THE UNIVERSITY OF CHICAGO

ENGINEERING LIGHT-MATTER INTERACTIONS WITH METASTABLE STATES IN A HEAVY FLUXONIUM

A DISSERTATION SUBMITTED TO
THE FACULTY OF THE DIVISION OF THE PHYSICAL SCIENCES
IN CANDIDACY FOR THE DEGREE OF
DOCTOR OF PHILOSOPHY

DEPARTMENT OF PHYSICS

BY
NATHAN DON EARNEST

CHICAGO, ILLINOIS
MARCH 2019

To All Of My Family. Blood And Otherwise.

TABLE OF CONTENTS

LIST OF FIGURES

ACKNOWLEDGMENTS

In my writing of this section, I am humbled by the great number of people who supported me throughout the duration of this thesis project. It is often said that it takes a village to raise a child, and no less is true to train a scientist. The vast number of people I have been able to interact with over my years at UChicago has given me so much to be thankful for and has undoubtedly shaped my outlook on life. This has made this section incredibly difficult to write – I hope that I do it justice none-the-less.

First and foremost, I must thank my advisor David Schuster. Not only did I have the privilege to be one of many students to benefit from his strong intuition and vast knowledge of circuit QED, but I had a wonderful time, no matter the conversation topic, be it cQED or which sort of pet you wanted most growing up – I always left conversations with Dave with ideas or a perspective that I did not have before. Working with Dave gave me the opportunity to pursue my interests and passions, and he always strived to create a rigorous and fun lab. I will miss the days of the super bowl parties and liquid nitrogen ice cream with everyone!

Next, I would like to thank my theory advisor – Jens Koch. Jens provided not only his immense knowledge and background on the development of the fluxonium as a source of guidance, but an open (albeit far) office where I had the chance to attend a few of his group meetings and get a better understanding of the theory behind my device. Jens also provided amazing attention to detail when it came to editing, one that is hard to match – which provided a great level of improvement to both the paper and this thesis work. Furthermore, thanks to Jens I had the fortune to work with Nick Irons and Brian Baker who both provided an incredible amount of help with establishing the theoretical/computational framework to study the Heavy Fluxonium. Many thanks to Nick for helping establish the initial fits to our data and to Brian for the many hours of conversation about simulation/experimental results. Comparing our data and creating a similar language by which we could work was

immensely helpful inunderstanding the device, and was critical in figuring out the correct frequencies to use.

I want to thank Jay Walter, who was always patient and listened to my ramblings. He taught me how to better present my scrambled observations and how to create simple, yet very powerful models. These were not only the initial models from which we started when measuring the device's parameters, but his help lasted throughout our experiments. I enjoyed and will miss the wandering conversations about physics, linguistics, and the many other topics.

Then there is the general Schuster lab community – of which there has been many individuals to whom I am grateful. Vatsan, or as I like to call him "the measurement master", was an absolutely pleasure to work with. His amazing attention to the slightest variation in measurements showed me how one could begin to parse out a true signal in the otherwise usual noise. I will miss our long nights of measurements and the ridiculous amount of laughing, often coming from the phrase: "As they say (insert random phrase)". ('They' rarely actually said the things we came up with). Ravi, you were an awesome coworker, roommate, and friend. I was always impressed by your ability to simplify the problem and create a more well-defined question, and enjoyed the hours of physics discussions (I look forward to the years of screaming "180!!!!"). Akash, I am so happy you and I were able to overlap in our time in grad school, and wish that same could have occurred in our undergrad lab. It was cool to see how our previous dark matter research could tie back into my graduate studies, and – more than that – you helped me remember to not take things too seriously. Abigail, it was a pleasure to teach you fabrication briefly, and even more to see how quickly I soon began to learn from you. I'm excited to see the continued excellence you will achieve in your fabrication and graduate studies. Victoria, I was able to enjoy the hours of junction imaging only through our interesting conversations that ranged from physics to social issues. I want to thank Yao for his time discussing physics problems, as well as the dinners we were able

to share over the years. When the lab felt lonely, Yao was always a great person to chat with. Gerwin, thank you for making sure the lab remained cleaned and organized!Andrew, thank you for the immense knowledge of proper machining techniques and I will miss gaining insight about this and all of the history of art you shared. Nelson, I am amazed at the cleanliness of your code, and will forever be in your debt for the code libraries you helped create. Ge, I must thank you for being one of the students to come before me and establish a considerable part of the lab, from the code (which I used throughout grad school to draw all of my devices) to the Oxford fridge (which is where I first measured the device presented in this thesis)! To "Dr." Dave, thank you for being one of the first people to teach me qubit fabrication, and making sure the lab was never empty at 3am. And, of course, many thanks to Brenda for always helping me get my reimbursements and the fun conversations! And thanks to the rest of SchusterLab: Alex, Kaitlyn, Sasha,Carolyn, Ankur, Helin, Gabrielle, Clai, Aziza, Chris, Mohammed, Sam, and Brendan, I always enjoyed conversations with you whether it be about physics or otherwise. I will miss you all.

I must also thank all of those at Argonne National Labs. In particular, I would like to thank Leo Ocola and David Czaplewski. You both helped me gain a strong familiarity with the JEOL tool that was used to make the device andguided me through my fabrication. Most, if not all, of my nanofabrication understanding can be attributed to these folks. And what I did not learn from those at Argonne, I thank the Pritzker Nanofab people: Peter, Anna, and Mike!

I would also like to acknowledge those that helped me immensely, though perhaps not directly – the community of fluxonium scientists who helped create the foundation of work that guided many of the decisions in the making of the junction size. I was fortunate enough to meet Ioan Pop and learn a considerable amount about the non-linearity of Josephson junction chains, and had the joy of seeing parts of Europe with him.

Physics is not my only passion – I have greatly enjoyed all of my theatre experience. To

all those in the IME-STAGE program: Nancy, Sunanda, Ellen, Sam, Kelcie, Edward, Yu, and all of those that I met but was not able to have longer conversations. I would like to extend my gratitude to all of those that worked with in the STAGE crew! Go check out their documentary to see me talk about my thesis.

And I, of course, must thank those who were in my life but not in lab! To my parents Valinda, Rick and Neji who all inspired me to always be deeply curious. To Lisa, who always encouraged me to push through the tough times in the PhD and knows how to always make me laugh. And to all of my educators before graduate school, both teachers and research mentors and all of the groups I was a part of, including CISN (Now Berkeley Hope), and Cal NERDS. These programs demonstrated the benefits of community, and I am so grateful for the friends I've made through these programs and the opportunities and help they provided.

ABSTRACT

In the past few years there has been an increasing amount of media coverage on quantum computing, largely due to the substantial investment in the superconducting circuit quantum electrodynamics (cQED) technologies by several governments and technology and finance companies throughout the world. Since their inception, superconducting qubits have realized several orders of magnitude improvement in information lifetimes, but individual qubit lifetimes must be further improved to realize a fault-tolerant quantum computer. A critical component of these circuits, which allows quantum states to be addressed, is the non-linear inductive element known as the Josephson junction.

In this thesis, we will present experimental studies showing how to design and fabricate the Josephson element to leverage a recently developed 'superinductor' as a way to engineer new qubit regimes, such as the heavy fluxonium. We create the heavy fluxonium with a chain of large Josephson junctions and a large shunting capacitor. This shunting capacitor increases the effective mass of a fictitious particle inside the wells of the heavy fluxonium potential energy landscape, giving rise to two characteristically different transitions: intra-well transmon-like plasmon transitions and inter-well fluxon transitions. The fluxon transitions are heavily suppressed by a reduced dipole matrix element realized from the increased effective mass, and result in metastable fluxon transitions, with T_1's as large as 8ms. This qubit design offers the possibility to study qubit interaction with the thermal bath, the implementation of atomic state preparation techniques such as Raman gates, optical pumping and fluorescent style readout, as well as the possibility to make substantial improvements in qubit lifetimes and create protected qubits in the cQED platform.

CHAPTER 1

INTRODUCTION

1.1 The Interaction of Light and Matter: A classical perspective

Titling this thesis as "Engineering the Interaction of Light and Matter" made it necessary to explain what is really meant by 'light' and to clearly lay out the different ways that we engineer interaction between light and matter. To this end, I would like to quickly discuss what most people (particularly those outside of physics) would call light: The 'visible' spectrum.

1.1.1 The 'Visible' Spectrum

We often start off perceiving light as the "visible spectrum", and don't really consider the energy outside this spectrum as light. This perspective is likely because our eyes have evolved to absorb energy in this spectrum, with four different types of absorbers (see figure 1.1). Three are responsible for color (the cones in our eyes) and the other is useful for low light sensitivity (the rods in our eyes). The very first stage of vision occurs when light, with wavelengths varying from roughly 440nm to 700nm, strikes one of these sensitive proteins (figure 1.1c for rods) and changes its chemical structure. Amazingly (though – perhaps – unsurprising), the human eye has evolved to be most sensitive to light in a similar range to the range of light that is mostly produced by our sun (figure 1.1d). Within this spectrum of light, we can already discuss a wide variety of light/matter interaction. Of particular interest, and of large familiarity, is the concept of so-called dispersion relations. A dispersion relation is a means of describing how the wavelength of light will determine its interaction within a medium, and is one way in which one can understand light's interaction with matter. In figure 1.2a, we can see the commonly known dispersion effect when white light, consisting of many different frequencies of light, enters a prism and causes the different colors (or

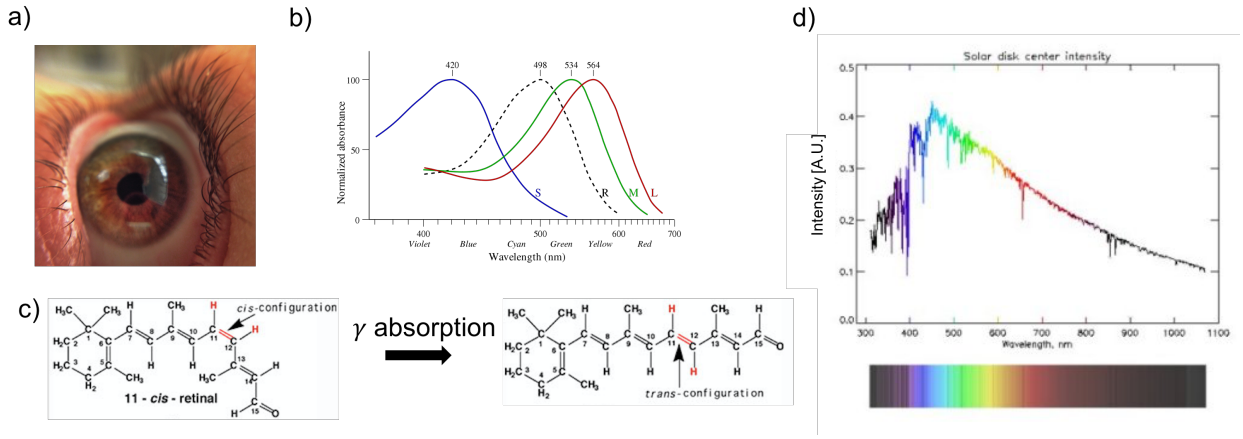

Figure 1.1: a) A macro photo of a human eye. b) A graph showing the sensitivity of each of the photoreceptors in the human eye. c) One of the photoreceptors (the rods) chemical structure before and after absorption of a photon at 500nm d) The spectrum of light produced by our sun. The peak intensity occurs in the visible range, but there is also light produced outside the visible spectrum. The center point of this spectrum is determined by the temperature of the sun and can be described well by black-body radiation.

wavelengths) to spread out and undergo a dispersion relation which depends on the material of the prism. This idea of a dispersion relation is rather general and can be part of what one engineers in the microwave regime [46]. While the visible spectrum of light may be what we are most familiar with calling 'light', this is only a very narrow part of the spectrum. As we move outside of this spectrum, we begin to be capable of studying many different effects.

1.1.2 All the light we cannot see

Though we tend to be most familiar with light as being a combination of the Red, Green and Blue wavelengths, we actually use and interact with light that is outside of this spectrum on a daily basis. We interact with light in the form of heat (this is light that has a longer wavelength than the visible), X-rays (light with shorter wavelength than the visible), or - of particular relevance to this thesis - light that we usually call 'radio waves', which can be picked up with a dipole antenna (figure 1.2b). This antenna (the 'matter') is capable of interacting with radio waves (the 'light'). The physical size of the antenna in this case

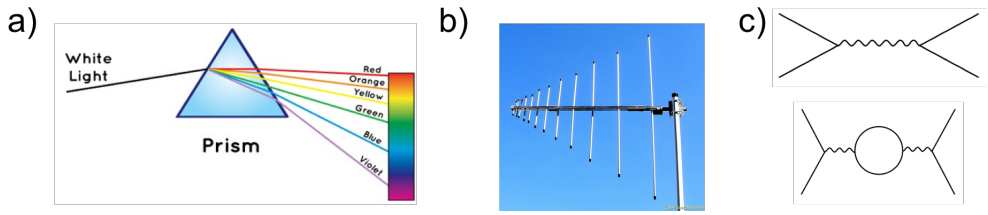

Figure 1.2: a) A very common and well-known depiction of light matter interaction is the dispersion that occurs when white light enters a prism. The prism causes the different wavelengths of light to bend with differing angles and consequently separates the white light into its different color components. The frequency dependent interaction of light and matter is known as chromatic dispersion and is a useful relation when thinking about superconducting circuits interactions with microwave light. b) A dipole antenna often used to pick up radio signals. The longer the antenna, the larger the dipole. This principle of a dipole will be important when thinking about creating a protected qubit. c) Two different Feynman diagrams used in Quantum Electrodynamics as a way to represent different interactions. Shown is the electron-positron interactions with the bottom figure depicting a higher-order interaction.

determines both how small of a light signal can be picked up, as well as the frequency range of sensitivity. In an analogous manner, this thesis will seek to engineer a dipole antenna of an atom. However, unlike the situation where we wish to have a very large antenna, as to be capable of hearing the radio station with our favorite songs, our antenna has to do with how strongly the quantum system we are studying couples to the noisey microwave environment. In the case where we wish to have a long-lived quantum state, we will seek to suppress the 'size' of our antenna, and consequently shield it from the classical environment. The intuitive reason we will wish to do this is to suppress interaction of our quantum systems with the classical noisy environment, as it is this environment that degrades the quality of our qubit. The challenge will be to make this dipole antenna really small, while still being capable of 'hearing' (i.e. measure/control) our 'radio station' (i.e. our quantum state).

1.2 The Interaction of Light and Matter: A quantum at a time

1.2.1 Quanta of Energy: Light is a particle too

With all of the interaction discussed above, we can view and describe these phenomena of light as a wavefront that bounces off some matter and then is either viewed by our eye, or picked up by our radio, or warms us up. None of these features really require that we treat light as a particle, and was the accepted theory of light until the early 1900s. Around this point, Einstein, in an attempt to explain the curious feature of discrete electrons being ejected from a metal plate when struck by low intensity ultra-violet light, proposed a thought experiment of the photo-electric effect in 1905. This effect was later confirmed by Robert Millikan in 1914, though at the time he did not agree with the 'corpuscle' nature of light. This, along with several other experiments at the time, started a scientific revolution and opened up one of the most successful theories to date: the theory of quantum mechanics. When thinking about quantum mechanics, I like to view it as coming in three 'layers':

1. Energy, at its most fundamental level, can be described in discrete quanta - which we call 'particles'. This is the reason it is dubbed "quantum" mechanics. This feature alone is quite prevalent in nature, and can be used to explain a substantial number of phenomena, such as how lasers work. It is often deemed the 'semi-classical' limit, as it only uses the quantum phenomena of discrete energy levels to describe a system, but otherwise uses classical dynamics to study the system's time evolution.

2. These discrete packets however are also waves and can be described as such. They can spread out over space and be put into a 'superposition' of states, and occupy multiple energy levels or places at once. Once the state of one of these particles is measured, it is projected into one of these states and no longer exists in both.

3. When these discrete packets of energy (particles) are brought together and made to

interact in a specific way, they can be 'entangled', which says that a measurement on one particle will immediately collapse the other particle into a particular state.

This thesis will primarily focus on the first two layers: Namely, we will engineer a system that has discrete energy levels, and can be put into a superposition of different energies. To do this, we will use the Circuit Quantum Electrodynamic approach (cQED), as a way to realize the interaction individual atoms and photons.

1.2.2 Quantum Electrodynamics (QED)

Quantum Mechanics is often dubbed as "the most successful scientific theory", which may beg one to ask why it deserves such a title. Part of the reason people often feel so comfortable making such a strong claim arises from the phenomenal precision that the theory brings about. Specifically, when studying the interaction of light and matter, this interaction has a characteristic strength, the so-called 'coupling strength'. This interaction strength can then be described with an increasing amount of precision with the use of perturbation theory, which is often dubbed as the 'order' of the coupling strength. The coupling gives rise to the fine structure constant:

$$\alpha = \frac{e^2}{\hbar c} \tag{1.1}$$

where e is the charge of an electron, $\hbar$ is the Planck constant, and c is the speed of light. This constant, being dimensionless, is roughly 1/137 regardless of units and generally describes the interaction of the elementary charge, e, with the electromagnetic field (i.e. photons). A first order approximation gives that $\alpha \approx 1/137$, but once we start taking higher order terms, corrections get added to 1/137. When higher order terms are calculated, the interaction strength of light and matter can be calculated and measured to be accurate within 0.23 parts per billion, and corresponds to going to tenth-order Feynman diagram [1]! (An example of a Feynman diagram can be seen in figure 1.2c.) This term determines the interaction strength of light and matter which, in the field of Cavity QED (CQED) and circuit QED (cQED),

ultimately comes down to the exchange rate of energy and will determine the rate at which we can couple different quantum states, as discussed below.

1.2.3 Cavity vs Circuit QED: 'α' vs 'g'

Cavity Quantum Electrodynamics was the original realization of the interaction of light and matter at the individual quantum level (figure 1.3a), and led to a Nobel prize in 2012 for Serge Haroche and David Wineland. Specifically, CQED is the study of interaction between light confined in a reflective cavity with an atom, and creates a coupling where the quantum nature of light becomes an important aspect to appropriately describe the system. In the case of a two-level atom coupled to a cavity, such a system is generally described by the Rabi Hamiltonian:

$$H_{\text{Rabi}} = \frac{\omega_0}{2}\sigma_z + \omega_c a^\dagger a + g(\sigma_+ + \sigma_-)(a + a^\dagger), \tag{1.2}$$

where the first term, $\omega_0\sigma_z$, describes the two-level atom, with a frequency ω_0. The second term, $\omega_c a^\dagger a$, represents the cavity at frequency ω_c and $a^\dagger a$ is the number of photons inside the cavity. The last term describes the exchange of energy between our two level atom and the cavity photons. σ_+ (σ_-) represents the atom going to the higher (lower) energy level and $a^\dagger$ (a) represents an increase (decrease) is the number of photons inside the cavity. 'g' describes the strength (i.e. rate) of interaction between the light and matter, and gives as sense of how quickly this exchange of energy can occur and is given by:

$$g = -\frac{E d_{01}}{\hbar}\sin(kx), \tag{1.3}$$

where E is the strength of the associated cavity electric field, $\sin(kx)$ captures the oscillatory behavior of the cavity field and d_{01} is the dipole element of the atom that we alluded to earlier. However, equation (1.2) includes counter-rotating terms ($\sigma_+ a^\dagger$ and $\sigma_- a$) that, in CQED, are at very high frequencies relative to the coupling strength g. In the case

when $g/\omega \ll 1$ we can take the rotating-wave approximation (RWA) and simplify the above Hamiltonian to the well-known Jaynes-Cummings model:

$$H_{\mathrm{JC}} = \frac{\omega_0}{2}\sigma_z + \omega_c a^\dagger a + g(\sigma_+ a + \sigma_- a^\dagger), \tag{1.4}$$

where we have removed the counter-rotating terms $\sigma_+ a^\dagger$ and $\sigma_- a$. In order to study quantum states, we used the circuit QED system (cQED) [7], which is the microwave electronic equivalent to CQED (see figure 1.3b/c). In this case, we can have two different approaches to realizing cQED, a so-called '3D' version (see figure 1.3b) in which the light cavity is a literal microwave cavity, and 'mirrors' are replaced by brass antennas as seen in figure 1.3b. There is also the '2D' version (figure 1.3c), where a patterned LC oscillator (which will behave as our photon cavity) is coupled to an artificial atom via a capacitive or inductive coupling. In this case, capacitors create a large impedance mismatch and make an artificial mirror, and our non-linear superconducting circuits serve the function of an artificial atom. In the case of a 2D realization of cQED, the coupling is given by:

$$g = \frac{eV_0}{\hbar}\beta, \tag{1.5}$$

where β is a dimensionless parameters dependent on the voltage division of the circuit and V_0 is the voltage put across an LC resonator when a single photon is present. The exact nature of these parameters, how they arise and are related to CQED is explained very well in "Circuit Quantum Electrodynamics" [7], and I highly encourage anyone to read this thesis to get a full understanding of the comparison of CQED and cQED. In the next two chapters I will describe how we can use this approach to engineer the interaction of light and matter both in a more classical sense and at the quantum level.

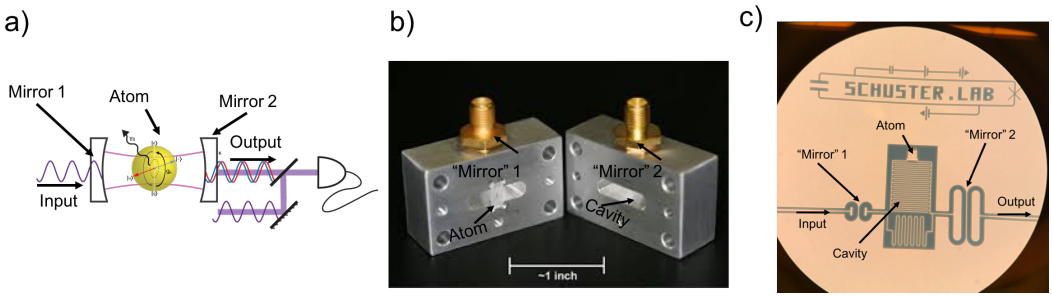

Figure 1.3: a) The prototypical cavity QED setup used to measure light/matter interactions at the quantum level. b) A "3D" realization of circuit QED, where a microwave cavity is made from aluminum and the artificial atom is placed on a sapphire chip near the location of largest electric-field coupling. In this 3D cavity design, it is located near the center of the cavity. c) An example of a circuit QED chip setup labeled with the cavity QED equivalent features. Pictured is a prototype design for the 0-π circuit (to be discussed in outlooks). Mirror 1 is our input capacitor and mirror 2 is the output capacitor. The large capacitance serves to make the 'mirror' more translucent and gives photons inside our LC resonator a preferential direction to propagate, subsequently going into the amplification chain.

1.3 Classical vs Quantum Information

1.3.1 Computers and Classical Information

In this day and age of technology, with computers within arm's reach at any point of the day, the study of information is as relevant as ever. Generally, when we think of information, we tend to think of it as things like a photo, a phone number, etc. However, when I discuss information in this thesis, what I really seek to bring to mind is the individual bits that are used to store the photos (and other such things). In other words, if I write the string:

$$0001101101010111,$$

I have put down 16 bits of information. Nowadays, these individual bits are made up of tiny transistors, and whether it is '0' or '1' is a matter of whether the transistor is 'on' or 'off'. In the case of only two bits of information, we have four possible combinations to describe the system: 00, 11, 01, or 10. However, once we discuss quantum bits, we will see that

the system becomes more complicated and will require a different mathematical means of describing their state.

1.3.2 Quantum Information

A quantum bit is a quantum realization of a classical bit where instead of being either '0' or '1' a bit can be put into a probabilistic superposition of being in both states:

$$|\psi\rangle = \alpha\,|0\rangle + \beta\,|1\rangle\,, \tag{1.6}$$

where the probability of being in the $|0\rangle$ state is given by $|\alpha|^2$ and the probability of being in the $|1\rangle$ state is given by $|\beta|^2$ and we must satisfy the condition $|\alpha|^2 + |\beta|^2 = 1$. However, until the device is measured it 'exists' in all possible combinations of both states, at the same time. A convenient way to represent the state of the device is to describe it as a point on the 'Bloch sphere' (figure 1.4a). On this sphere, the state $|0\rangle$ is represented by a vector pointing towards the north pole of the sphere, the $|1\rangle$ state is represented by a vector pointing towards the south pole, and an equal superposition of the two $\left(\frac{|0\rangle+|1\rangle}{\sqrt{2}}\right)$ is represented by a vector along the equator.

The unique property of quantum information is that you can create an entangled state, whereby two discrete systems can only be described by a single wavefunction. One such state, known as the Bell State, is given by:

$$|\Psi\rangle_{\text{Bell}} = \alpha\,|0\rangle_1\,|0\rangle_2 + \beta\,|1\rangle_1\,|1\rangle_2\,, \tag{1.7}$$

where the probability to measure our bits in either '01' or '10' is now zero, and the probability to measure '00' is given by $|\alpha|^2$ and '11' by $|\beta|^2$. This phenomenon is the 'spooky action at a distance' that bothered Einstein and other physicists when quantum mechanics was first being discovered and it the quintessential feature that allows one to create quantum

algorithms that are faster than classical algorithms for specific tasks.

1.3.3 Realizing a quantum bit

We have seen that a quantum bit is a device that can be put into a superposition of '0' and '1', but this then raises the question: What actually is a quantum bit? There are a myriad of ways in which we can realize a quantum bit, and the physical representation of the '0' or '1' state depends on the specific realization of the device, each with its potential strengths or weaknesses for the purposes of a quantum computer. It ultimately is the result of a quantum system being able to be placed in two different energy states. (If you wish to use more than two quantum states, this is then called a 'quantum digit' or 'qudit'.) For the purpose of building a quantum computer, there are generally 5 factors by which we compare any system's promise, deemed the "DiVincenzo criteria", listed in the following:

1. A scalable physics system
2. The ability to initialize the state of the qubits to a ground state
3. A "universal" set of quantum gates
4. A measurement scheme which allows one to measure specific qubits
5. Long 'coherence' times as compared to the gate times

One possible way to realize a quantum computer would be to use the polarization of a photon to create our quantum states (figure 1.4b). A vertical polarization can be our '0', horizontal polarization '1' and we can then put it into circular polarizations to realize arbitrary quantum states. This allows us to satisfy conditions 2, 3, 4, 5 of the DiVincenzo criteria, but in this case creating entangled states and having a 'scalable physics system' becomes difficult because photons do not inherently interact with each other. Another possibility is to use different energy states of a real atom, which are inherently quantum

in their nature. Several atoms can be coupled together by placing them inside an ion trap (figure 1.4c), and atom-atom interaction can be mediated by photons bouncing in between mirrors in the cavity (direct atom-atom interactions are difficult due to the small dipole element of atoms and getting atoms close enough to have a reasonably strong coupling). This approach satisfies all of the conditions listed above and is a promising avenue to realize a small quantum computer, but will become increasingly more difficult to scale-up due to the technical difficulty of trapping more and more atoms. Though this scaling challenge is a universal difficulty, one more possibility, the specific approach used in the case of this thesis, is to use the phase of a Josephson junction as our quantum states. The benefit to this approach is that the variety of weaknesses that are inherent to other systems, could possibly be engineered away.

Artificial atoms (i.e. superconducting Josephson junction circuits) have garnered the most amount of attention in regards to the building of a quantum computer due to their promising ability to satisfy all of the DiVincenzo criteria. In particular, the improvement of coherence times since their inception (Figure 1.5a), provides the ability to perform many 'quantum gates' before the system decays, allowing for sophisticated quantum algorithms to be implemented. In particular, figure 1.5a has a horizontal dashed line, which is the minimum individual qubit coherence time required to realize particular error correction schemes in a scalable manner and various systems have been closing in on this restriction. In order for the scaling of these devices to be realized at a fault-tolerant level, however, the coherence times of individual qubits must still be further improved. The focus of this thesis is to engineer a system that satisfies condition 5 of the Divincenzo criteria, by further increasing the coherence times of a qubit, while maintaining short qubit operation times.

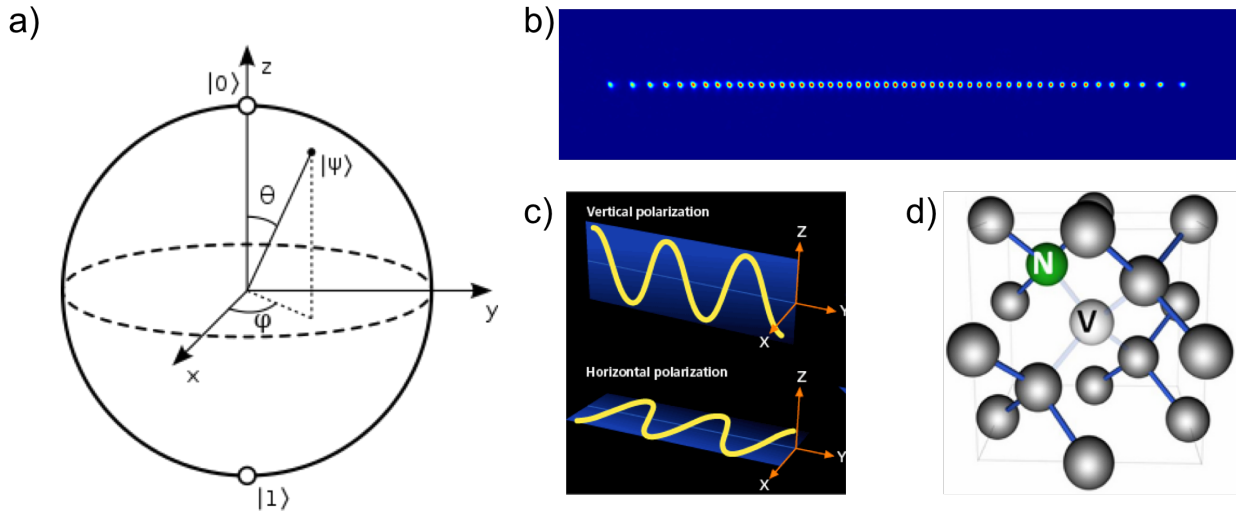

Figure 1.4: a) The 'Bloch sphere', a useful means to represent arbitrary quantum states of a two-level system. The north pole can be called our "0", the south pole our "1" state, and a point of the equator would represent an equal superposition of "0" and "1". b) A 50-atom quantum computer, realized by the Monroe group at University of Maryland. A promising avenue to realize a quantum computer, that will complement superconducting qubits well. b) A demonstration of two possible light polarization states that can be used as a quantum bit. This approach, however, is difficult to scale as photons do not inherently interact. d) A cartoon depiction of an NV-centre. These systems demonstrate rather long coherence times, even at room temperature, and can be measured and controlled with optical light, making them a strong candidate for the development of a quantum computer. However, coupling multiple NV-centres together is a technically difficult challenge due to the small dipole matrix element of the electric field.

1.3.4 Superconducting Qubit Overview: Improvement over the years

Defining Qubit Coherence

The fifth requirement of the Divincenzo criteria brings out three different elements by which we should judge a qubit's usefulness: The qubit lifetime (T_1), the qubit coherence time (T_2), and the gate operation time (T_g). The qubit lifetime is the average time it takes for the qubit to decay to its ground state. The coherence time is the time in which the qubit will be placed in a superposition state $|\psi\rangle$, and can be measured as being in this state before the phase between our two quantum states is blurred out and can no longer be distinguished by measurement. This, in some sense, is the point when the 'quantum-ness' of the qubit has decayed and we have a classical bit randomized between '0' and '1'. The gate time is the amount of time is takes to rotate our qubit to an arbitrary point on the Bloch sphere (figure 1.4a). Generally, a qubit's gate time is judged by the time specific gate of rotating by an angle of π on the Bloch sphere and go from $|0\rangle \rightarrow |1\rangle$, and is called t_π. When judging the quality of a qubit one must judge the minimum of T_1 or T_2 relative to the gate time T_g, as this determines the total number of quantum operations that can be done on a single device. This ratio is part of what goes into determining the 'quantum volume' of a qubit.

1.4 Thesis Overview

This thesis starts off by giving an overview of the theory of the fluxonium circuit. Chapter 2 reviews the general cQED platform and the common elements that come together, such as the Josephson effect, different style resonator setups, and introduces two realizations of an artificial atom: the transmon and fluxonium circuits. We discuss Fermi's Golden Rule as it relates to creating protected qubits, and the principle of a Λ system to coherently couple protect states.

In chapter 3 we delve more into the specifics of the fluxonium theory. We review the effects

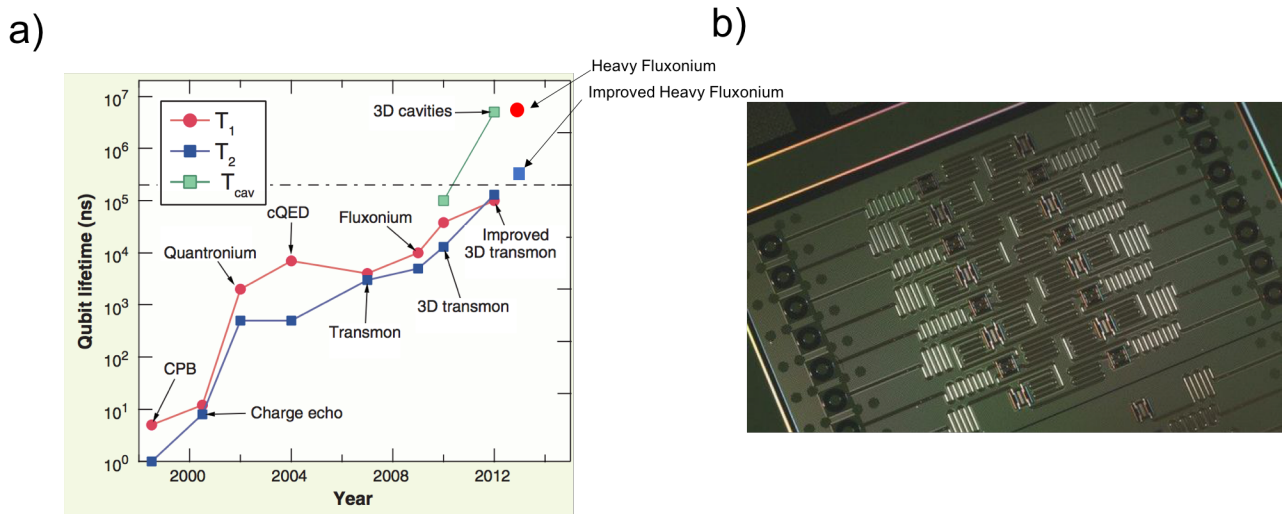

Figure 1.5: a) A chart from [9] showing the improvement of qubit lifetimes and coherences over the past couple of decades with recent results added to the chart [14, 11, 16]. It is this substantial improvement in coherence, along with the versatility of superconducting circuits that has made them the popular system to pursue a large quantum computer. Note the recent result of the heavy fluxonium [14, 11] achieving T_1s above a millisecond and the improved heavy fluxonium [16] achieving T_2s of several hundred microseconds and for the points measured hitting the limit of $T_2 = 2\,T_1$. This improvement was the result of carefully trading off the benefit of a suppressed dipole element for a good T_1 vs having a 'sweet spot' for good T_2s. b) A photo of the 19-qubit quantum processor by IBM. In this photo, they use 2D transmon qubits coupled to nearest neighbors via capacitive coupling.

of the different circuit components on the energy landscape via the phase basis of the circuit. Specifically, we show how we create a protected qubit, the 'heavy' fluxonium, with a chain of large Josephson junctions and a large shunting capacitor. This shunting capacitor increases the effective mass of a fictitious particle inside the wells of the heavy fluxonium potential energy landscape, giving rise to two different transitions: intra-well plasmon transitions (which are similar to those seen in transmon qubits) and inter-well fluxon transitions, which are heavily suppressed due to the reduced dipole matrix element realized from the increased effective mass. We demonstrate how implementation of a superinductor with a large enough inductance allows one to realize a qubit with a triplet excited state at zero flux quantum. We allude to the Bloch basis as an alternative approach to studying the fluxonium and how, in the limit of infinite inductance, the heavy fluxonium is dual to a transmon. We then discuss how nearby plasmon modes increase the χ-shift of our readout resonator and result in a different form of dispersive coupling (called plasmonic coupling) which hybridizes our qubit and resonator modes. This plasmonic coupling makes it possible to read out out the qubit over the entire flux quantum as well as perform a fluorescent styled readout on our device through cycling on different plasmon-transitions. We then discuss the chain design of the fluxonium and how one must take special care to consider the non-linear behavior of the chain. We conclude by discussing different gate methods that can be used in the fluxonium circuit, including Raman transitions rates and a scheme equivalent to optical pumping.

In chapters 4 and 5 we discuss the various ways in which one can fabricate a Josephson junction, as well as the details of the experimental setup. Importantly, we show a few different mask designs, and the associated failure modes for each of the designs. In particular, we found that careful surface preparation (particularly for sapphire substrates) ensures good adhesion between the mask and the substrate, which then allows for higher yield fabrication. Specifically, personal experience has shown that it is important to bake the wafer above 100C at low vacuum pressures to ensure all residual water has been removed from the surface. We

also show some initial procedures for realizing stacked Josephson junctions, which is an alternative approach to realizing linear inductances above a micro-henry.

In chapters 6 and 7 we cover the various experimental results for our fluxonium circuit. We demonstrate metastable fluxon transitions, with T_1's as large as 8ms, limited by dielectric loss in the capacitor. Due to the suppression of the dipole matrix element the coherent gate times are also increased, to a point where direct transitions are effectively forbidden ($T_{\mathrm{g}} \gg T_2$). To measure and coherently couple these long-lived states, we make use of the plasmon transitions which are relatively insensitive to flux and couple to isolated states in multiple wells, allowing for the implementation of Raman transitions and gate schemes equivalent to optical pumping in superconducting circuits. The plasmonic coupling in this circuit allows one to realize a fluorescent style readout through cycling on different plasmon-transitions, and also results in the realization of photon/plasmon assisted transitions, which demonstrate an increased coupling of fluxon transitions when there is a photon or plasmon excitation is present. The suppressed dipole element also allows one to tune the primary fluxon transition over several orders of magnitude, with a maximal energy transition of 4.6GHz at zero flux quantum, down to sub-Megahertz frequencies at half-flux quantum. Consequently, we can see the effect of the thermal bath of the dilution fridge as we tune our primary fluxon transition to lower frequencies such that $\omega_{g_0 g_1} \sim kT$, thermally exciting the qubit into the excited fluxon $|g_1\rangle$ state. This results in some avoided crossings appearing in the resonator-like peak associated with the qubit being in the $|g_1\rangle$ state. Surprisingly, the small fluxon tunneling rate resulted in a negative temperature state (with a yet-to-determined cause) which persisted for varying periods of time, including a period that lasted for over a week's duration. During this persistent negative temperature state, one can see when $\omega_{g_0 g_1} \sim kT$, the thermal bath would 'excite' the qubit into the $|g_0\rangle$ state, as determined by fluorescent readout of the $|g_1, 0_r\rangle \rightarrow |e_1, 0_r\rangle$ branch. This led to the pronounced onset of avoided crossings associated with the qubit being in the 'global' ground state $|g_0\rangle$. One of

these avoided crossings is captured by the current Hamiltonian model of the system and is associated with a higher order coupling involving the exchange of a fluxon and photon for a plasmon. In addition to this understood avoided crossing, several avoided crossings appeared that are not captured by our current Hamiltonian model, which appear to connect our resonator-like and plasmon-like features, and reflect features seen in a higher 2 photon energy manifold (and are in close proximity to associated photon assisted transitions). We conclude this thesis with an outlook chapter where we briefly discuss future generations of protected qubits such as the 0-π circuit, and possible implementations of the superinductance for realization of ultra-strong coupling schemes, as well as providing some possible explanations for the negative temperature state measured on this device and others.

CHAPTER 2

CIRCUIT QED BASICS

2.1 Engineered Light Cavity

2.1.1 Lumped Element Cavity

To explain how we will engineer our light cavity, we first look at the prototypical harmonic oscillator system that is shown in introductory Newtonian physics courses (figure 2.1a). In this case the Hamiltonian for the system is given by:

$$H = \frac{p^2}{2m} + \frac{1}{2}m\omega^2 x^2, \tag{2.1}$$

where ω is the resonant frequency of the system and is determined by using Newton's first law and Hooke's law of a spring, giving:

$$\omega = \sqrt{\frac{k}{m}}. \tag{2.2}$$

A few years after we learn this relation in our classical mechanics course, we instead treat it as a quantum mechanics system and find that $\hat{x}$ and $\hat{p}$ are quantum operators that do not commute with each other with the following relation:

$$[x, p] = i\hbar, \tag{2.3}$$

and has energy levels given by:

$$E_n = \left(n + \frac{1}{2}\right)\hbar\omega, \tag{2.4}$$

with the same ω as seen in equation (2.2). Instead, we can look at the Hamiltonian of

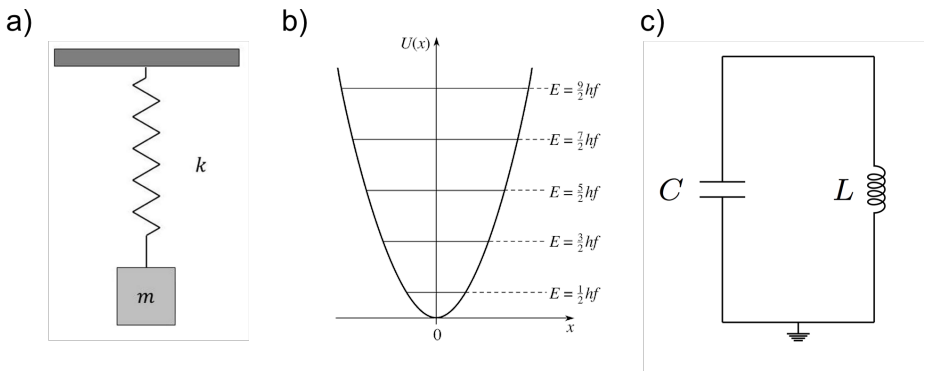

Figure 2.1: a) A mass on a spring, the prototypical harmonic oscillator that is introduced in Newtonian physics courses. b) When the harmonic oscillator is treated as a quantum system it will have discretized energy levels spaced apart evenly by $\hbar\omega$ where omega is the characteristic frequency of the system. c) A LC-oscillator is a different type of harmonic oscillator.

an electrical LC-Oscillator, which is given by:

$$H = \frac{q^2}{2C} + \frac{\delta^2}{2L}, \tag{2.5}$$

where C is the capacitance of the circuit with q being the charge stored on the plates and L is the inductance of the circuit with $\delta{=}LI$ being the flux stored in the inductor. There are two immediate things I would like to point out. First, we can see that there is a relation between the capacitance of the circuit and the mass hanging from the end of the spring, such that $C \sim m$. This principle will become important when we make the fluxonium qubit 'heavy' as a method to improve our qubit lifetime, as this increased mass reduces quantum tunneling rates. The second thing I would like to point out is that in the above formulation of the LC oscillator Hamiltonian we have an analogy between the charge of the circuit and momentum of the mass ($\hat{q} \sim \hat{p}$) and the flux of the circuit and the momentum position of the mass ($\hat{\delta} \sim \hat{x}$). One can show that the canonical variables of this Hamiltonian are $\hat{q}$ and

$\hat{\delta}$, which then gives the commutation relation:

$$[\phi, \delta] = 2ei \tag{2.6}$$

Continuing with our understanding of the LC-oscillator as a harmonic oscillator, we can then describe the associated energy of the resonator by the traditional 'raising' ($\hat{a}^\dagger$) and 'lowering' ($\hat{a}$) operators:

$$H = \left(\hat{a}^\dagger \hat{a} + \frac{1}{2}\right) \hbar\omega \tag{2.7}$$

$$= \left(\hat{N} + \frac{1}{2}\right) \hbar\omega \tag{2.8}$$

with the energies E_n as given in 2.4. The convenient aspect to equation (2.8) is that we have now put it in the form of the 'number operator' $\hat{N}$, which corresponds to the number of photons inside the cavity.

The microwave frequency regime is an interesting section of the light spectrum because it has a characteristic wavelength that occurs at scales from 100μm to 1m. Because the waves have constructive or destructive interference on these lengths, the electrical behavior of a device will dependent strongly on its geometry. Consequently, there are two distinctive electrical resonators one can engineer: lumped element resonators, in which the size of the resonator is small enough to ensure any resonant features associated with the geometry are at frequencies sufficiently high enough to not influence circuit dynamics, or λ resonators that are designed with a particular length and boundary condition to create standing waves that oscillate at a frequency that is designed by the effective cavity length.

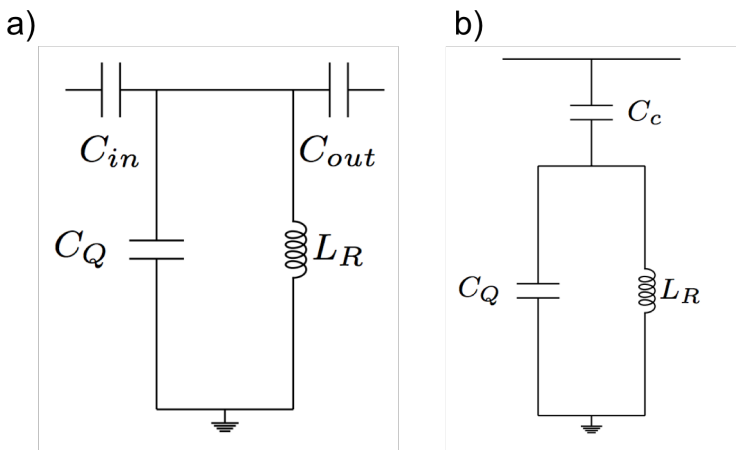

Figure 2.2: a) Transmission style resonator which was used in the heavy fluxonium experiment b) Hanger style resonator which is useful when trying to determine the internal quality factor of a resonator.

Hanger/Transmission Resonators and Quality Factors

When measuring a signal of a resonator, there are two different styles of resonance one can use: either a transmission style resonator (figure 2.2a) or a hanger style resonator (figure 2.2b). To measure the internal quality factor of the resonator, one can use the hanger style resonator, in which case the transmission is given by [48]:

$$S_{21}(\nu) = 1 - \frac{Q_{\mathrm{c}}^{-1} - 2i\frac{\delta\nu}{\nu_R}}{Q_{\mathrm{tot}}^{-1} + 2i\frac{\nu-\nu_R}{\nu_R}}, \tag{2.9}$$

where ν_R is the resonance of the hanger resonator, ν is the probe frequency, Q_{c} is the coupling Q, and Q_{tot} is the total Q. From this we can then extract the internal quality factor:

$$Q_{\mathrm{int}} = \frac{Q_{\mathrm{c}} Q_{\mathrm{tot}}}{Q_{\mathrm{c}} - Q_{\mathrm{tot}}}. \tag{2.10}$$

The same principle applies in the case of the transmission style cavity, but with the coupling Q being mediated by both the input and output capacitors. In such a situation, the internal quality factor cannot be extracted, but a preferred direction can be set by making the 'output'

capacitor larger. Intuitively this is because the impedance of a capacitor, $Z_C = 1/\omega C$, is reduced with a larger capacitor and makes the 'mirror' more translucent.

2.1.2 Transmission Line Cavity

The above treatment was for a lumped element cavity, where we had distinct capacitive and inductive elements. However, it is also possible to create a cavity in which the circuit elements are no longer distinctive components, but instead are more akin to a transmission line with boundary conditions that are determined by the geometry and the circuit. In the case where the transmission line is capacitively coupled to our outputs on both ends, we will have $\lambda/2$ resonances, similar to a standing resonance that exists for a tube with open ends on both sides. In this situation, the effective length of the transmission line is given by $\lambda = 2\pi v/\omega$. Interestingly, light will propagate down a lossless transmission line with a velocity, v, given by:

$$v = \frac{1}{\sqrt{L'C'}} \tag{2.11}$$

where L' is the inductance per unit length and C' is the capacitance per unit length. If so inclined, one could make the transmission line out of the same highly inductive linear Josephson junctions we use to create the fluxonium as a way to slow light down dramatically [12]. In such a situation, the dispersion relation of our transmission line is given by [48, 51]:

$$\kappa(\omega) = \omega \frac{\sqrt{L_J C_g}}{\Delta x} \frac{1}{\sqrt{1 - \omega^2/\omega_p^2}} \tag{2.12}$$

Where L_J is the Josephson inductance, and C_g is the capacitance to the ground plane. The ability to slow the speed of light down dramatically is due to the ability to make a linear element in which L_J is very large (about 10,000x larger than the typical geometric inductance). Moreover, by making a transmission line from large Josephson junctions, one can realize a traveling wave parametric amplifier [2], study analogs to space-time fluctuations

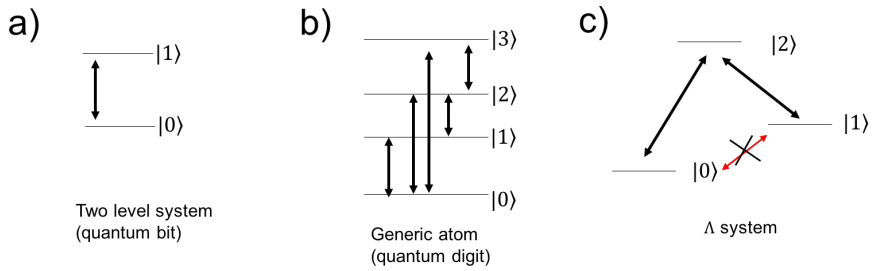

Figure 2.3: Different realizations of artificial quantum systems that are discussed in this thesis. a) A two-level system. Though the transmon is not a true two-level system, we are able to access the first two levels and study coherent oscillations between them. At low driving powers, the higher energy levels can be ignored, though it is useful to not ignore them in the case of fast-flux gates for multi-mode realization of a quantum system [17]. b) A generic atom consisting of multiple energy levels, generally known as a 'quantum digit' (qudit). c) A Λ system with two states ($|0\rangle$ and $|1\rangle$) cannot directly couple, but their interactions can be mediated by a third higher auxiliary level ($|2\rangle$) that couples to both [14].

on the Hawking radiation process [69], or even begin to study other interactions of light and matter with Luttinger liquids [6] or superconducting/insulating phase transitions [12].

2.2 Matter

'Matter' is a very general term that can mean a lot of different things. This can range from electrons, to quarks, more complicated atomic structures, or even dark matter (something we actually are trying to search for now using superconducting qubits [49, 50]). For this reason, I would like to constrain our perspective of what we are defining as matter into three different categories that are relevant for this thesis work: 1) A two level system, where the matter is well described by two quantum states, 2) A general 'quantum digit' with many different quantum energy levels that describe the matter and 3) A Λ system, where there are two states that cannot communicate with each other directly but can be coupled by a third higher auxiliary state (see figure 2.3).

2.2.1 Engineering Matter

Anharmonic Oscillators: Accessing a two-level system

The issue with harmonic oscillators is that putting in a single excitation is difficult, because the frequency of a single excitation is on resonance with subsequent excitations (n=2,3,4,etc). However, if one adds a slight anharmonicity, this will change the energy spacing of the energy levels. If this shift in energy level spacing is large enough, this makes it possible to resolve specific states and coherently address two such energy levels and create a qubit. While there are many ways one can engineer such a non-linearity - there (to date) is nothing better than the Josephson junction. The Josephson junction is the only known lossless non-linear inductive element and will be the work horse of this thesis and all of superconducting quantum computing.

The Josephson effect

The key element used in the development of superconducting quantum circuit is the Josephson junction. The effect, predicted in 1962 by Brian David Josephson [67] and experimentally verified in 1963 [18], is the critical element that gives rise to the anharmonicity needed to address two specific states and create our quantum bit with a superconducting circuit. Ultimately these quantum states come down to variation in the phase across our Josephson junction, but the exact physical representation of this change depends on the specific circuit components used and the states being addressed. Here I will quickly delve into the physics behind the Josephson junction and how it gives rise to a quantum circuit, using a transmon qubit as an example model to start.

In conventional superconductors, the attractive interaction that creates Cooper pairs (and consequently superconductivity) arises from a second-order interaction between phonons and electrons. To maximize the net interactions of the electrons, we state that every cooper pair

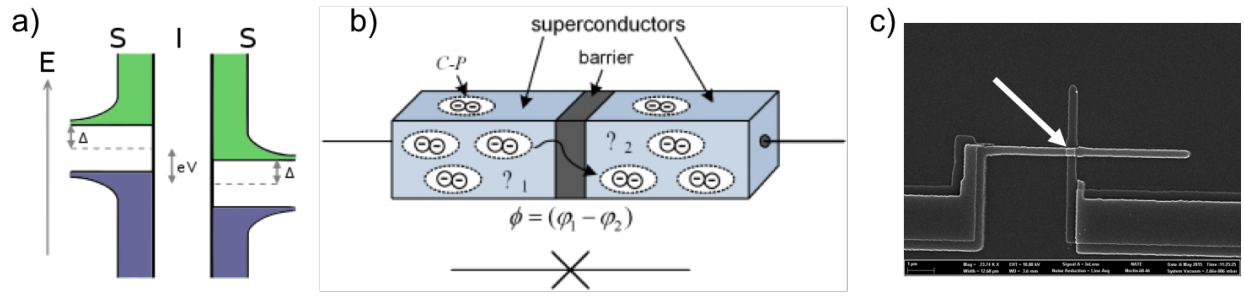

Figure 2.4: a) Energy diagram of a superconducting tunnel junction, which is a specific realization of a Josephson junction. The vertical axis represents the energy, and the horizontal axis represents the density of states. The dashed lines represent the Fermi energy and Δ is the superconducting gap of the superconductor being used (typically aluminum) b) A schematic of the Josephson junction, with Cooper pairs ("C-P") possessing a phase of φ_1 on the left and φ_2 on the right. It is a many-body effect that leads to all of the C-P having a unified phase on each side of the barrier. c) An SEM image of an Al-AlOx-Al JJ made using the Manhattan method (explained in chapter 5). The arrow is pointing at the junction itself.

can interact with every other Cooper pair, on the same side of the barrier and due to the nature of the Hamiltonian all of the Cooper pairs will have the same phase [19]. We then represent the electronic wavefunction by:

$$\Psi = \prod_k \left(u_k + v_k e^{i\phi_k} c_k^\dagger c_{-k}^\dagger \right) |0\rangle \,, \tag{2.13}$$

where $c_k^\dagger$ is the second quantization creation operator for an electron state of k, and u_k/v_k denote the probability than an electron pair state of empty/filled, and ϕ_k is the phase across the Josephson junction. This phase need not be quantum mechanical, per se, but is treated as such when the associated anharmonicity and quality factor are large enough to access individual states. To access the quantum degree of freedom of the junction, an external voltage V must be applied which leads to a change in the phase across the junction given by:

$$\Psi \to \prod_k \left(u_k + v_k e^{i[\phi + i(2e/\hbar)\int V dt]} c_k^\dagger c_{-k}^\dagger \right) |0\rangle \,. \tag{2.14}$$

The corresponding change in the phase is then given by:

$$\frac{d\phi}{dt} = \frac{2eV}{\hbar}. \tag{2.15}$$

This then gives the well-known phase evolution equation of a Josephson junction:

$$V = \frac{\hbar}{2e}\frac{d\phi}{dt}. \tag{2.16}$$

Then, to better understand the time evolution of a system, we consider the general equation for inductance given by:

$$V = L\frac{dI}{dt} = L\frac{d\phi}{dt}\frac{dI}{d\phi}, \tag{2.17}$$

and the corresponding current of a Josephson junction given by:

$$I(t) = I_0 \sin(\phi(t)). \tag{2.18}$$

With this knowledge, we can combine (2.18) and (2.17) to relate the critical current of a junction to its inductance:

$$L_J = \frac{\Phi_0}{2\pi I_0 \cos\delta}, \tag{2.19}$$

where I_0 is the critical current of the junction. When fabricating these junctions, the critical current can be well approximated by the room temperature resistance and junction size, which give rise to the following relation:

$$I_0 = \frac{\pi\Delta}{2eR}\tanh\left(\frac{\Delta}{2k_BT}\right), \tag{2.20}$$

where Δ is the BCS superconducting gap of the material (figure 2.4a). In principle, one could use a larger gap, which would require quasiparticles of higher energy be present in order to create an undesired tunneling event, as a method to improve qubit lifetime. When

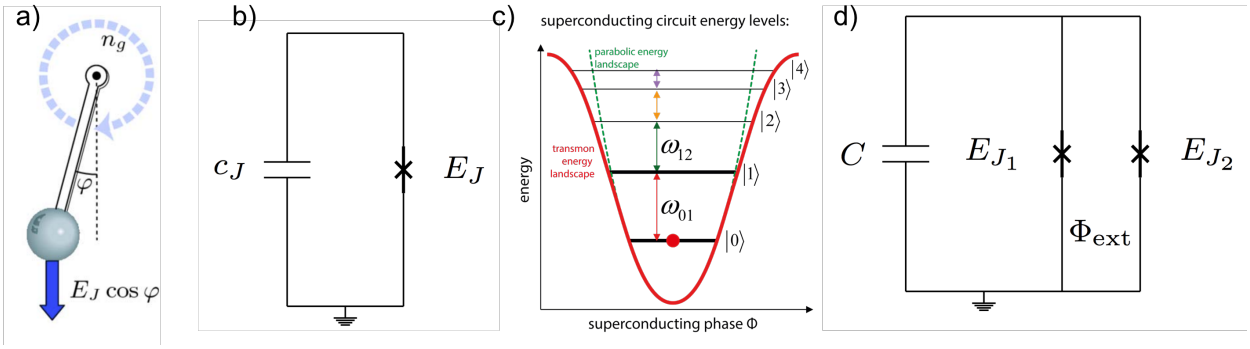

Figure 2.5: a) The transmon can be viewed as an anharmonic oscillator, which is equivalent to a mass swinging on a pendulum, but now with large angle φ to account for its non-linearity. b) The circuit for the initial transmon qubit. c) The energy levels of the transmon qubit which result from a slightly anharmonic well. d) When using a split tunnel junction one can 'Zeeman' tune the artificial atom in the same way an electron can be tuned.

one follows the Hamiltonian solution to equation (2.14), it is equivalent to a spin 1/2 particle (We will see in a bit, when a fluxonium has a large enough inductance, the assumed periodic boundaries no longer exist making this spin 1/2 characteristic break down [64], as is the case for the heavy fluxonium presented in this thesis).

2.2.2 Accessing a Two-level system: The transmon

An Anharmonic Oscillator

Now that we have the necessary Josephson effect, we shall apply it to the (currently) most commonly used quantum bit: the "transmon". The transmon, shown in figure 2.5, consists of a Josephson junction, shunted by a large capacitance. Using the phase basis and taking the Josephson energy derived above, the Hamiltonian is given by:

$$H_t = -4E_C \frac{d^2}{d\phi^2} - E_J \cos\phi \tag{2.21}$$

Intuitively you can view this as being rather similar to the LC-Oscillator discussed above, but with a slight non-linearity added. The anharmonicity is a way to measure the non-

linearity of the circuit, defined as:

$$\alpha = E_{12} - E_{01}, \tag{2.22}$$

which, in the case of the transmon, is just given by the charging energy of the circuit:

$$\alpha_{\text{transmon}} \sim -E_C. \tag{2.23}$$

Furthermore, in the case of the transmon qubit, we can estimate the resonance of our ω_{01} transition by the following relation:

$$\omega_{01} \approx \sqrt{8E_J E_C}. \tag{2.24}$$

As we will see shortly, the anharmonicity of the heavy fluxonium does not have a simple relationship like (2.23) because the ω_{01} transition tunes considerably, while the ω_{02} transition is nearly flat over the entire flux quantum. However, the plasmon transition of the heavy fluxonium can be decently approximated by equation (2.24), as these transitions are transmon-like and follow similar selection rules.

A tunable two-level system

In analogy to Zeeman tuning of an electron (nature's two-level system), we can create a transmon that is tunable by simply putting two Josephson junctions in parallel. This is the 'split tunnel junction' and has a resulting tunable E_J that is given by E_{J_1} and E_{J_2} as shown in figure 2.5d. In this case, the Hamiltonian of the split junction is given by:

$$H_J = (E_{J_1} + E_{J_2}) \cos\left(\pi \frac{\Phi_{\text{ext}}}{\Phi_0}\right) \cos\theta - (E_{J_1} - E_{J_2}) \sin\left(\pi \frac{\Phi_{\text{ext}}}{\Phi_0}\right) \sin\theta, \tag{2.25}$$

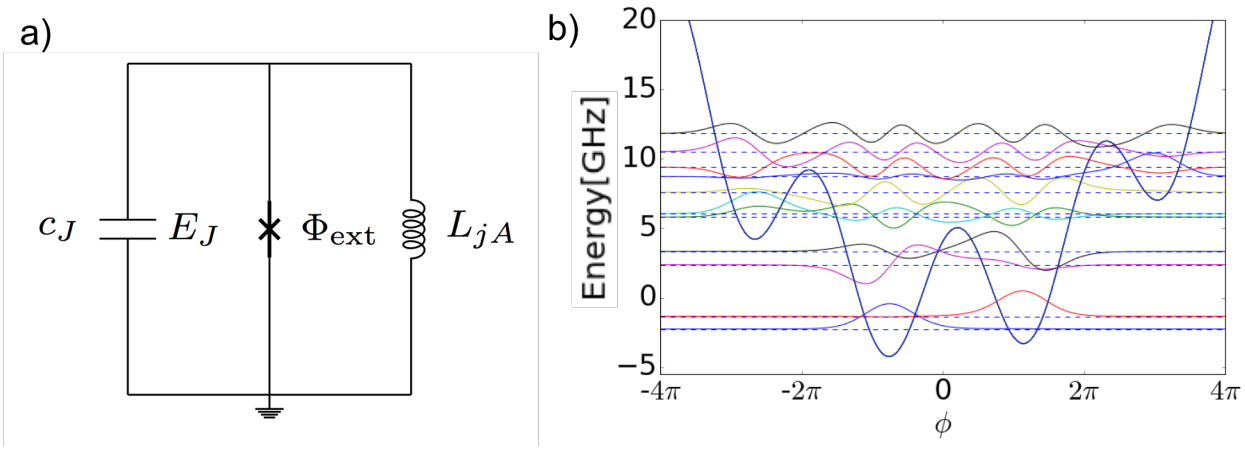

Figure 2.6: a) The original fluxonium circuit with the capacitance of the circuit being determined primarily by the parallel-plate capacitance of the small Josephson junction E_J. b) The plethora of energy levels associated with the fluxonium Hamiltonian.

where θ is the average phase of the junctions, and $\phi = \theta_1 - \theta_2 = 2\pi\frac{\Phi_{\text{ext}}}{\Phi_0}$. The asymmetry, d, in the two junctions will determine how the qubit energy can be tuned, as governed by:

$$d = \frac{E_{J_1} - E_{J_2}}{E_{J_1} + E_{J_2}}. \tag{2.26}$$

In the case of perfectly symmetric junctions we can achieve a tunability down to zero. However, this is impractical as there will always be some slight asymmetry in the junctions. More usefully, one can intentionally engineer asymmetric junctions as a way to reduce the range of tunability. In the case when the qubit coherence time is limited by flux noise, this asymmetry can help reduce the flux slope of the qubit transition and thereby improve the coherence. This tunable E_J element may also prove to be useful for future implementations of the heavy fluxonium, where the barrier can be tuned to a low value at points when one wishes to do gates, and tuned back to large values when long-lived states are desired.

2.2.3 An Engineered 'Qudit': The fluxonium

While a transmon qubit is well approximated by a two-level system, another artificial atom – one which requires more energy levels to be appropriately described – is the fluxonium [15]. Shown in figure 2.6a, the fluxonium is one of the realizations of a 'quantum digit' where the system is no longer well approximated by just two levels and in order to appropriately describe the system, many levels must be accounted for. In the case of the heavy fluxonium, this actually ends up being a useful asset, as it will help ensure that we will have a measureable shift in the cavity resonance for different quantum states, even with minimal dipole matrix elements (as will be the case of the fluxonium circuit). The details of this circuit will be covered in the next chapter.

2.3 Protected Qubits

2.3.1 Improving Qubit Lifetime: Fermi's Golden Rule

As stated in the abstract, the goal of this thesis project was to engineer a qubit that possess long coherence times as this will be essential to realize a fault tolerant quantum computer. In order to understand how one can improve the lifetime of a qubit we take a look towards the coupling rate (and consequently the lifetime) of two different quantum states when acted upon by an arbitrary Hamiltonian. Such a relation is given by Fermi's Golden Rule:

$$\Gamma_{01} = \frac{1}{T_1} = \frac{2\pi}{\hbar} \left|\langle 0|A|1\rangle\right|^2 S(\omega). \tag{2.27}$$

Here, $S(\omega)$ is the noise spectral density of the qubit environment, and the preceding term is the coupling of our two states of interests from the generic measurement operator A. The large improvement in coherence times that superconducting circuits have experienced thus far is the result of a significant effort in improving the noise of the environment through careful

microwave engineering and rather complicated material science approaches to reduce $S(\omega)$. While this avenue will still prove to be useful, it will also become increasingly complicated to suppress noise terms that are inherently a part of the materials and systems being used. To this end, we take a look at the preceding term, $|\langle 0|A|1\rangle|^2$, as a way to suppress the coupling of two states, and thereby increase their lifetime. Unsurprisingly, if we turn down the coupling of our states we will have an improved T_1, but we will also suppress the desired coherent coupling. This suppression of the coherent coupling will result in increased gate times, which will ultimately make the increased lifetime not as useful. However, we can borrow a trick from atomic physics to realize a system that has both a suppressed dipole element, as well as decent coherent coupling via the use of a higher auxiliary level.

2.3.2 Engineering a Λ system: The heavy fluxonium

Traditionally, a Λ system is comprised of a ground and metastable excited state, coherently coupled through a third intermediate state. Λ systems are ubiquitous in atomic physics, realized using a combination of selection rules [25], relative strengths of optical-dipole and microwave hyperfine matrix elements [26], and large differences in frequency scales in conjunction with the 3D density of states (decay rate $\gamma \propto \nu^3$) [27], In the next chapter we will see how one can adjust the various energy values of the fluxonium circuit to realize isolated ground state wavefunctions, and to ultimately create a Λ system, in which local ground states do not communicate with each other, but can be coupled via an auxiliary higher energy level - akin to atomic physics schemes.

2.4 Artificial Atom 'Periodic Table'

Here I just want to make a quick allude to nature's engineering: The periodic table. While natural atoms are produced inside the cores of suns, they are ultimately described by some complex Hamiltonian. We are able to solve this Hamiltonian exactly for the hydrogen atom,

and after that we have to make approximate solutions. One of the benefits to a quantum computer is that we will be able to further improve these approximate solutions [28]. But, just in the way that an atom is unique in its (albeit complex) Hamiltonian, we too can make atoms with unique Hamiltonians each having special properties which allow us to study different realizations of physical phenomena. It is in this way that we are able to begin to create an "artificial atom periodic table". With many different realizations of such artificial atoms being realized, we really are just in the initial phase of this exciting field, and with no doubt there will be some interesting physics to arise from future artificial atoms, and their interactions with light.

CHAPTER 3

FLUXONIUM THEORY

3.1 Constructing the Interaction between light and matter

3.1.1 The 'matter' Hamiltonian

When working in the phase basis, one can find the Hamiltonian of a circuit by initially writing the Lagrangian, L, defined by the phase across each node of the circuit. The phase difference is simply dependent on the established rules set by Kirchhoff's laws. Then, to obtain the Hamiltonian, one simply applies the Legendre transformation $\mathrm{H} = \sum_i \dot{q}_i \frac{\partial L}{\partial q_i} - L$. In the case of the fluxonium circuit (figure 2.6a), we obtain the following Hamiltonian:

$$H_f = -4E_C \frac{\partial^2}{\partial \phi^2} - E_J \cos(\phi - \Phi_{ext}) + \frac{1}{2} E_L \phi^2. \tag{3.1}$$

In the initial experiments observing coherent oscillations across Josephson junctions [3, 4], the above Hamiltonian was a general description of the qubit. However, in this situation alone we expose our quantum states of the circuit directly to the 50Ω environment, which introduces a substantial amount of noise (represented by the $S(\omega)$ in Fermi's Golden Rule) and will degrade the quality of device. As we will see shortly, by simply coupling this component to a harmonic oscillator, we are able to realize the circuit equivalent to Cavity QED [5], which also serves to isolate us from the noisy microwave environment and will help greatly improve the quality factor of the devices.

State Label

In the fluxonium circuit, there are two different characteristic transitions: Inter-well Fluxon transition and intra-well plasmon transitions. Fluxon transitions will be the suppressed transitions, while the plasmon transitions will have order unity coupling. We denote the

various energy levels, as shown in figure 3.1b, by their fluxoid number with a subscript, and then the corresponding state within that well (e.g. $|g\rangle$,$|e\rangle$,$|f\rangle$). The subscript will reverse at zero flux quanta and half flux quanta, due to the ordering of the energy labels.

3.1.2 Physical Intuition of Hamiltonian

Effect of circuit components on wave functions

As shown in figure 3.2, each circuit component has a simple physical representation in our energy landscape. The inductive element, E_L, provides the quadratic term of the Hamiltonian and, as a consequence, determines the curvature of the potential energy. Naturally, the flux dependence of fluxon transitions, which associated with states that are localized in the local minima of each well, will depend heavily on this quadratic curvature. For a device that is limited by flux noise (as was the case for the device presented in this thesis), a reduced flux-slope for our energy transition should result in an improved T_2. As can be seen in figure 3.2a, as we increase the inductance (or decrease the inductive energy), the quadratic term becomes shallower. Furthermore, the number of wells that have local ground states will increase. Interestingly, in the limit of an infinite inductance, a capacitively shunted fluxonium reaches the same dynamics of a transmon qubit [52]. E_J, provided by the small Josephson junction, determines the barrier height as can be seen in figure 3.2a. And E_C is the effective mass of a fictitious particle living inside the energy landscape. Both the height of the barrier, and the effective mass of the fluxonium will determine the tunneling rate of fluxon-like transitions. As we increase the circuit capacitance, we will increase the effective mass of a particle which will consequently suppress the coupling of the low-lying ground states (see figure 3.2c). The same effect could be achieved by increasing the barrier height of the junction (see figure 3.2a), however this cannot be leveraged indefinitely because an increase in the barrier height will ultimately reduce the non-linearity of our small junction, which is required to address specific quantum states. More specifically, in order for our circuit to

ensure fluxons tunnel primarily through the small junction, it is required that [15]:

$$N \exp^{-8R_Q/Z_{JA}} \ll \exp^{-8R_Q/Z_J}, \tag{3.2}$$

where $R_Q = h/(2e)^2 \approx 1k\Omega$ is the resistance quantum, Z_{JA} is the impedance of a single large junction in the junction array, N is the number of large junction and Z_J is the impedance of the small junction.

Tightening of Energy Levels

I would like to also note, that as we increase the capacitance of the circuit, the bands of our energy levels will begin to be tightened. (In particular, take note of the tightening of the energy levels in the panel of figure 3.2c). In an experimental sense, this will become important when we begin to try and coherently address the desired states and do not want to populate other levels. The reason is that, as we add capacitance, we reduce the tunneling matrix element, which requires that one drives at high powers to coherently couple the states of interests. However, the tightening of the bands will also increase the risk that we will begin to off-resonantly drive other transitions. However, this band tightening is also interesting when one begins to consider the limits of very large inductances, what is now being deemed the 'hyper inductance' [65]. In the limit that we have a large E_J/E_C ratio and a sufficiently large inductance, our heavy fluxonium now begins to resemble the potential energy landscape of multiple transmon-like qubit wells. The device presented in this thesis has an E_L sufficiently large to realize a mixed band coupling (e.g. at $\Phi_{\text{ext}} \sim 0$ there is a band tightening of $|e_0\rangle$ with $|g_{-1}\rangle$ and $|g_1\rangle$ or $|f_0\rangle$ with $|e_{-1}\rangle$ and $|e_1\rangle$), but not significant enough to realize a band tightening of only low-lying ground states. It is this band tightening, in conjunction with the resonator hybridization (to be explained below), that gives rise to the adoringly called 'wolverine' features seen in figures 6.7a (the 2-photon

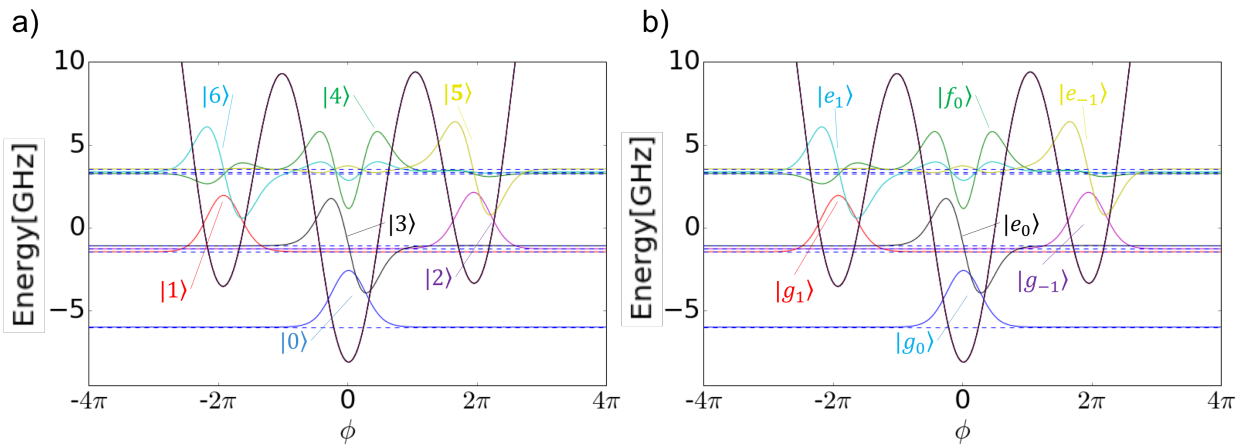

Figure 3.1: a) State labeling of wavefunctions based on the order, starting with the lowest energy being labeled as $|0\rangle$, the next as $|1\rangle$ and so on. This labeling scheme, however, is dependent on the flux value of interests and can lead to complications in interpretation of various energy levels. b) State labeling according to wavefunction well occupation and the correspond energy level within this well. This labeling scheme helps to point out the different sort of transitions of either intra-well plasmon transitions or inter-well fluxon transitions. plasmon-like transitions are akin to transitions in a transmon qubit and have similar selection rules, whereas fluxon-like transitions are unique to the fluxonium and correspond to the persistent current state of the device and can be suppressed to achieve long qubit lifetimes.

features), 6.11a (photon assisted transitions), or 6.12 (plasmon assisted transitions).

If we instead take the limit $L \to \infty$, one will find the potential energy landscape of the fluxonium begins to resemble that of a transmon [52]. However, it is never the case that the inductance is truly infinite, and therefore the degeneracy of our fluxonium circuits will be lifted ever so slightly, giving a larger width to our bands. In such as case, where the inductance will be large enough to have the low-lying ground states be nearly degenerate, there will be the opportunity to experimentally observe Bloch oscillations [51, 52], which could serve to close the metrological loop and give a fully self-consistent current standard [51].

The fluxonium qubit is essentially a flux qubit with a very large inductance. Though the Hamiltonian is the same, the resulting wave functions have a fundamentally different nature. To realize an inductance value large enough to engineer a fluxonium circuit we must make use of non-geometric means to realize such large inductance values. There are two possible

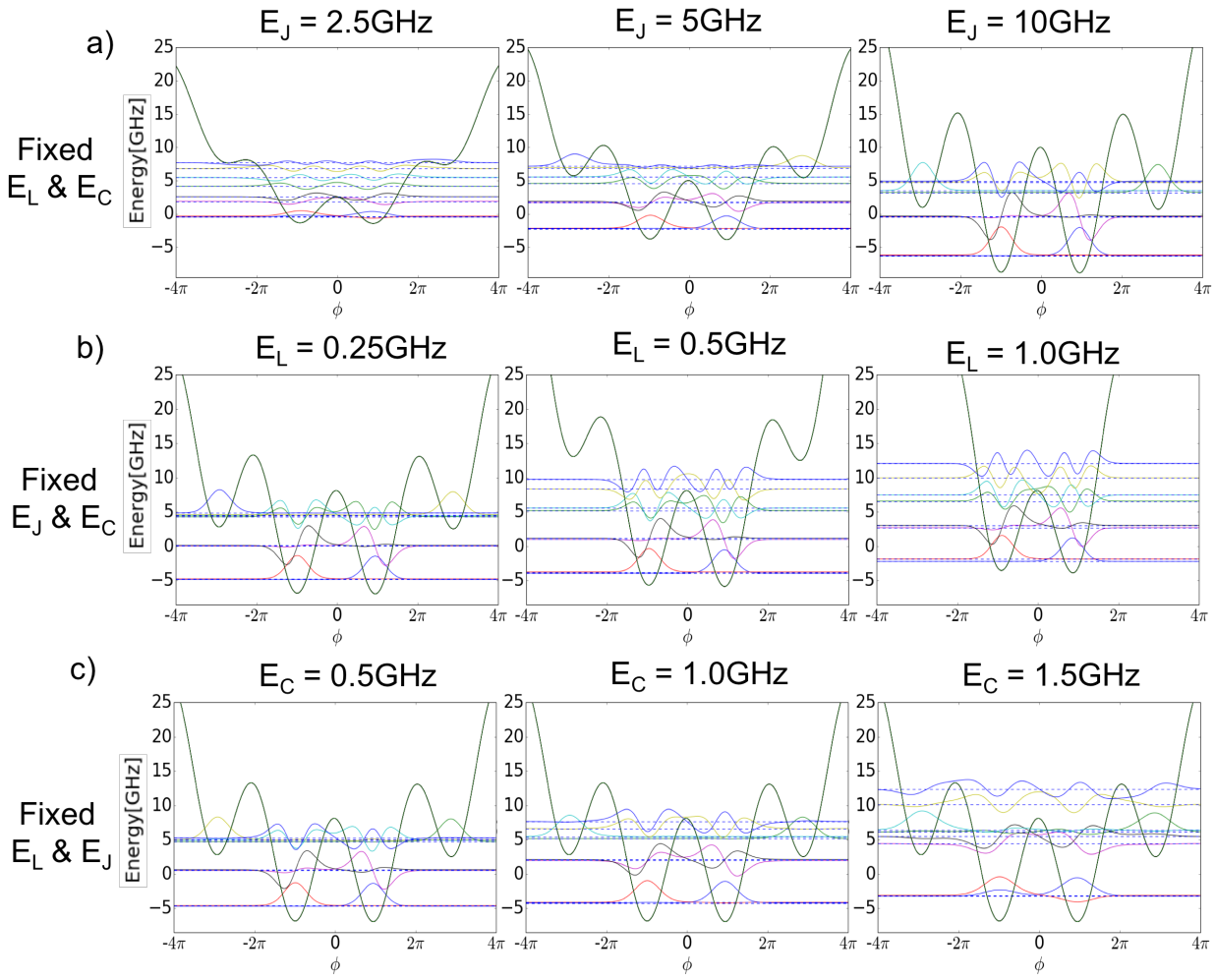

Figure 3.2: Potential energy landscape of the heavy fluxonium circuit, changing the energy values of the three circuit components, and demonstrating the change in the potential energy landscape and the corresponding change on the eigenenergies. When the energy values are fixed, they are fixed to the values realized in the main device of this thesis, i.e. E_J=8.11GHz, E_C=0.43GHz, E_L=0.24GHz. In the first row, we fix E_L and E_C and increase E_J as we move right. We can see that as E_J is increase, the barrier height is also increased, consequently suppressing the tunneling matrix element of our wavefunctions. Through implementing a tunable E_J we can use this to our benefit as a way to realize a tunable magnetic moment like in [11], but with fast flux in our 2D qubit design. In the second row, we fix E_C and E_J and increase the inductive energy. We can see as the inductive energy is lowered, there is the onset of multiple wells, where we are in a four well limit at half flux in the case of the heavy fluxonium. In the final row, we fix E_J and E_L and increase the charging energy. This demonstrates that as the charging energy is decreased, the tunneling between wells is decreased, and our energy transitions are brought into tighter bands.

means to realize these larger inductances: either by using large Josephson Junctions or via the use of kinetic inductance. I will review the requirements in either situation to realize an ideal inductive component and all of the various parameters that must be accounted for to ensure an ideally behaving inductive element.

Suppression of dipole matrix element vs sweet spot

Generally, in superconducting circuits, one has an ideal point of operation in regards to the sensitivity to flux noise when the slope of the energy transition, relative to flux, is shallow. This point is generally called the 'flux sweet spot'. Our approach to improve the lifetime of the device, however, makes this sweet spot go away (as seen in figure 3.3). There is ultimately a tradeoff between having a flux sweet spot (which is good to obtain a long lived T_2) and a very small dipole matrix element for a long T_1. In figure 3.3, one can see this loss through the increased capacitance of the circuit, as well as a suppression of the 'triplet' coupling between $|g_1\rangle$ and $|g_{-1}\rangle$ (this suppression/sweet spot loss also occurs for increased E_J). For future iterations of the device, we can engineer the circuit to have an optimal tradeoff between a small dipole element, and good sweet spot. Another option, however, would be to reduce the slope of the energy transition altogether, by further increasing the inductance (see figure 3.3d).

Perspectives provided by different bases

In the above discussion, the fluxonium was presented from the perspective of the phase basis. This feels like a good way to consider the Hamiltonian, as the desired long-lived quantum states have distinct phases and the presented perspective gives a natural way to understand how to reduce tunneling between wells and engineer the long-lived T_1 of the device. However, this perspective alone does not do justice to the complex nature of the device or provides much understanding of the different coupling mechanisms of our distinct transitions. To this

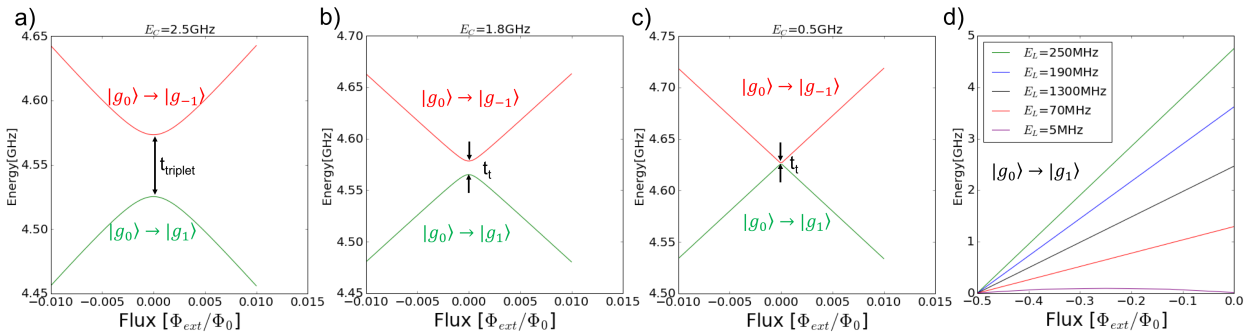

Figure 3.3: Suppression of the tunneling matrix element also comes with a loss of the sweet spot, which is ideal for a long T_2 coherence time. a-d are an increasing capacitance (the effective mass), which results in a decrease in the tunneling between $|g_0\rangle$ and $|g_1\rangle$, but also the loss of a sweet spot. A tradeoff between these two factors will be important when engineering this qubit for the purpose of quantum information.

end I would like to quickly discuss an alternative perspective. In the limit:

$$E_J \gg E_C \gg E_L, \tag{3.3}$$

there will exist two distinct transitions: intra-well plasmon transitions or inter-well fluxon transitions. In this limit, we can rewrite the fluxonium hamiltonian [53] as:

$$H_f = H' + H_{\text{ind}}, \tag{3.4}$$

where $H' = 4E_C N^2 - E_J \cos\varphi$. H' is very similar to that of the Cooper pair box, but without satisfying the periodic conditions, but instead follows quasi-periodic boundary conditions similar to Bloch's theorem [53]. As such, the eigenstates of H' are Bloch states such that:

$$H' \left|p, s\right\rangle = \epsilon_s(p) \left|p, s\right\rangle, \tag{3.5}$$

where $\epsilon_s(p)$ is the band dispersion relation for a given 'band'. In this situation, we can rewrite the fluxonium Hamiltonian, neglecting inter-band coupling, as $H_f \approx \sum_s H_s \left|s\right\rangle \left\langle s\right|$

where:

$$H_s = \frac{E_L}{2}\left(i\frac{d}{dp} + \frac{2\pi\Phi_{\text{ext}}}{\Phi_0}\right)^2 + \epsilon_s(p). \tag{3.6}$$

H_s is the hamiltonian for each band s. This perspective of the heavy fluxonium is a good complement to the phase basis perspective and will be useful when considering the meaning of (and necessary conditions for) Bloch oscillations in a Josephson junction [53, 51]. Furthermore, this basis is useful for quantizing the circuit using loop charges, where they demonstrate this duality is useful for understanding Josephson junctions in large-impedance environments, stating that they behave as nonlinear capacitors supporting quantized flux [56].

3.1.3 Defining Different Transitions

Fluxon Transistions

The transitions that are engineered to be long lived will be the transitions associated with a shift in the phase of the qubit. In other words, these are inter-well fluxon transitions (or the persistent current states):

$$|g_0\rangle \rightarrow |g_1\rangle\,, \tag{3.7}$$

$$|g_0\rangle \rightarrow |g_{-1}\rangle\,. \tag{3.8}$$

Plasmon Transitions

Intra-well plasmon transitions are transmon-like in their nature, facing similar selection rules. Examples of these transition are:

$$|g_0\rangle \rightarrow |e_0\rangle \tag{3.9}$$

$$|g_0\rangle \rightarrow |f_0\rangle \tag{3.10}$$

$$|g_1\rangle \rightarrow |e_1\rangle \tag{3.11}$$

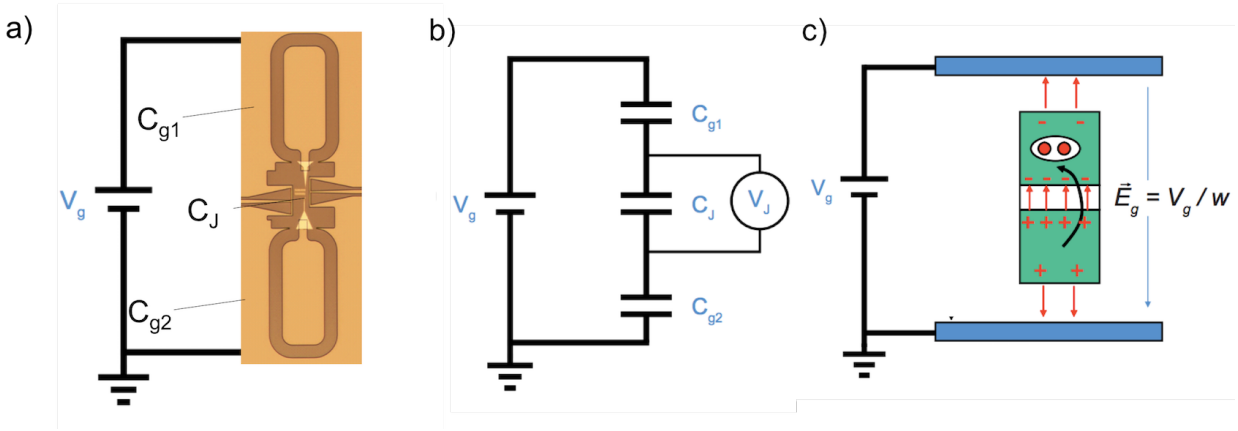

Figure 3.4: a) Image of fluxonium Sample with a cartoon voltage which arises from a photon being present inside the readout resonators (capacitively coupled, but not seen in the photo) b) A voltage divider diagram for a capacitively coupled junction with capacitance C_J c) This can be approximated as a dipole inside an electric field to gain intuition as to how state readout works.

A combination of both

In the circuit, we can have a combination of plasmon and fluxon transitions. These transitions will be critical in completing our Raman gates. Some examples of these transitions are:

$$|g_0\rangle \rightarrow |e_{-1}\rangle \tag{3.12}$$

$$|g_1\rangle \rightarrow |e_0\rangle \tag{3.13}$$

3.1.4 Coupling to fluxonium: Adding the 'light'

Basic Principle: Voltage Divider

As discussed in the introductory chapter, by adding an LC-oscillator we are able to realize an equivalent system to cavity QED and either begin to study the interaction between the cavity and qubit, or simply to use it as a way to isolate the qubit from the noisy 50Ω environment and thereby improve the coherence of our quantum system. There are two primary ways in which we can couple our light and matter systems: either capacitively

or inductively (In Cavity QED the interaction is inherently a combination of both of the electric and magnetic fields as the coupling is due to photons of light bouncing back and forth between two mirrors and light is inherently an electromagnetic field. This difference of circuit QED can be leveraged to realize the strong coupling limit - and even possibly the ultra-strong coupling regime [68].) Ultimately either approach can be viewed as creating a voltage divider, and it is the resulting voltage placed across the Josephson junction (V_J in figure 3.4b) that determines the strength of coupling between our light system and matter system. This voltage V_J can be larger by increasing the ratio of voltage division, or by increasing the impedance of the readout resonator, as this will result in a larger voltage placed across the resonator when a photon is present in the resonator.

Given the larger capacitor pads of our heavy fluxonium design, it is easy enough to place one of the pads next to the readout resonator and thereby capacitively couple to the readout resonator. The resulting Hamiltonian is given by:

$$H_S = H_f + h\nu_r a^\dagger a + \sum_{j,k} hg \left|j\right\rangle \left\langle k\right| \left\langle j|\hat{n}|k\right\rangle (a^\dagger + a) \tag{3.14}$$

This is the quintessential Hamiltonian studied throughout the cQED field and the fluxonium circuit, and will the basis of this thesis' work. In the outlook section I will discuss the possibility to intentionally engineer the coupling term of this Hamiltonian as a way to realize ultra-strong coupling, in which the rotating wave approximation breaks down and one can study the interaction of light and matter in a regime that is simply inaccessible in cavity QED [12].

3.1.5 Measuring the fluxonium State - χ-shift

As is carefully described in "Circuit QED" [7], the readout of the qubit state is achieved by measuring the resonate frequency of the cavity mode. Due to an effective stark shift

this resonate frequency will depend on the state of the qubit, which then provides a means to perform a quantum non-demolition (QND) measurements. The strength of this signal, however, will depend on the magnitude of the shift, which is determined by the width of the cavity resonance and the magnitude of the shift.

Better χ-shift with readout close to plasmon mode

When capacitively coupled to our read out resonator, we are able to readout the state of the qubit by measuring the transmission of the readout resonator. The χ-shift in the readout allows for us to have a state-dependent QND measurement. However, as we suppress the coupling of our states, we will make the dipole matrix element smaller, which naively would also suppress the χ-shift. However, in the case of the fluxonium circuit, there are many different levels that contribute to the χ-shift of the resonator [13]:

$$\chi_j = \frac{g^2}{16E_C^2} \sum_{k \neq j} \frac{\omega_{jk}^3}{\omega_{jk}^2 - \omega_r^2} \times (d_{jk})^2 \tag{3.15}$$

where d_{jk} are the coupling matrix elements of the transition $|j\rangle \rightarrow |k\rangle$, and ω_r is the readout resonator frequency. What is important to note here is that by placing the readout mode close to our primary plasmon transitions, we are able to still resolve our low-lying ground states $|g_0\rangle$ and $|g_1\rangle$, even though we are also suppressing their dipole matrix element. As we will now see in the case of the heavy fluxonium, this can also serve as a way to create a new form of coupling which will allow for fluorescent readout.

3.1.6 Hybridization of Plasmons and Resonator: Plasmonic Coupling

Defining Dispersive Regime

A very useful aspect of the circuit QED architecture is the ability to engineer the system to be in a "dispersive strong" regime, where a qubit can be far detuned from the readout cavity mode while still having enough coupling strength and a long-lived quantum states allowing one to perform coherent gates. Quantitatively this can be broken down into several characteristic regimes as fully discussed in [7]. Generally speaking these regimes are characterized by the coupling strength to our readout resonator, g, the detuning of our qubit, Δ, and the loss rates of either the readout resonator (Γ) or the qubit (γ). However, in the case of the heavy fluxonium circuit presented in this thesis, we will have a slightly different form of coupling, deemed plasmonic coupling. This form of coupling arises because the plasmon transition in our heavy fluxonium circuit does not tune very much with an applied external flux (this is due to the large inductance), while our fluxon transition tunes quite dramatically with flux. As a result of that, it is possible to realize a coupling limit in which the fluxon transition ($|g_0\rangle \rightarrow |g_1\rangle$) is dispersively coupled to the readout but the plasmon transitions ($|g_0\rangle \rightarrow |e_0\rangle$,$|g_1\rangle \rightarrow |e_1\rangle$) are non-dispersively coupled to our readout resonator. To quantify this more rigorously, we are in the dispersive regime when we satisfy [13]:

$$|\Delta_{j,ll'}| \gg |g_{j;ll'}|\sqrt{n_j+1}, \tag{3.16}$$

where n_j is the number of photons in our readout resonator and l and l' are the transition states of interest in the qubit circuit. In other words,

$$g_{j,ll'} = g_j \langle l|n|l'\rangle \tag{3.17}$$

$$g_j = 2e\beta_j V_j^{\mathrm{rms}} \ , \tag{3.18}$$

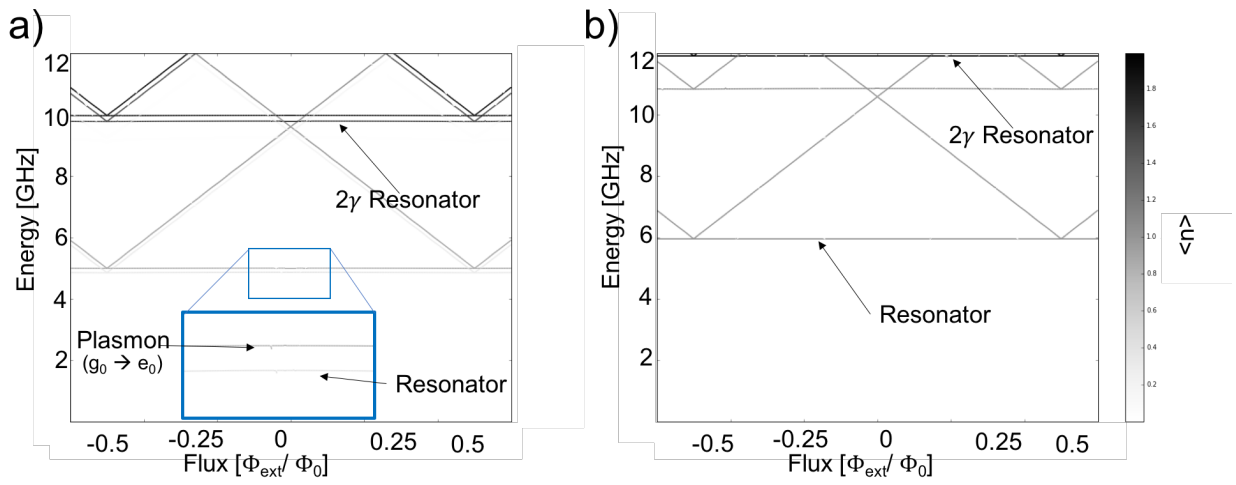

Figure 3.5: The photon number of various transitions in a capacitively coupled heavy fluxonium circuit with two different readout resonator frequencies to demonstrate the hybridization of qubit modes with resonator modes. a) Experimentally realized values demonstrating the strong hybridization of our readout resonator and $|g_0\rangle \rightarrow |e_0\rangle$ plasmon mode. We can also see in this plot that our $|g_0\rangle \rightarrow |f_0\rangle$ transition hybridizes with the two-photon mode of the resonator. b) The results of theoretically detuning our readout resonator far away from the plasmon mode, which results in a pure resonator and a plasmon mode with no hybridization.

where V_j^{rms} is the RMS voltage on our readout resonator when there are j photons present. Furthermore, we have the $\Delta_{j,ll'} = \omega_{ll'} - \omega_{\text{res}_j}$ where j is, again, the number of photons present in the readout resonator.

Non-dispersive Plasmon Coupling

For the plasmon transition $|g_0\rangle \rightarrow |e_0\rangle$ we have $|g_{1,02}| \approx$79MHz$\cdot g_{02}$. The 79MHz is determined the value of the capacitance between the qubit and the readout resonator, and g_{02}, generally a function of the applied external flux is given by:

$$g_{02} = g_{g_0 e_0}(\Phi_{\text{ext}}) \tag{3.19}$$

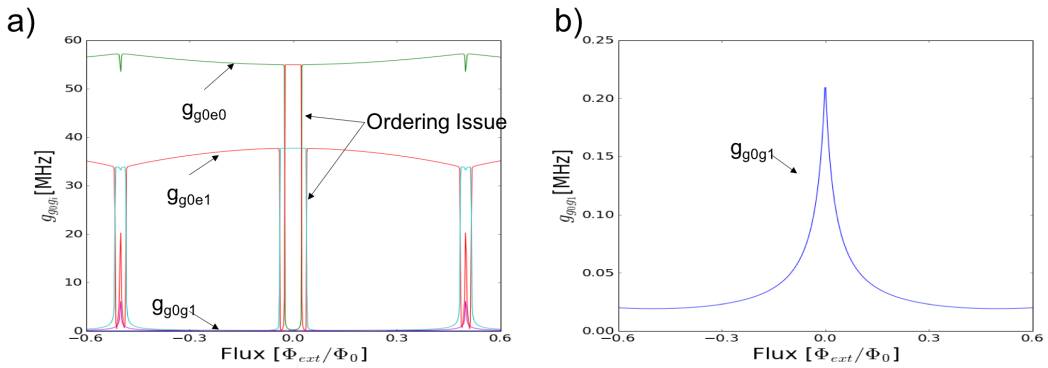

Figure 3.6: a) The coupling element with matrix elements of the transitions considered for the plasmon transitions and the fluxon transition b) A close up zoom of the fluxon transition matrix element, because it cannot be seen clearly in subfigure a) due to its relatively small value.

As this is a transmon-like transition, this transition is allowed by the corresponding selection rules and gives us that $|g_{1,02}| \approx 55\text{MHz}$ at $\Phi_{\text{ext}} \approx 0$. As we will see in the experimental results chapter, we have that $|\Delta_{1;02}| \approx 150\text{MHz}$, giving that $|\Delta_{1,02}| \approx 3|g_{1;02}|$, which does not satisfy the condition for dispersive coupling in equation 3.16. This regime is often seen in the tunable transmon qubit at the appropriate flux point in which both the resonator and transmon energy levels are in resonance, and gives the quality of having a 'phobit' or 'quton' as said in [7]. However, due to the shallow quadratic potential of the heavy fluxonium circuit, we have this energy level in this non-dispersive regime for the entire flux quantum. In this case, the plasmon mode is always in a non-dispersive regime, and leads to the realization of photon/plasmon-assisted transitions. However, as we will now see, this non-dispersive limit is not the case for our fluxon transition.

Dispersive Fluxon Coupling

In the case of our fluxon transition, we have intentionally suppressed the coupling matrix element, as this is useful for increasing our qubit lifetime, as discussed in the introduction. This will inherently put the device much further into the dispersive regime. Even when

the $|g_0\rangle \rightarrow |g_1\rangle$ transition is at its highest point ($\omega_{g_0g_1}(\Phi_{\text{ext}} = 0)$ ≈4.65 GHz) we have $\Delta^{\phi_0}_{1;01}$ ≈300MHz and $g_{1;01} \approx 0.2$MHz, putting us decently into the dispersive regime. Furthermore, due to the tunable anharmonicity of the heavy fluxonium we have the ability to tune our fluxon transition nearly all the way to a sub-MHz value ($\omega_{g_0g_1}(\Phi_{\text{ext}} = 0) \approx 0.5$MHz, though this value has not been directly measured experimentally) and thereby further put us into the dispersive regime. The exact relation of the coupling $g_{g_0g_1}$ can be seen in plot 3.6b.

Qubit-Resonator Hybridization

The plasmonic coupling results in the hybridization of our readout mode with the qubit mode. What this means is that a photon in the resonator has some probability of turning into a plasmon excitation in the qubit and a plasmon excitation in the qubit can turn into a photon in the resonator. To characterize this hybridization quantitatively, we will simply take our coupled Hamiltonian, H_S, and act the number operator on the various states as a way to identify the level of hybridization. The specific experimental realization of plasmonic coupling in this device is discussed in the experimental results chapter. In figure 3.7 we can see that when the resonator is exactly on resonance with the plasmon transition we have a 50/50 hybridization of our modes. When ω_{Res} is detuned away from our resonator by the bare coupling capacitance, we get a 75/25 hybridization. In figure 3.7b, we increase the capacitance of our coupling capacitor, and demonstrate that the hybridization range increases.

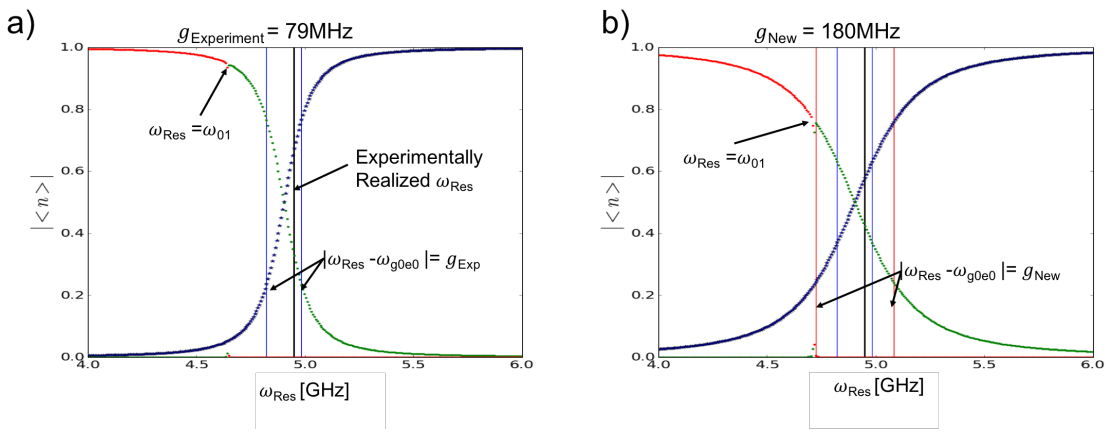

Figure 3.7: a) The photon number of either our plasmon mode or resonator mode as a function of the resonator frequency for the experimentally realize coupling capacitance parameters. As can been seen the hybridization results in a 50/50 mixture for a readout resonator on resonance with the uncoupled plasmon mode and when detuned away by the bare capacitive coupling (which does not take into account the charge matrix elements) we have a rough hybridization of 75/50. b) A similar plot to what is shown in part a, but for an increased bare coupling capacitance, showing that the amount of hybridization depends on the detuning relative to the coupling.

3.1.7 Appropriate Quantum Numbers in Hybridized Circuit

Extreme Hybridization and Appropriate Quantum Numbers

In the limit where the bare resonator is precisely on resonance with our plasmon mode, we will have an even mixture of photon and plasmon modes (see figure 3.7), and they lose their independent nature, similar to the quton of phobit states of a transmon in resonance with a readout resonator [7]. To understand this, consider the states:

$$|e_0, 0_r\rangle \tag{3.20}$$

and

$$|g_0, 1_r\rangle \tag{3.21}$$

Because they lose their independent nature, it no longer makes sense to simply write down one or the other. Instead we would write down:

$$|\psi_+\rangle = \left(|e_0, 0_r\rangle + |g_0, 1_r\rangle\right)/\sqrt{2} \tag{3.22}$$

$$|\psi_-\rangle = \left(|e_0, 0_r\rangle - |g_0, 1_r\rangle\right)/\sqrt{2} \tag{3.23}$$

This is analysis also applies for our other plasmon mode:

$$|\psi'_+\rangle = \left(|e_1, 0_r\rangle + |g_1, 1_r\rangle\right)/\sqrt{2} \tag{3.24}$$

$$|\psi'_-\rangle = \left(|e_1, 0_r\rangle - |g_1, 1_r\rangle\right)/\sqrt{2} \tag{3.25}$$

where $|g_0\rangle, |e_0\rangle, |g_0\rangle, |e_1\rangle$ all have the some coupling as determined by the bare fluxonium circuit. Interestingly, this hybridization allows for a fluorescence readout of our device and seems to lead to the photon-assisted transitions we see in our device (based on the lack of their appearance in other heavy fluxonium systems we have measured). In the case of the device presented in this thesis, we have a $\sim$60/40 hybridization as the resonator is not precisely in resonance with the plasmon mode, but is detuned by less than the coupling g. To this end, the labeling of transitions in this thesis will not fully account for this hybridization, and just goes with the larger part of the mode to avoid the complicated and unclear labeling of transitions. Interestingly, there are other terms in this that lead to more sophisticated composite transitions which I will introduce below.

Composite Transitions

As will become important for some of the transitions seen in the spectroscopy of our device, I would like to point out a different sort of transition: Composite transitions comprised of fluxonium-like transitions (either flux or plasmon like in their nature) and transition

associated with the gain or loss of a photon in the resonator. These transitions are the result of a hybridization of our readout resonator with the plasmon transition of the plasmon. If we look at the "resonator-like" peak in single-tone spectrum, we find that the resonator blanks out at precisely half flux quantum. This corresponds to two composite transitions coming into resonance with the resonator at precisely half-flux, corresponding with:

$$|g_0, 0_r\rangle \rightarrow |g_1, 1_r\rangle \tag{3.26}$$

and

$$|g_1, 0_r\rangle \rightarrow |g_0, 1_r\rangle \tag{3.27}$$

These composite transitions are the first indication that the device has photon-assisted transitions. Another composite transition that will be important is the following:

$$|g_0, 1_r\rangle \rightarrow |e_{-1}, 0_r\rangle \tag{3.28}$$

This is the transition that causes the vertical bands in figure 6.7a, and is a particularly interesting composite transition because it involves a combination of a fluxon, plasmon, and photon.

Composite Avoided Crossings

In addition to the presence of composite transitions, we also see composite avoided crossings (particularly when the qubit is in a persistent negative temperature state). An example of this is when the following two transitions come into resonance with each other:

$$|g_0, 0_r\rangle \rightarrow |e_0, 0_r\rangle \tag{3.29}$$

$$|g_0, 0_r\rangle \rightarrow |g_1, 1_r\rangle \tag{3.30}$$

This is an example of a higher order composite avoided crossing between $|e_0, 0_r\rangle$ and $|g_1, 1_r\rangle$, which can be seen in figure 7.4b.

3.2 Chain Design

3.2.1 Superinductance: JJ Chains

Generally speaking a Josephson junction is a non-linear inductive element, and its non-linearity can be engineered dependent on the size of the junction. The smaller the junction, the more it will constrict the flow of current, and consequently the more non-linear it will behave. This non-linearity is essential in the realization of qubits like the transmon qubit, where it is this non-linearity that allows the specific quantum states to be coherently controlled. However, in the case of the fluxonium qubit we will also wish to engineer the junctions to be well approximated by the first term of the Taylor series. The inductance of our chain at low temperatures is given by:

$$L_{\text{chain}} = N\frac{RA\hbar}{\pi\Delta A} \tag{3.31}$$

where N is the number of junctions, Δ is the bandgap of the metal being used, RA is the resistance area product of the junction and A is the area. We put it in this form, because the RA product should be a constant for a given oxidation pressure and time, and so this value this is a function of the junction area. In this way, we can make the junctions small to increase their inductance, but that will also increase the non-linearity of the junction. It is the interplay between these two that can be engineered to maximize the inductance that can be realized by the chain. The other option to increase the inductance is to make the chain longer and increase N. However, as we seek to increase the inductance of our chain by making it longer, we will begin to bring down the resonant mode of the chain and ruin its ideal inductive behavior.

Phase Slips

A proxy for determining the non-linearity of the larger junctions is to approximate what the phase slip rate of the junction will be. We approximate the phase slip rate of the chain to scale linearly with the number of junctions which gives [29]:

$$\Gamma = \frac{4N}{\sqrt{\pi}} \left(E_J^3 E_C \right)^{\frac{1}{4}} \exp^{-8\sqrt{\frac{E_J}{E_C}}}, \tag{3.32}$$

where N is the number of junction and E_J and E_C are the Josephson and capacitive energy of each individual Josephson junction respectively. To ensure a mostly linear inductive element, you simply make the junction area large enough to ensure the phase slip rate is small. However, one must take special precaution to avoid making the junctions have an inductance that is comparable to the geometric inductance. In these cases, inductive tuning will begin to show hysteric behavior, which is not usually desirable in superconducting qubits. However, this is only a proxy for the junction's non-linearity. A more direct measure is to look at its self-Kerr mode. Physically, this is defined as the shift of the resonator mode as a function of the number of photons being placed inside the mode [44], where cross-Kerr modes are associated with the shift in a resonance when photons are present in another mode [45]. These cross-Kerr modes can be used as a way to engineer bistability in a Josephson junction array [46].

3.2.2 Chain Modes

Engineering them away

In the initial versions of the fluxonium qubit [11, 14, 15], the chain of large Josephson junctions was made short enough to ensure that it could be well approximated by as a lumped element inductor. However, as one wishes to further increase the inductance of the qubit

(useful for improving the T_2 of the device), these modes will inherently be pushed to lower frequencies and will eventually need to be accounted for. In the chapter 4.1.5, we present a possible 'stacked junction' fabrication method that can be employed as a way to achieve inductance above 1μH without need of accounting for the chain modes. However, in the case that we wish to make the inductance larger by simply making the chain longer, the chain modes must be considered. At this point in time, it is unclear if these simple approaches to increasing the qubit inductance will be successful. A recent experiment demonstrated the ability to realize a heavy fluxonium with an even longer chain [30], but the T_1 of the device is about the same as that of transmon qubits. This may, however, be due to material properties, as [30] did not make use of the Josephson junction array. Nonetheless, these chain modes can serve as an interesting platform for engineering light/matter interactions.

Intentionally Engineering them

An exhaustive treatment to this end is discussed in [21], where an approximate Langrangian for a chain of junctions is modeled. To be able to understand the effect of these modes, we model the chain as a series of junctions with an individual Josephson inductance L_{jA_i}, and charging energy dependent on C_{jA_i}, and with some stray capacitance to ground C_{g_i}, as shown in figure 3.8. In the case of this exhaustive fluxonium model we have that the kinetic and potential energy is given by [21]:

$$T = \frac{1}{16E_C^{\phi}}\dot{\phi}^2 + \frac{1}{16E_C^{a}}\sum_{\mu}\dot{\xi}_{\mu}^2 + T_G$$

$$V = -E_J^b\cos(\phi + \phi_{ext}) - E_J^a\sum_m \cos\left[\frac{\phi}{N} + \sum_{\mu} W_{\mu m}\xi_{\mu}\right]$$

where ξ_μ is the collective modes of the chain, T_G is the modification of the kinetic energy when accounting for coupling and stray ground capacitance. When the large junction array

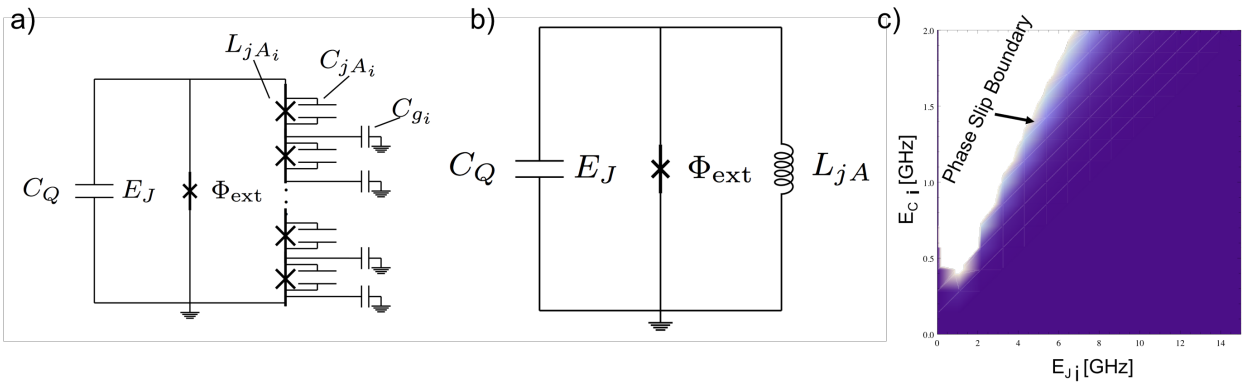

Figure 3.8: a) The inductive chain of the fluxonium consists of a series of large Josephson junctions, each with some small stray capacitance to ground. In the case of the main result presented in this thesis we ensure the chain length is short enough not to worry about the modes of the chain junctions. b) The idealized circuit model. c) A plot of the phase-slip boundary for an individual large junction where E_{J_i} and E_{C_i} are the Josephson energy and charging energy of a single large Josephson junction, L_{jA_i} and C_{jA_i}, respectively, labeled in subfigure a. This boundary is determined to be roughly 1mHz for the entire chain of junctions to ensure that the chain behavior does not significantly influence the measurement of the device (T_1 measurements can take about 30 minutes per flux point, without reset protocols).

is designed properly, we make sure to satisfy the condition $E_J^a/E_C^a \gg 1$, and the chain modes should be slowly varying and we have $\dot{\xi}_\mu \approx 0$. In this approximation, we are left with the following form for T_G:

$$T_G = \frac{1}{16}\left[1 - \frac{1}{4E_t}\left(\frac{2}{3}\frac{N+1}{N}\lambda\right)\dot{\phi}^2\right]$$

where N is the number of large junctions, $E_t = e^2/2C_T$ and $C_T = 2(C_g^b + C_c) + (N-1)C_g^a$. So, under the approximation that the chain modes can be considered slowly varying, stray capacitance to ground will simply result in a modification to the charging energy of the fluxonium qubit. Of course, this approximation will break down if enough junctions are added to the chain, complicating the nature of the Hamiltonian. If, however, one must account for these modes, then it should only be the even modes of the chain that couple to the qubit (as these are the modes that will actually place a voltage across the small Josephson junction). However, while these chain modes may complicate the nature of the device, they do not prohibit the possible realization of such a qubit as demonstrated in the realization of a heavy fluxonium with a kinetic inductance inductor realized by niobium titanium nitride [30]. Studies on bi-stability in Josephson junction chains [46] may help elucidate the effects of non-linear self/cross-Kerr chain modes on a fluxonium qubit.

3.2.3 Superinductance: Kinetic Inductance

One can instead use kinetic inductance of a wire to realize large inductance values. Generally speaking this kinetic inductance is the result of a reduced density of cooper pairs in the superconductor which requires that the velocity of a given cooper pair be larger for a given current. The kinetic inductance of such a wire is given by:

$$L_k = \left(\frac{m}{2e^2 n_s}\right)\left(\frac{l}{wd}\right) \tag{3.33}$$

Where m is the mass of the charge carrier, n_s is the density of cooper pairs and l,w,d are the length, width and thickness of the wire. The strength of the kinetic inductance is given by the kinetic inductance fraction:

$$\alpha_{l_k} = \frac{L_k}{L_{\text{total}}} \tag{3.34}$$

And an increase in the kinetic inductance fraction is generally associated with a larger sensitivity to the breaking of cooper pairs. This increase sensitivity makes kinetic inductor ideal detectors, and is deemed a Kinetic Inductance Detectors (KIDs), commonly used in astronomy experiments. In the case of quantum information, we would ideally shield ourselves from any source of quasi-particle generation, as this would ultimately reduce the coherence times of our qubits. As such, KIDs can serve as an ideal means to measure the 'cleanliness' of your microwave environment. Several different materials have been realized with large kinetic inductance fractions, including Titanium Nitride [30, 36], Indium Oxide [20] or even 'granular Aluminum' [37] which is just aluminum that is deposited with an intentional partial pressure of oxygen. In the case of TiN or InOx, there is an associated phase slip rate of the meandering inductor given by [20]:

$$\gamma_{QPS} \approx \frac{\Delta}{\hbar}\frac{R_Q}{R_\xi}\frac{L}{\xi}\exp\left[-A\frac{R_Q}{R_\xi}\right] \tag{3.35}$$

Note that the phase slip rate is only linear on the length of the wire, but is exponentially sensitive to the resistance. Accounting for this, we can engineer a highly inductive wire, with minimal phase slips, by making the wire very long which can be useful for the realization of a large kinetic inductance in a fluxonium circuit. This, however, will require that we consider the chain modes of the inductor, which currently has unknown implications.

3.3 Gate Methods

As stated earlier the plan of attack is to improve the qubit lifetime by simply decreasing the coupling of the states. If the dipole matrix element is small to start, then it will be difficult for it to decay. However, the same mechanism that suppresses undesired decays in this case will also suppress the desired coherent oscillations between our two states, increasing the required time to perform gates on our qubit. This fact alone would indicate that this method of improving the lifetime would not really result in a useful improvement for quantum computing, as it ultimately comes down to the ability to perform many gates in the coherence time of the device. However, the rich energy structure of the fluxonium provides the possibility to suppress the coupling of our low-lying energy states, while using higher energy states (which couple to both states due to have a decent wavefunction amplitude in both wells) to coherently couple our states of interest.

3.3.1 Direct Drive

Even though we intentionally suppress the coupling of the low-lying states $|g_0\rangle$ and $|g_1\rangle$, we can still attempt to drive oscillations between these states. Generally speaking, this can be described by the Rabi oscillation rate which, for a drive tone E_0, detuned by Δ from the transition of interest, is described by:

$$\Omega_{i,j} = \sqrt{|\chi_{j,k}|^2 + \Delta^2} \tag{3.36}$$

where the resonate rabi rate is given by:

$$\chi_{i,j} = \frac{d_{ij} \cdot E_0}{\hbar} \tag{3.37}$$

d_{ij} is the dipole matrix element between state i and j, E_0 is the strength of the associate field. In the case of a direct drive of the heavy fluxonium we will have the dipole matrix element heavily suppressed and, consequently, the Rabi oscillation rate will be extremely slow. Consequently, we must use another level that has a strong dipole element to both $|g_0\rangle$ and $|g_1\rangle$ states.

3.3.2 Raman Transition

The benefit to the fluxonium circuit is that it breaks the degeneracy of the transmon cosine potential and consequently allow us to engineer the disjoint states, while also having higher energy states that can be used to couple the disjoint states. This allows for us to implement techniques commonly found in atomic physics, such as Raman transitions [38, 39] or coherent population trapping [42, 43]. These gate methods allow one to study various physics effects, such as electromagnetically induced transparency [41] or Autler Townes splitting [30] (These two affects are similar, but not the same [40]). Since the direct drives are strongly suppressed, we must make use of the higher energy manifold $|f_0\rangle$ as a way to couple our states coherently. To do this, we will need two drive tones, instead of the one used when directly driving the transition. One tone will drive the 2-photon plasmon $|g_0\rangle \rightarrow |f_0\rangle$ transition, which is mediated by the $|e_0\rangle$ state and the other tone will drive the fluxon $|f_0\rangle \rightarrow |g_1\rangle$ transition. The rate of this coupling is then modified by the coupling of our two drive tones and is given by:

$$\Omega_{g_0 g_1} = \frac{\Omega_{pump}^2 \Omega_{probe}}{\delta_{2\gamma} \Delta} \tag{3.38}$$

Where $\delta_{2\gamma} = E_{e_0} - \nu_{\text{pump}}$ is the detuning of our 2-photon drive from the primary plasmon and $\Delta = 2\nu_{\text{pump}} - E_{f_0} = \nu_{\text{probe}} - (E_{f_0} - E_{g_1})$ is the detuning of the pump and probe tones from the two-photon resonance. I would like to note, that while we used the $|f_0\rangle$ state as our auxiliary coupling state, in principle one could use the primary plasmon $|e_0\rangle$ instead. In the case of this thesis, we did not use this due to the highly Purcell limited lifetime of

the transition from being in close proximity to our readout resonator. Practically what will limit our gates is the presence of other modes, which will be driven off-resonantly when we turn up the drive powers. This will result in reduced gate fidelities, as will begin to occupy modes that are not our desired $|g_1\rangle$ mode.

3.3.3 Plasmon Pumping

Optical pumping, originally discovered by Alfred Kastler (Nobel 1966), is a method that can be used to prepare a cloud of atoms into their excited states by means of a non-radiative decay. Commonly used in atomic physics [22], or in NV-centres [23, 24], this gate method is made possible when there are two metastable disjoint states ($|g_0\rangle$ and $|g_1\rangle$ in figure 3.9b) are coupled via a lossy higher energy state ($|e_0\rangle$ in figure 3.9b). This method can be used for the purpose of preparing our device in the excited state by constantly driving on the $|g_0\rangle \rightarrow |e_0\rangle$ transition and then measuring the T_1 of the device. Furthermore, this principle can instead be used as a means to 'reset' the qubit the ground state $|g_0\rangle$ by instead driving on the $|g_1\rangle \rightarrow |e_1\rangle$ transition, which will eventually pump the device into the ground state.

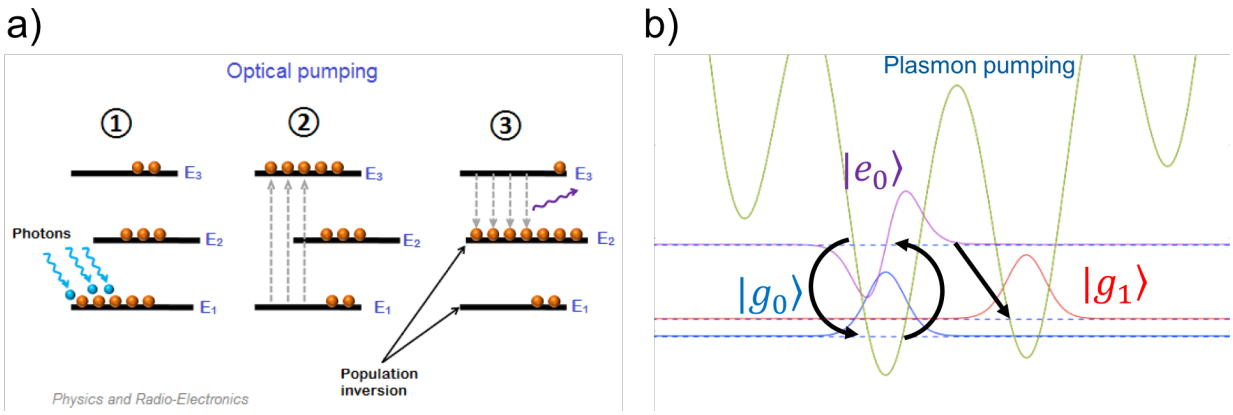

Figure 3.9: a) A cartoon depiction of the optical pumping method developed by Alfred Kastler, whereby photons will excite an electron from the ground state (E_1) to an excited state of the system (E_3), which then decays to desired state to be occupied. b) A similar mechanism of the heavy fluxonium device, in which we can drive on the ground state plasmon-like transition ($|g_0\rangle \rightarrow |e_0\rangle$). Most of the time the device will simply decay back down to the ground state $|g_0\rangle$, but due to a finite coupling between $|e_0\rangle$ and $|g_1\rangle$ there is a chance for the device to decay into our excited state $|g_1\rangle$, inverting our device, and allowing us to do subsequent T_1 measurements.

CHAPTER 4

JOSEPHSON JUNCTION FABRICATION

4.1 Josephson Junctions: Lithography

A critical component to superconducting qubit technology is the Josephson junction (JJ). To date, this is the best non-linear element to use for in order to generate access to a two-level system. Broadly speaking a Josephson junction can come in many different flavors, consisting of different combinations of metals and insulators. For the purpose of this thesis I will focus on the Superconducting-Insulating-Superconducting (SIS) Josephson junction. Within this, I will focus on the use of Aluminum and Aluminum Oxide (Al-AlOx-Al) as the way to create a Josephson junction, but this not the only means of making a SIS Josephson junction.

There are many different ways in which one can create an Al-AlOx-Al junction, and each method has its strengths or weaknesses. Below I will discuss the three different method used in our lab to create Josephson junctions, and a new method of stacking Josephson junctions that has been explored as a way to create a 'Hyper-inductance'. Ultimately all fabrication methods for in-situ Josephson junction will require an evaporator with stage rotations and was the primary method used in the Schuster lab, using a plassys evaporator. However, some recent work by Wu et al [61] demonstrates the ability to create a Josephson junction in multiple fabrication steps, exposing the metal to atmosphere, and still achieve decent quality factor transmon qubits. This fact serves to support the possibility of creating stacked Josephson junctions with multiple layers, which we will discuss below.

4.1.1 Adhesion Issues: Silicon vs Sapphire and Vacuum Bake

Regardless of which method one uses to fabricate Josephson junctions, I have found a large barrier to getting successful fabrication is to ensure that there is good adhesion between the

resist and the substrate. Generally speaking, the Dolan bridge method seems to be the least susceptible to this issue, due to the fact that the top layer of resist (typically PMMA) defines the deposited features and is connected throughout the pattern. Since the PMMA does not adhere directly to the substrate is does not tend to move when adhesion is poor. However, a primary source of this adhesion issue appears to be due to residual water on the surface of the substrate, which can be baked away immediately before spinning the resist (just by putting the wafer on a hot plate above the boiling point of water). Personal experience has shown that this alone seems to work well for silicon, but does not always lead to good adhesion on sapphire. What I have further found is that baking under vacuum helps further improve adhesion on sapphire. I have since adopted the habit of baking all of my wafers under vacuum immediately before spinning the bottom layer of resist (generally MMA in junction fabrication).

4.1.2 Bridgeless Method

The bridgeless method, developed by Lecouq et al. [31], is a very good method to use for creating dense arrays of large Josephson junctions, once a few critical failure modes are addressed. This method also only uses two different planar angles, and to create the break in the layers is relying on an asymmetric patterning of undercut. The benefit to this method is that, under ideal conditions, arbitrarily large Josephson junctions can be realized. A diagram is shown in figure 4.1 demonstrating the necessary design realizations for a successful fabrication of large Josephson junctions using this method. (see figure 6.1) However, when using this method to fabricate Josephson junctions I ran into a few issues (see figure 4.2). For successful fabrication, the top layer of resist needs to be thick enough for the undercut (represented by UCW is figure 4.1b/c) to not sag, but ensuring the connecting fingers are actually deposited (i.e. $FW_2 > 0$,$FW_3 > 0$). To this end we get that the deposited

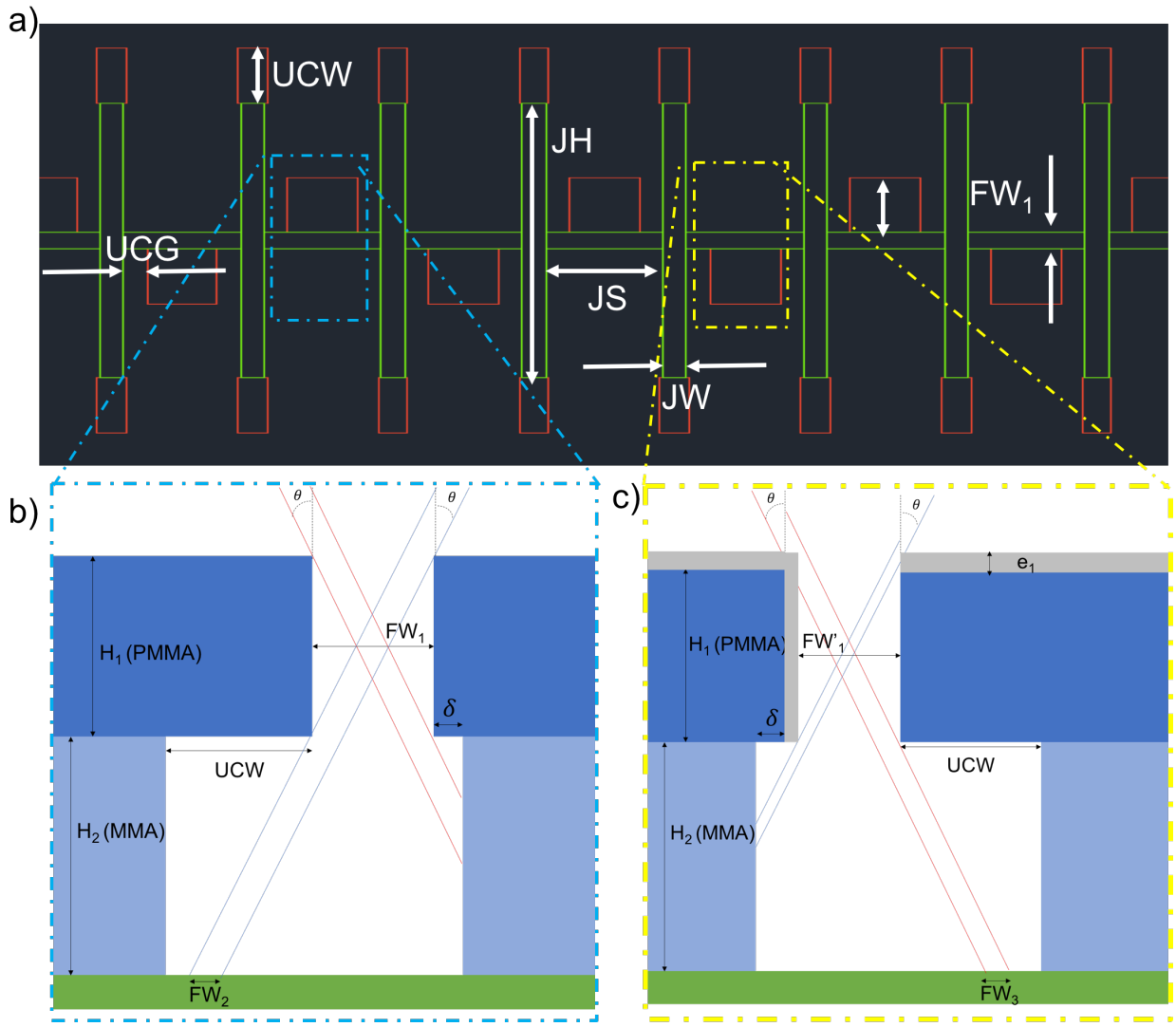

Figure 4.1: a) dxf pattern with all of the relevant dimensions for fabricating a chain of Josephson junctions using the bridgeless method. Failure modes tend to arise from: 1) the undercut gap (UCG) being too small 2) the junction separation (JS) being too small, or 3) the junction height (JH) being too large. Failure mode 1 causes a symmetric deposition of the fingers due to the natural undercut (δ in b) and c)) being too large. This natural undercut can be too large when the main dose (used to write through both MMA and PMMA) is too large as well. (Though, when the dose is optimized, this failure mode still arises if δ is too small.) Failure modes 2 and 3 generally result in structure movement of the resist. This can be mitigated through lowering H_2 and doing a vacuum oven bake. b) and c) Show the side perspective of the resist structure, in particular highlighting that the designed finger width (FW_1) is generally larger than deposited finger widths, FW_2 and FW_3. FW_3 will generally be smaller than FW_2 due to the deposited metal further reducing the open gap for finger deposition.

finger widths are:

$$FW_2 = FW_1 - H_1 \tan\theta \tag{4.1}$$

$$FW_3 = FW_1 - H_2 \tan\theta - (1 + \tan\theta)e_1 \tag{4.2}$$

Note how the second deposited finger width (FW_3) depends on the amount of metal deposited (e_1). In order for this bridgeless method to work appropriately the designed finger width (FW_1) cannot be too large, otherwise the asymmetric deposition will never occur. However, if the finger is too thin you risk not depositing the fingers. When optimized, the finger width will generally be comparable to the amount of metal being deposited and so it can happen that the first finger (FW_2) is deposited but not the second finger because FW_3 becomes negative. When imaging the junctions, this can give the false impression one needs increase the dose which will then lead into different failure modes, which are further discussed below.

Bridgeless Failure Modes

Over the course of a few years, I ran into the challenge of getting consistent results with my fabrication of Josephson junction chains when using the bridgeless method. The primary challenge was ensuring the resist structure would not move during development (see figure 4.2 a-c). To overcome this issue, several different approaches were used, but ultimately it was found that structure movement would be mitigated by be ensuring good adhesion between the bottom resist layer (MMA in the case of my devices) and the substrate being used. This adhesion issue appeared to be the result of residual water left on the surface of the wafer. In order to fully remove this it has been found that baking above the boiling point, UNDER A VACUUM, and this resulted in far more consistent fabrication results, making it easier to debug different failure modes. Generally speaking it was also found that the adhesion was better when using silicon substrates instead of sapphire. Structure movement would also be

the result of a combination of the junctions being too closely spaced (UGC is figure 4.1a) and the bottom resist (H_2 in figure 4.1b/c) layer being thick. This created an unstable structure that was overly sensitive to dose and the natural undercut. By increasing the spacing between junctions, you can obtain a more stable structure, but this comes at the cost of a reduced inductance, and longer overhangs (which make the asymmetric deposition more difficult, though not impossible). The other common failure mode would be the symmetric deposition of the connecting figures (as seen in figure 4.2d). This failure mode would arise from either a non-optimized dose, and the undercut gap ('UCG' in figure 4.1) being too small. Even when the dose was optimized, if UCG was too small, the proximity dose would be large enough to make the natural undercut (δ in figure 4.1b/c) too large to achieve an asymmetric deposition of the connecting fingers. This failure mode results in the shorting of the junction.

4.1.3 Dolan Bridge for Junction Chains

The Dolan bridge method (see figure 4.3) is one of the original fabrication methods to create a Josephson junction in an in-situ evaporation, and was the initial method used for the first superinductors [15]. This method uses a single planetary angle, but two different normal angles. This fabrication method is generally a robust fabrication method and can be used for Josephson junctions of varying sizes, but becomes slightly more complicated as you wish to make the junctions larger, useful for the realization of superinductances as shown in figure 4.3. When making a chain of junction in this method one must take care to avoid the collapse of the bridge for the larger junctions, caused by increasing the junction height (JH in figure 4.3b inset). To this end the important parameters to pay attention to are the bridge thickness (H_1 is figure 4.3c, which is usually made of PMMA resist. The second parameter one must pay attention to is the width of the bridge, W_1 in figure 4.3c. Fabrication tests show that a junction of height JH $\approx 5\mu$m and a width $JH_{1,2}$ $\approx$200nm can be successfully made with a bridge height of H_1 $\approx$700nm and width of W_1 $\approx$200nm (when developed in IPA:H_2O (3:1)

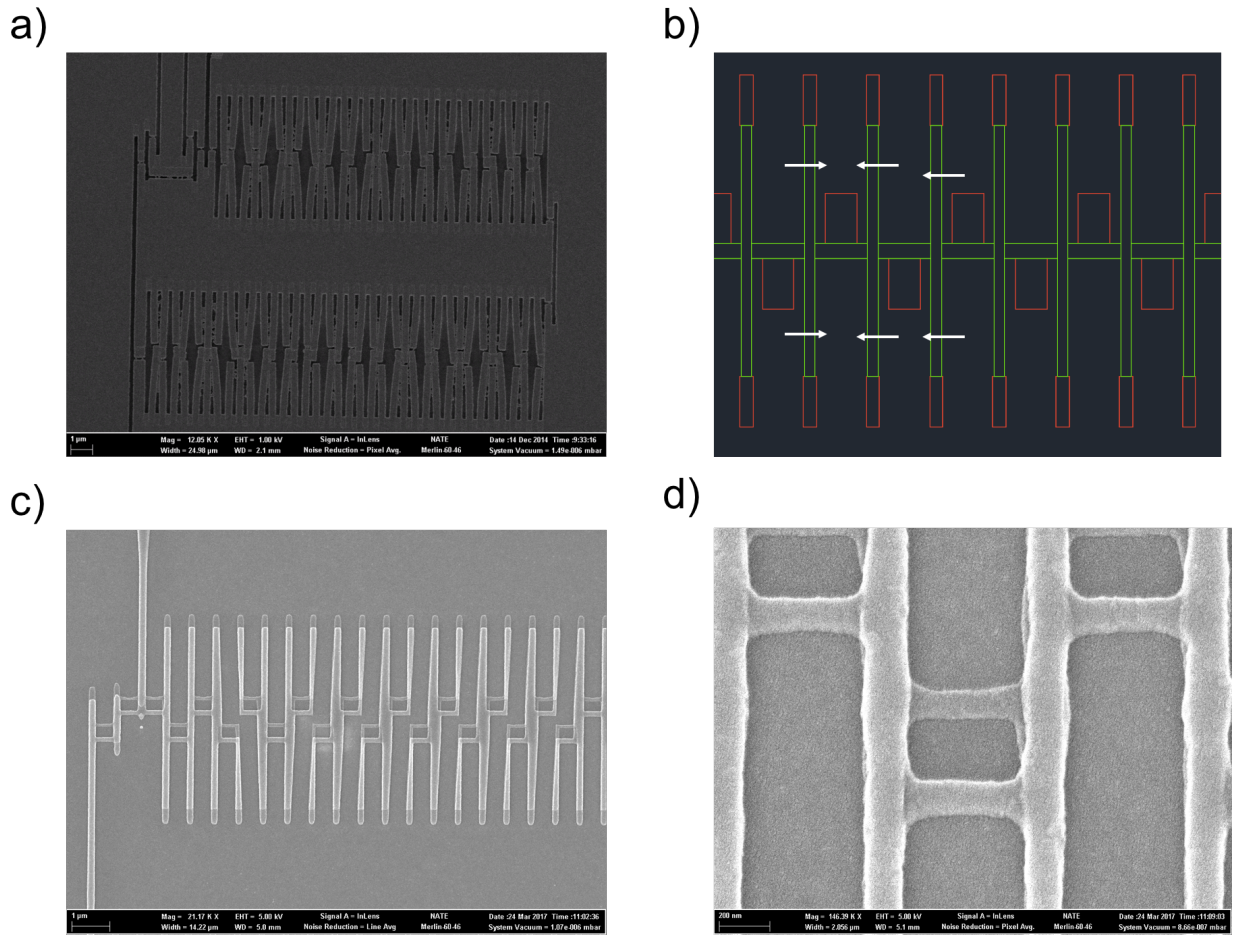

Figure 4.2: a-d are Examples of failure modes for the bridgeless fabrication method. e is a successful demonstration of a long chain for initial tests of the next generation fluxonium. a) An SEM image of the MMA/PMMA resist demonstrating structure movement. In particular, note that the structure movement is not a result of overdosing, as the PMMA resist is not entirely written through, and yet movement occurs. b) The pattern file for writing the bridgeless chains with arrows indicating the direction of the structure movement. c) An example of what the resulting evaporation looks like post lift-off when there is structure movement. d) The failure mode of the natural undercut δ (seen in figure 4.1 b and c) being too large. This generally happens because either the relative dose between the main dose and undercut dose has not been optimized or because the undercut gap (UCG in figure 4.1a) is too small.

at 6C for 1min 30seconds). A thinner bridge width W_1, though helpful for compact junction chains, fails for junctions with JH$\approx 5\mu$m. The resulting junction areas are given by:

$$JA_1 = \tan\theta(2H_1 + 2H_2 + e_1) - W_2 \tag{4.3}$$

$$JA_2 = 2H_2 \tan\theta - W_1 \tag{4.4}$$

where e_1 is the thickness of the first evaporated layer (not pictured in the diagram), and it is required that $W_2 < \tan(2H_1 + 2H_2 + e_1)$ and $W_1 < 2H_2 \tan\theta$, in order to have a continuously connected chain of junctions. When trying to make a large inductance, it is desirable to make this chain as compact as possible to get the most inductance per unit length. However, to reduce the junction separations (JS_1, JS_2) one must reduce the total resist height, $H_1 + H_2$, and the bridge width, W_1. Reduction of either W_1 or H_1 risks the collapse of the bridge and one must take special care to balance the tradeoff between getting more compact junctions and actually getting a successful fabrication.

4.1.4 Manhattan

The Manhattan method is another option one can use when engineering Josephson junctions. This method, is completed by fixing a single planar angle and using two different planetary angles (represented by the red and blue arrows in figure 4.4. Inspired by the geometry, it is called Manhattan as it uses thick layers of resist as a way to ensure that metal is only deposited along one 'street' or another (the green boxes in figure 4.4a) as the way to create a Josephson junction. The original implementation of this method is made such that the fingers of the junction are deposited during the evaporation and is ideally used for smaller junctions. The typical fabrication failure mode of this method usually comes from the two layers being shorted out by stubs from each evaporation, as seen in figure 4.4b. To overcome this error, one must simply ensure good adhesion with the resist and a sufficiently large planner angle

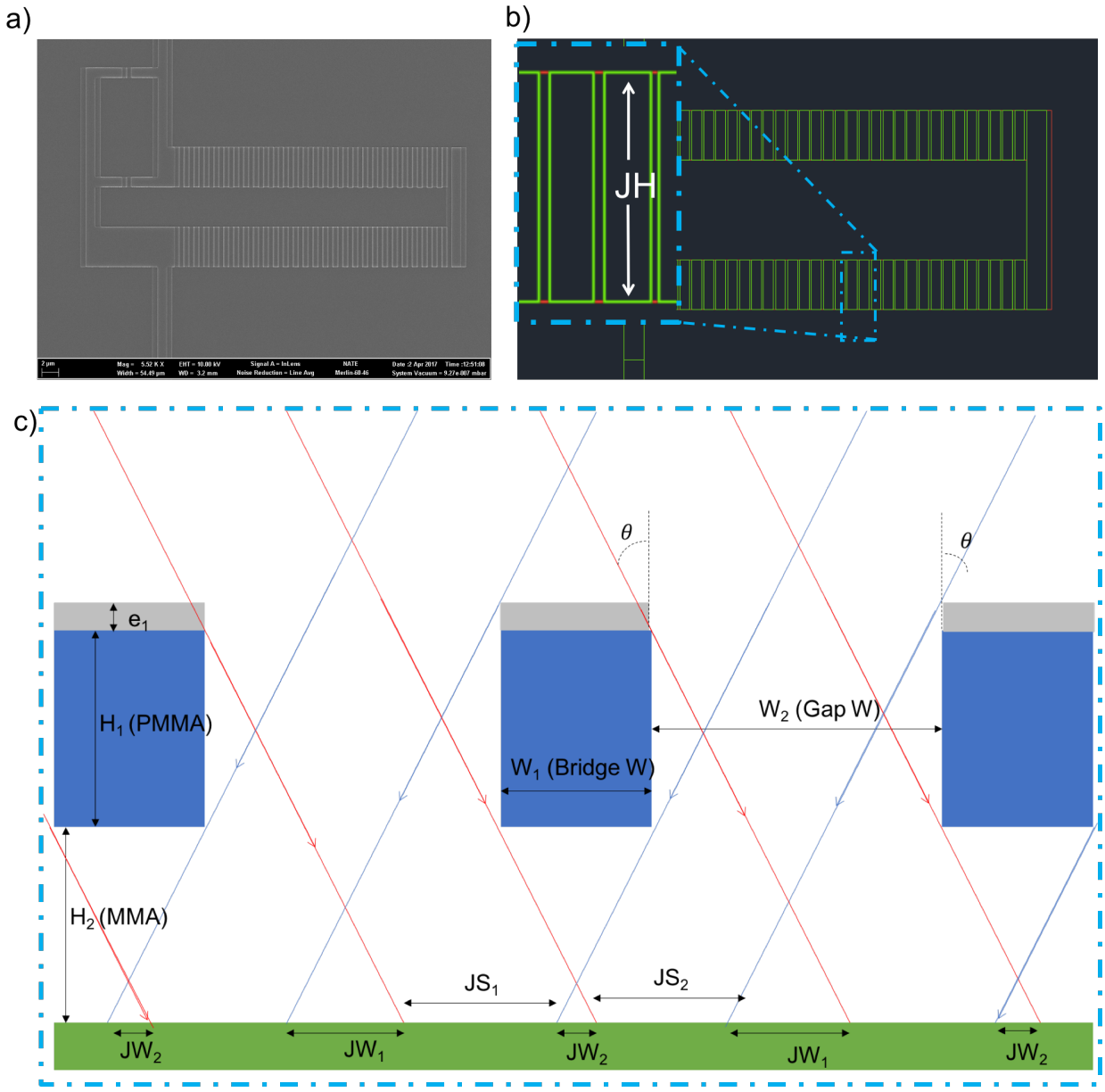

Figure 4.3: a) An SEM image of a fluxonium circuit with a tunable E_j as well as the regular ϕ loop. b) The corresponding pattern given to the ebeam writer, with the dashed light-blue box corresponding to diagram shown in c. c) The side perspective of the Dolan bridge, demonstrating that there are two junction areas and separations. There is ultimately a trade-off between a getting a compact chain of Josephson junctions and the collapse of the bridge when dealing with larger junctions.

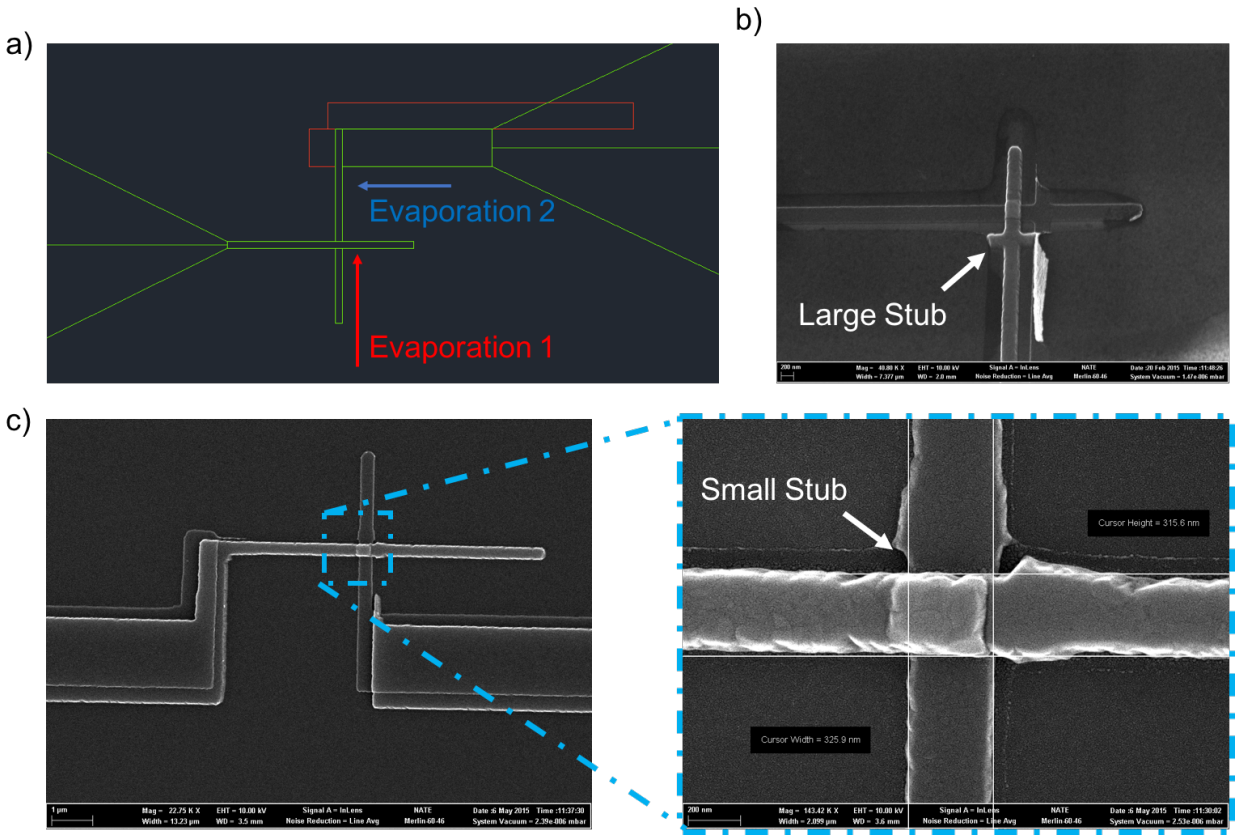

Figure 4.4: a) A dxf pattern file. The red and blue arrows represent the two different planetary angle evaporations. In the dxf, the green boxes represent the sections in which a large dose will be presented to write away both the mma and pmma whereas the red boxes represent the areas in which a lower dose will be presented to only remove the copolymer mma. b) An example of the failure mode of the Manhattan method for small junctions. The stubs are the result of shallow planar angle of evaporation or from having too large of a natural undercut.

or resist thickness. Using these method is ideally suited for making smaller junctions, but one can use a combination of the rotating the planetary angle with the bridgeless method of create an asymmetric undercut as a way to only deposit connecting fingers for a larger Josephson junction. To see such a pattern, look at [32] where he uses the Manhattan method as a way to make large junctions for a tunable coupler.

4.1.5 Stacked Junctions: Manhattan 2.0

A large goal with the heavy fluxonium qubit was to push the upper limit of coherence that a superconducting qubit can achieve. To this end, there are the two values by which you judge the quality of a qubit: T_1 and T_2. The primary result of this thesis was achieving a large T_1, but this alone is not enough for the qubit to be useful for quantum information, you also need a large T_2. However, the good news was that the T_2 was limited by external flux noise, which then means that the coherence can be improve by either reducing the noise or reducing the qubits sensitivity to flux noise. The second approach is achieved by making the flux slope of the transition of interest shallower, which can be achieved by further reducing the inductive energy of the circuit. Or, in other words, increasing the inductance beyond the 'superinductance' achieved by the fluxonium circuit and pushing it into a 'hyperinductance' regime and generating yet another new class of flux qubits, deemed the 'Blochonium' [65]. Motivated by the qualitative change that was achieved in the original charge qubits by adding a very large capacitance as a way to mitigate sensitivity to charge noise, the 'blochonium' is a name to highlight the qualitative difference by further increasing the fluxonium qubit, and the possibility of the device to create a fully self-consistent current standard [51, 52]. While it may be possible to achieve these hyperinductance values by simply making the chain of Josephson junction longer, this path will require a careful consideration on the effects of stray capacitance and the resultant chain modes (though it is unclear at this time how or if these modes will affect the performance of the device.) Another option, however, is to build upwards and stack junctions on top of each other. This approach is not without its complications however, and below I lay out some of the initial attempts towards this front.

Manhattan 2.0: Mixing the bridgless and manhattan methods

In order to fabricate a stack of large Josephson junctions in-situ with a single small junction, there must be a way to deposit a single layer of a small Josephson junction without

depositing metal in the area of the large junctions and to then deposit several layers of the larger junctions without then shorting the small junction by depositing metal in this area. In principle, one can just break these steps into two different fabrication layers and do one at a time, but this requires that the metal be exposed to atmosphere and that the junctions survive going on a hotplate and being in the SEM for the second layer of fabrication. While, in principle, this should be possible, we instead pursued a path in which both layers can be deposited at the same time by taking advantage of the wall deposition technique used in the bridgeless method, with the planetary rotation used in the Manhattan method. Furthermore, this approach allows us to use different oxidation parameters for the small junction compared to the large junctions, which may prove to be useful when implementing these techniques in the fabrication of the 0-π circuit. Within this approach there are generally two primary approaches one can take: a fully in-situ evaporation in which all connecting layers are deposited at once (see figure 4.5) or an approach where a non-junction base layer is used to connect different stack (see figure 4.6)

In-situ Evaporation

Usually it is desirable to not break vacuum in a way that will result in dirty oxide being near a Josephson junction. With this in mind an initial attempt at making a stack of large Josephson junctions was done in such a way to avoid venting the chamber in between junction evaporations, and is shown in figure 4.5. This involves using the undercut as a way to connect different junction stacks. While this has the benefit of being completely in-situ, it comes at the cost of junction density.

With initial base present

Recent results from [33] demonstrate the possibility of fabricating a Josephson junction in multiple layers with atmospheric pressured presented in between, and still getting fairly large

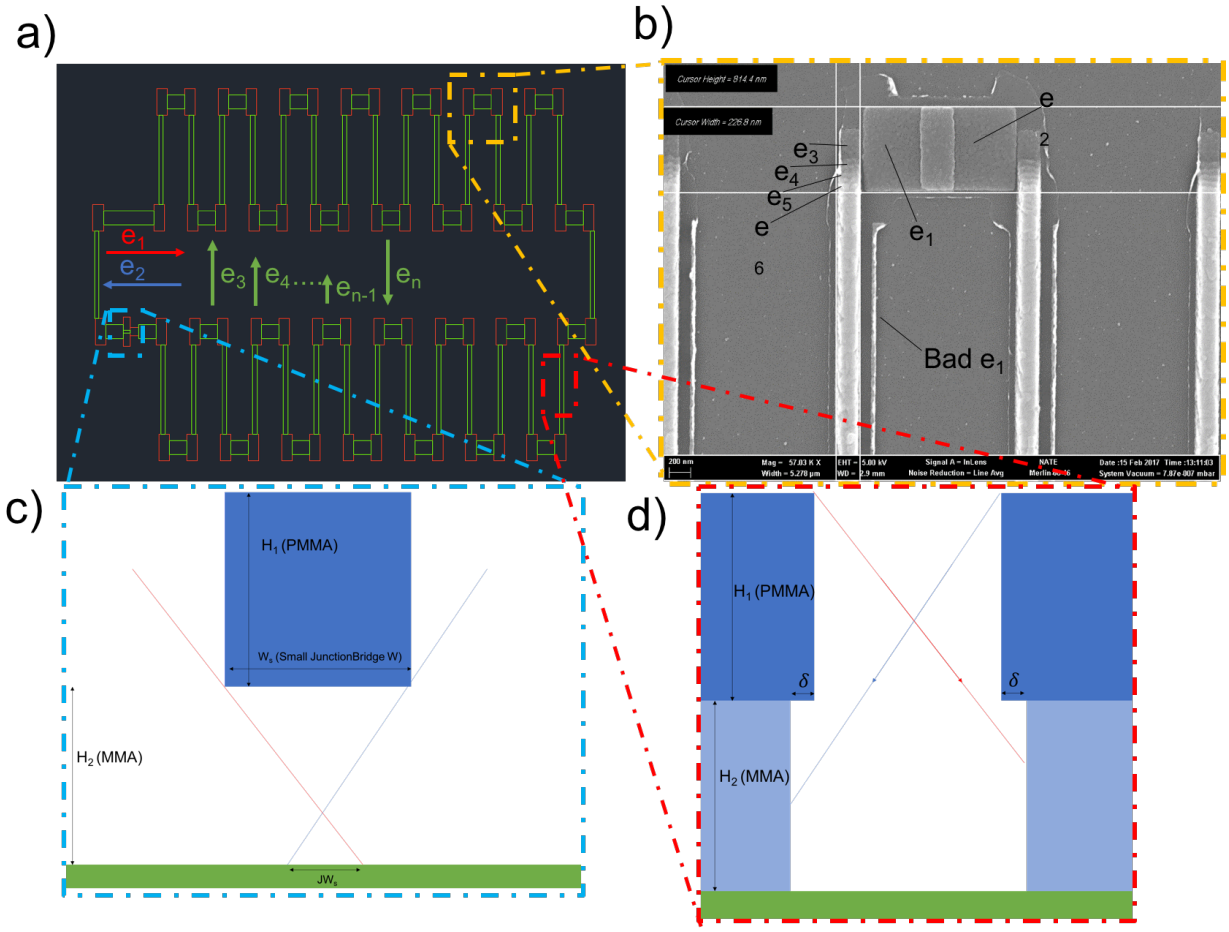

Figure 4.5: a) A dxf pattern of a prototype in-situ stack junction fabrication. The red and blue arrows indicate the first evaporation angles and the green arrows represent the evaporation angle of the large junction stacks. b) An SEM image of the dxf pattern shown in a with the various layers labeled. In particular note the 'Bad e_1' which represents an undesired deposition of the first evaporation layer due to either the natural undercut δ being too large or the evaporation angle not being large enough. c) A side perspective of the small junction area in the dxf pattern in a). d) A side perspective of the large junction area demonstrating the working principle of the stacked junction method in which an intentional wall deposition occurs due to a combination of a thick resist stackup (large $H_1 + H_2$) and a large evaporation angle.

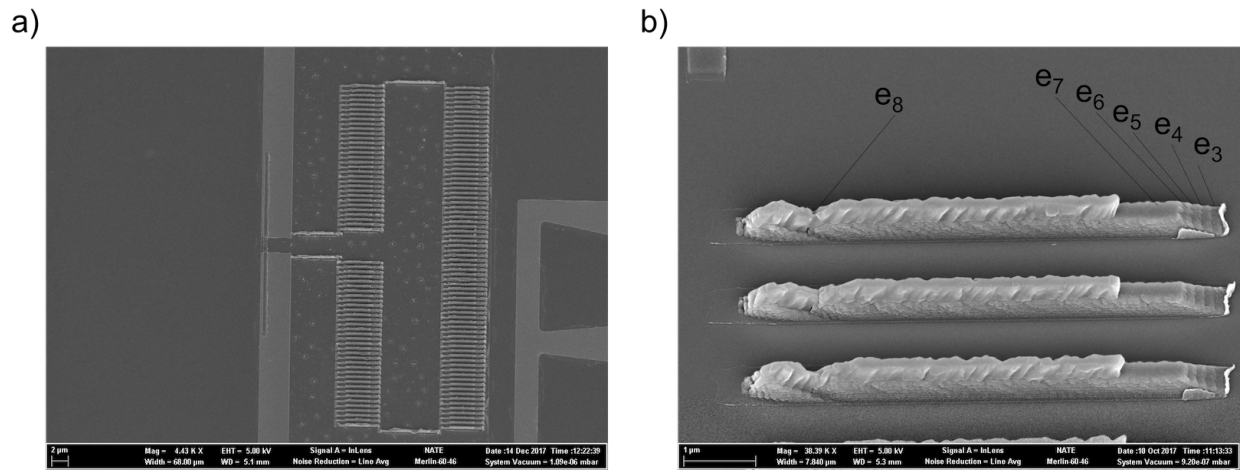

Figure 4.6: An example of the stacked junction procedure with a non-junction base layer present to connect the different stacks of Josephson junction. b) A zoom in on the stack of junctions, where it is possible to resolve each individual layer and demonstrates the importance of the final layer being thicker than the preceding deposited layers.

coherence times (about 35μs in the case of the mentioned study). In this case, it should be possible to fabricate a stack of Josephson junction with an initial non-junction layer base present (as shown in figure 4.5 and 4.7). Here an initial Niobium base layer is deposited as a means to connect stacks, with the steps outlines in figure 4.7.

The Manhattan method can be combined with the bridgeless method as a way to further extend the density of superinductance and to even possibly realize a 'hyperinductance', which is loosely defined as inductance values in excess of several micro-Henries.

4.2 Josephson Junction: Oxidation

A critical aspect to the engineering of a fluxonium atom is the superinductance created by either the chains of Josephson junctions or with a kinetic inductance. In either case, getting as much inductance per unit length will prove to be useful in engineering highly inductive chains without need to account for the chain modes (though it is currently unclear how much these modes will affect device performance). In the case of the Josephson junctions, this inductance per unit length is exponentially on the oxide thickness of the large junctions.

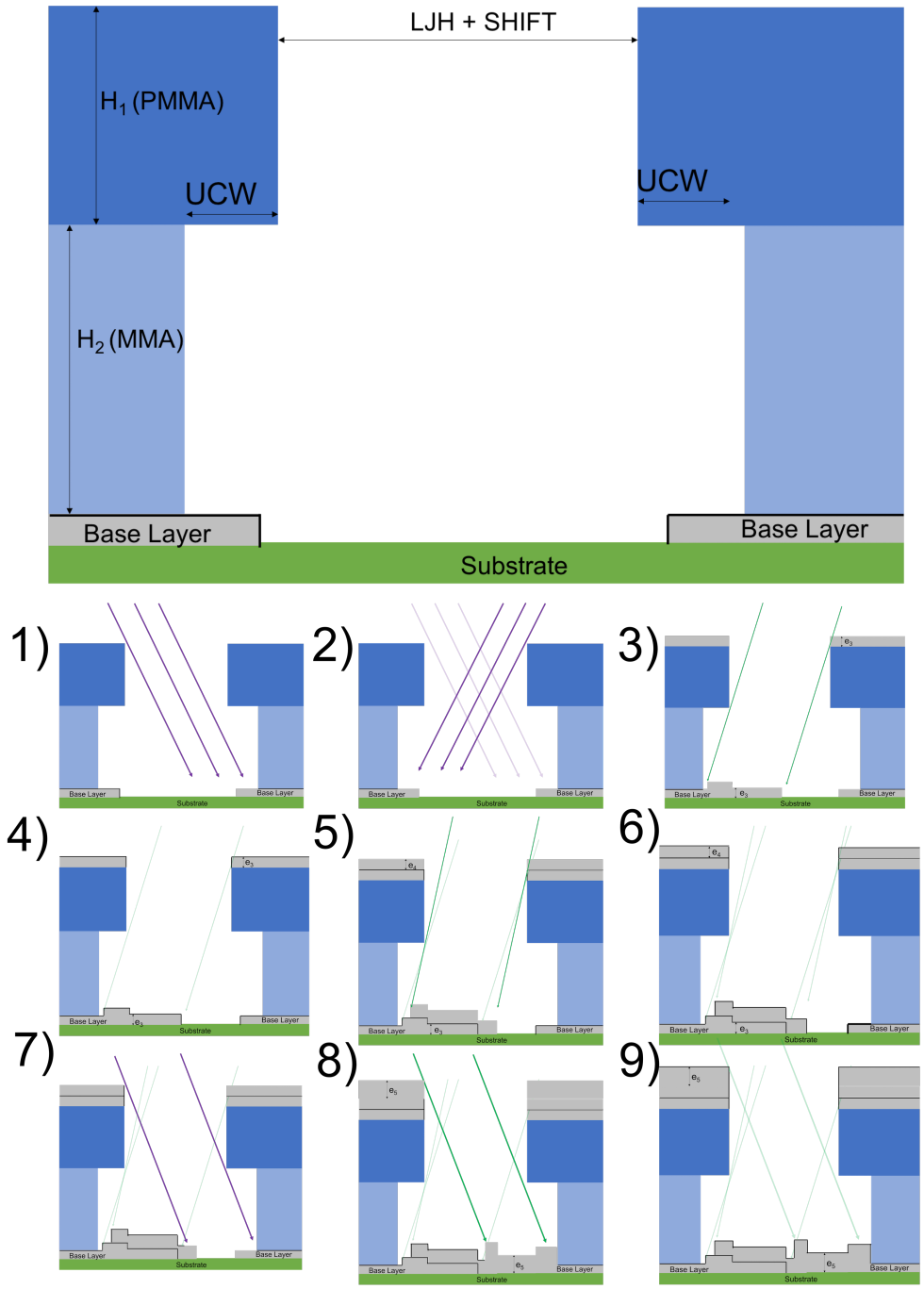

Figure 4.7: Diagram of the process used to realize a stack of large Josephson junctions. This, in combinations with a rotation method similar to a Manhattan method should allow for the realization of a stacked chain of Josephson junction as well as a single small junction without the need to vent to atmosphere in between

As we make the oxide thicker, the phase slip rate will increase as well, but only linearly. As such, it is useful to oxidize the junctions, creating a large RA product, and to scale up the area of the junction accordingly. To this end, my device used oxidation parameters that were not in line with what the rest of the lab generally uses for our transmon qubits. This diversion from the lab standard led me down a road with a few bumps, in particular getting consistent RA product at higher pressures.

Oxidation Time/Pressure

There are two parameters which can be tuned to adjust the thickness of the Aluminum oxide: the time and pressure of oxidation. According to a paper written by Zheng et al. [34], between these two parameters, the shifts in time are more sensitive than shifts in pressure. I unfortunately did not have time to reproduce these results for confirmation, but provide this as a guide for whoever wishes to do so. The RA product for the published heavy fluxonium was $4.97{\cdot}10^{-9}[\Omega m^2]$, but I believe that one could play with this factor to gain a factor of 3 increase in inductance for a chain of similar length, while still maintaining a small phase slip rate of the chain.

CHAPTER 5

EXPERIMENTAL METHODS

5.0.1 Cleaning Wafers

Sapphire

- Prepare spin station
- Sonicate wafer in NMP for 3 minutes
- Sonicate wafer in Isopropyl Alcohol for 3 minutes
- Sonicate wafer in Acetone for 3 minutes
- Sonicate wafer in Isopropyl Alcohol for 3 minutes
- Rinse under running DI water for 3 minutes, taking special care to ensure water stream is run across the entire wafer
- Dry with N_2
- Bake wafer in vacuum oven at 110C to remove residual H_2O
- Quickly move to spin station and spin resist

I want to draw attention to the baking step. It is of particular importance that this baking step is done in a vacuum chamber to ensure good adhesion between MMA resist and sapphire. A substantial amount of time was spent throughout my graduate years trying to solve this problem, and simply baking on a hot plate at atmosphere pressure did not result in good adhesion to my sapphire substrates. This vacuum bake does not seem to be as critical to get good adhesion between MMA and silicon substrates, and silicon is generally an ideal substrate to develop recipes on (for Josephson junction fabrication at least) due to its lower cost, improved adhesion, and no need for a conductive layer on top.

Silicon Prep for ALD TiN

- Sonicate wafer in NMP for 3 minutes
- Sonicate wafer in Isopropyl Alcohol for 3 minutes
- Sonicate wafer in Acetone for 3 minutes
- Sonicate wafer in Isopropyl Alcohol for 3 minutes
- Rinse under running DI water for 3 minutes, taking special care to ensure water stream is run across the entire wafer
- Dry with N_2
- Place in piranha acid (sulfuric acid and hydrogen peroxide) etch for 3 minutes
- Cycle Rinse with H_2O
- Place in Buffered HF for 3 minutes
- Quickly (< 5 minutes) place wafer in ALD tool vacuum

The buffered HF serves the purpose of Hydrogen terminating the silicon substrate and has generally resulted in the highest quality factor resonators when made with Titanium Nitride [36]. This hydrogen termination depletes over times, and studies [35] indicate that this termination lasts for up to 20minutes, though I always ensured that there was less than 5 minutes in between the rinse of the HF dip and placing the wafer inside an ALD vacuum chamber.

5.0.2 Metal Deposition: Evaporation Recipes

- Pump Chamber to 1.0e-7 mbar

- Evaporate Titanium for 4 minutes (This helps further reduced the chamber pressure) at a rate of 0.2nm/s (typically achieved with a 55mA source current)
- Switch to desired metal crucible (Aluminum/Niobium)
- Turn on ebeam and slowly ramp to initial current (110mA Aluminum/150mA Niobium) over the course of 5 minutes
- Check Spot position
- Slowly ramp to appropriate second current (170mA for 1nm/s Aluminum / 190mA for 0.9nm/s Niobiumm) over the course of 2 minutes
- Rate control for desired evaporation rate (1.0nm/s for Aluminum and 0.9nm/s for Niobium)
- Evaporate desired thickness of metal

From this recipe, I would like to specifically note the slow ramp over the course of several minutes. We found that this is important when trying to get higher quality aluminum films, and - in particular - a uniform deposition rate. If ramp times were much faster the deposition rate would have significantly larger variations during the deposition. There was also a question of the importance of the selected evaporation rate. For all of my Aluminum junctions I evaporated at a rate of 1nm/s, as I wanted to minimize the 'dirtiness' of the Aluminum. However, others in our lab would evaporate Aluminum junctions at a rate of 0.1nm/s and achieved high quality factor qubits regardless. So, it is unclear how the interplay between grain properties and film 'dirtiness' ultimately affect the performance of our qubit junctions. However, it is interesting to note that one can intentionally add oxygen in the chamber during Aluminum evaporation as a way to create granular Aluminum that has a significant amount of kinetic inductance [37] and can be implemented into a fluxonium circuit without the need for making explicit Josephson junctions.

5.0.3 Metal Deposition: Atomic Layer Deposition Recipes

Titanium Nitride

Atomic Layer Deposition recipe for Titanium Nitride. We use Ultratech Simply ALD tool for this recipe (See figure 5.1 for a cartoon depiction of the process).

- Heaters (13,14,15) on at 270C
- Heaters (16,17,24) on at 150C
- Heater 25 on at 125C
- Stabilize 3600 seconds
- Start ALD cycle

  Purge with 20 sccm Argon

  Flow Precursor 1: 50 sccm of TDMAT (Tetrakis(dimethylamido)titanium)

  Wait 5 seconds

  Flow Argon purge for 4 seconds at 5 sccm

  Flow Precursor 1(TDMAT)/2(N_2) at 20sccm each for 5 seconds

  Turn plasma on at 300 Watts for 8.5 seconds

- Repeat Cycle as needed. 50 cycles is roughly 4nm of TiN.

5.0.4 Lithography Recipes

Optical lithography: Heidelberg (BEST TOOL EVER) or Optical Mask

For features larger than 1μm, we can use optical lithography as a way to pattern them. This is preferable to ebeam lithography because it is much faster and allows one to create pattern

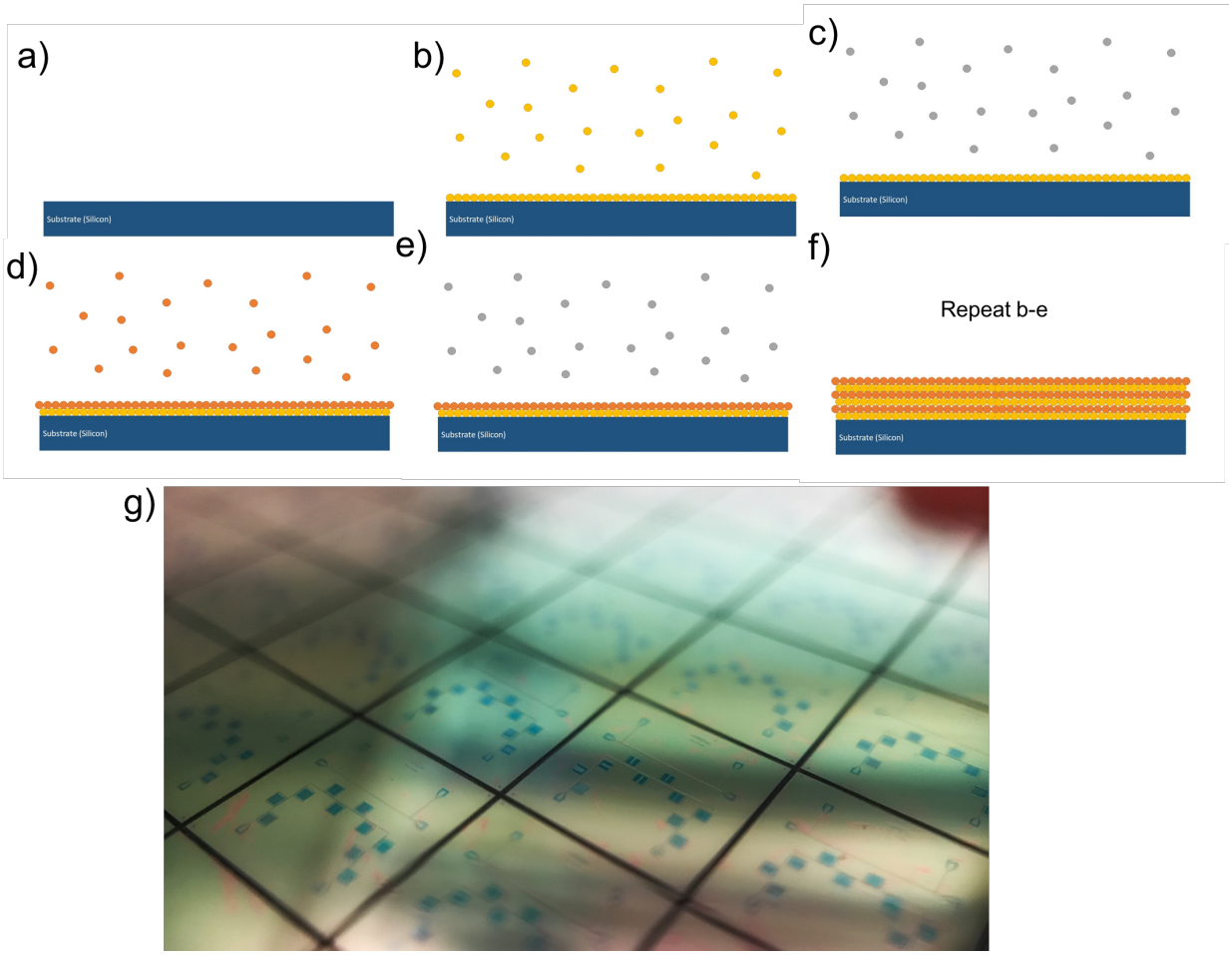

Figure 5.1: A cartoon depiction of the ALD process a) Start with a bare silicon <111> wafer (ideally hydrogen terminated) b) Flow your first precursor gas (TDMAT in our case) c) flow an Argon purge gas to clear out the chamber d) Flow your second precursor gas (a mix of N_2 and TDMAT) e) Flow an Argon purge gas to clear out the chamber f) Repeat steps b-e to achieve the desired thickness g) An image of a wafer of diced TiN samples with lumped element resonators.

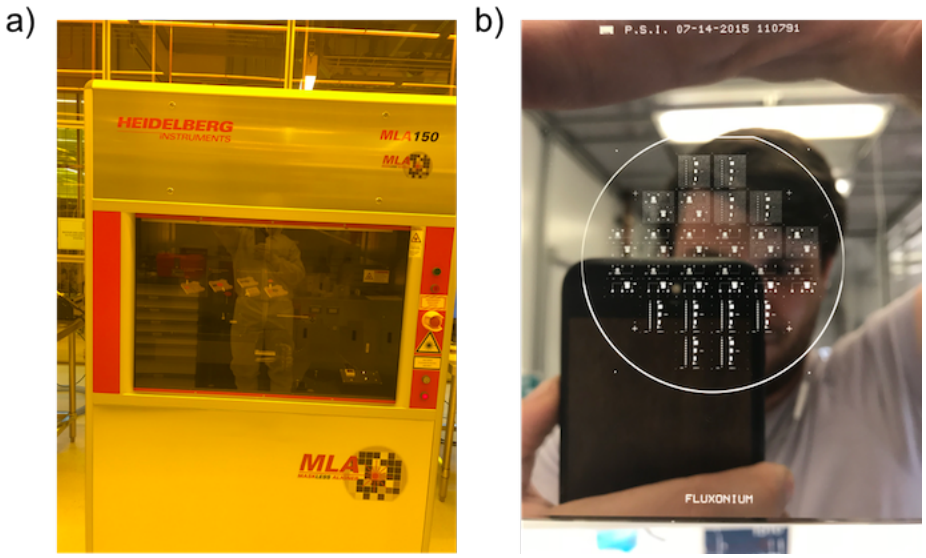

Figure 5.2: a) A Heidelberg laser writer, used to write patterns that are above the optical limit of $\sim 2\mu$m b) A photo of a mask used in mask aligner. This mask was order from a company, but can also be written in the Heidelberg laser writer. When using the mask, one can put it in an optical-stepper and get a higher resolution (down to about 500nm)

to which we will align when doing ebeam lithography. To achieve these optical patterns, we can either use an optical mask which sits over the wafer (see figure 5.2a) or we can use the Heidelberg tool (figure 5.2b) which uses a laser and draws a dxf pattern provided to it. The benefit to the mask is that it can be used in a stepper tool and achieve features down to about 500nm, but the Heidelberg tool provides the opportunity to quickly update the mask file without the need to order a new mask (or make it with the Heidelberg).

- Bake Wafer on hotplate at 150C for 3 min (adhesion issue generally not problematic for optical patterns)
- let cool for 10 seconds
- Spin Resist (AZ 703) at 3500rpm for 45 seconds
- Bake at 95 C for 1 minute
- Expose with Heidelberg tool. (405nm laser. Dose $100\mu J/cm^2$)

- Post-bake at 95C for 1 minute
- Develop in MIF(Az1:1) for Niobium (Aluminum) coated wafers for 1 minute
- quench in DI water bath
- Rinse under DI tap for 3 minutes

Ebeam Lithography

For making our Josephson junction, I used a 100kV SEM ebeam writer. Most recently I have used the Raith Tool (Raith EBPG 5200) as our ebeam writer (Though the device focused on in this thesis was primarily written in a 100kV JEOL tool at Argonne's CNM). Our stack up for Josephson junction fabrication was generally MMA/PMMA as elaborated in the previous section. The exact spin speeds and sub-class of resists used depended on which specific method I wanted to use to realize a chain of junction. In particular we used a cold develop technique with a mixture of IPA:H_20 at 6C for 1 minute and 30 seconds. The exact temperature and time of develop is not very important per se, as a proper dose can be found for a given temperature and time of development, but it should just be ensured that things are kept consistent. Shorter development times will generally lead to less natural undercut, but may come with more variability.

5.1 Cryogenic Setup

In order to conduct our experiments with superconducting circuits, we need to cool them down enough for them to actually superconduct. The T_C varies for different metals that we use, but ultimately - if we wish to study coherence between quantum states - we must cool the sample down enough such that the thermal excitations results in minimal occupation of higher energy states and our device can ultimately cool down to the ground state. To

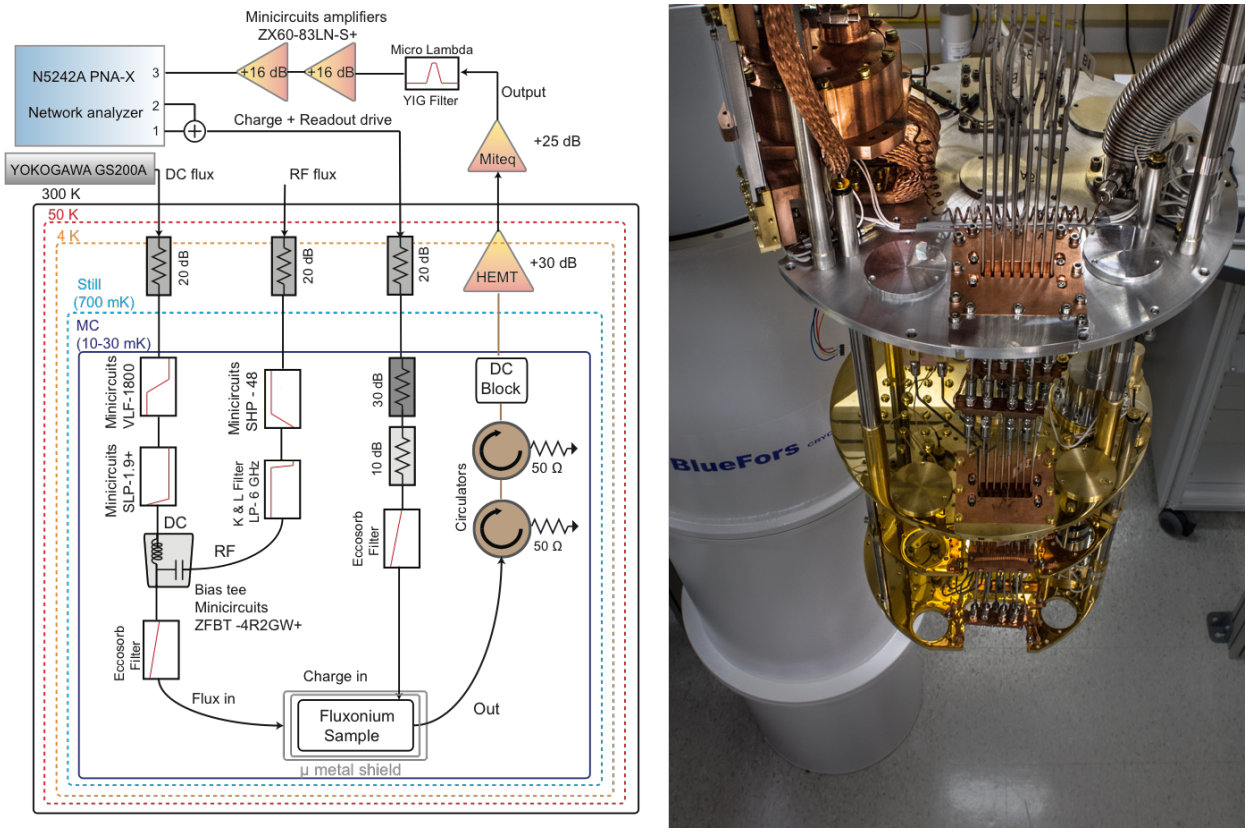

Figure 5.3: a) Wiring Diagram of heavy fluxonium setup. b) Photo of BluFors Dilution Refrigerator used to measure the device. In the photo, the RF lines can be seen in the middle and are thermalized to each stage with copper clamps, machined by myself and Andrew Oriani.

this end, we used a BluFors dilution fridge with a base temperature roughly in the range of 25mK.

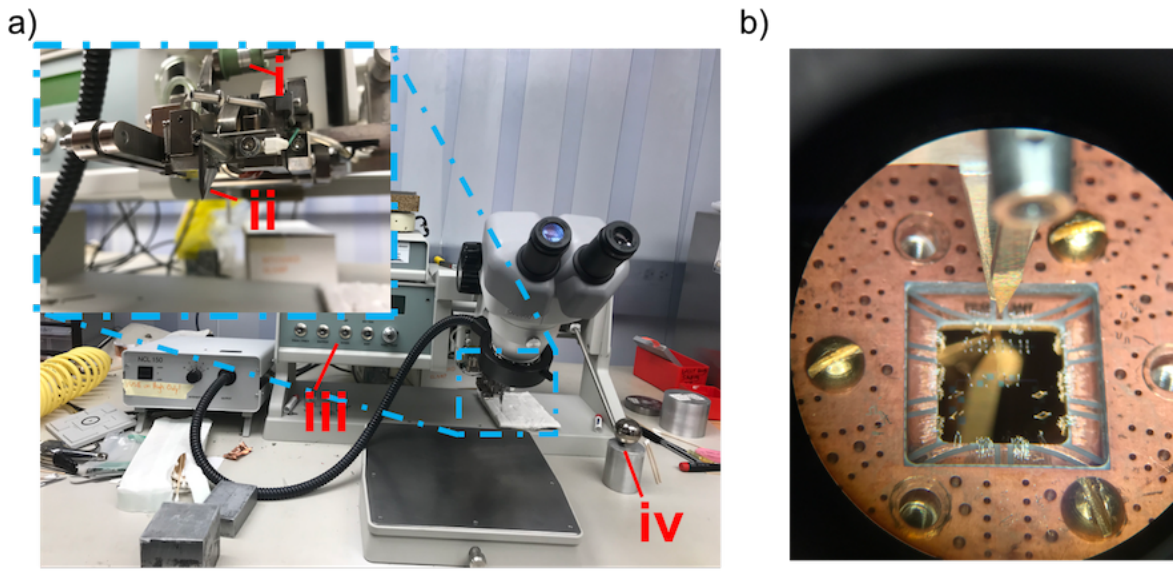

Figure 5.4: a) A westbond wirebonding station, with the upper left inset as a zoom in on the wirebonding needle. i) The Aluminum wire spoil ii) The needle tip with a very small hole in the back to be rethreaded with the wire comes out of the needle head iii) Controls to adjust wirebonding strength and duration iv) The manual 3D manipulator b) An example photo of a TiN sample being bonded

5.2 Sample Mounting

5.2.1 Wirebonding

We used a Westbond Manual Wirebonder (figure 5.4a) to wirebond aluminum wire to our chips and an IBM-style breakout board (figure 5.4b). To ensure a good connection with the ground plane we modified the original IBM design for larger ground plane pads to provide more room for wirebonds, as well and placed indium wire beneath the chip in the sample holder (figure 5.5c) to ensure the chip was firmly pressed up against the IBM board. This indium wire also helped ensure the chip would not move around during wirebonding.

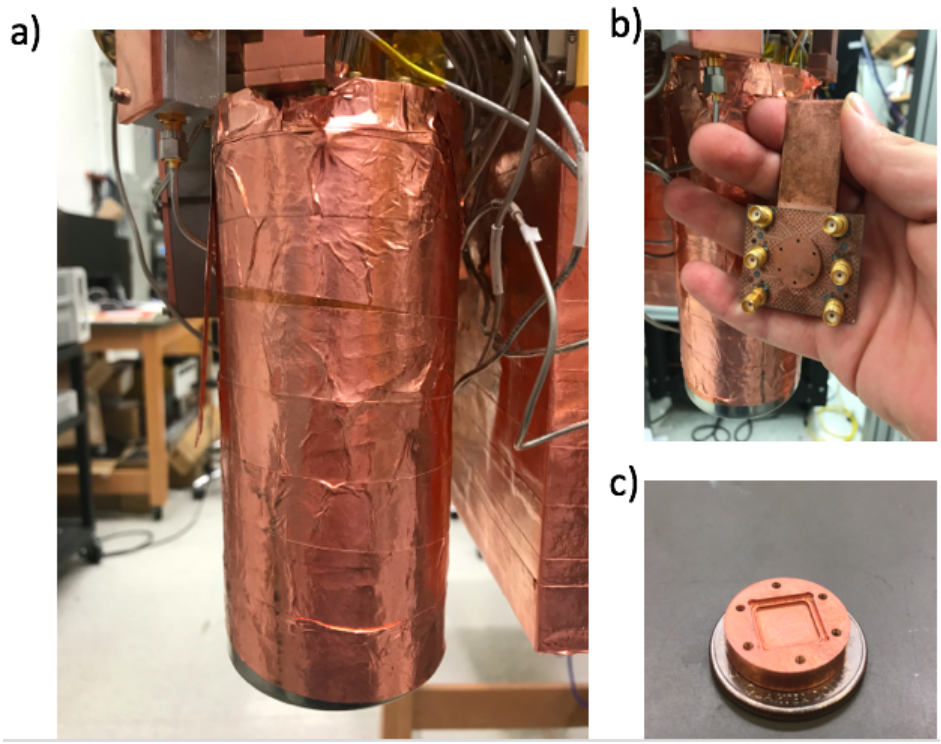

Figure 5.5: a)A μ-metal shield used to shield the sample from externa magnetic fields which is the wrapped in copper tape to help ensure the μ-metal is thermalized. b) An IBM board mounted on a copper post which is then placed inside the μ-metal shield c) A copper cap that holds the chip sample in place against the IBM board. There is a gap beneath where the chip is held to help ensure that the box mode of the board is pushed to higher frequencies as well as to ensure the potential lossy surface currents do not affect the performance of the device being held.

5.2.2 Fridge Mounting/Shielding

Given that the chip is rather small, there needs to be a way in which we can put signals in and out of the sample. This can either be achieved by a 3D mount, or in the case of this thesis using a PCB breakout board. In our lab, we use a modified design of the IBM boards for 2D qubits (see figure 5.4b and figure 5.5b) which is then mounted onto a copper post and put inside a μ-metal shield as shown in 5.5. The cap shown in figure 5.5c is a copper cap in which the chip is placed. Beneath the chip a pocket is cut out to push up the box mode of the sample holder as well to ensure any coupling to currents in the cap would be mitigated.

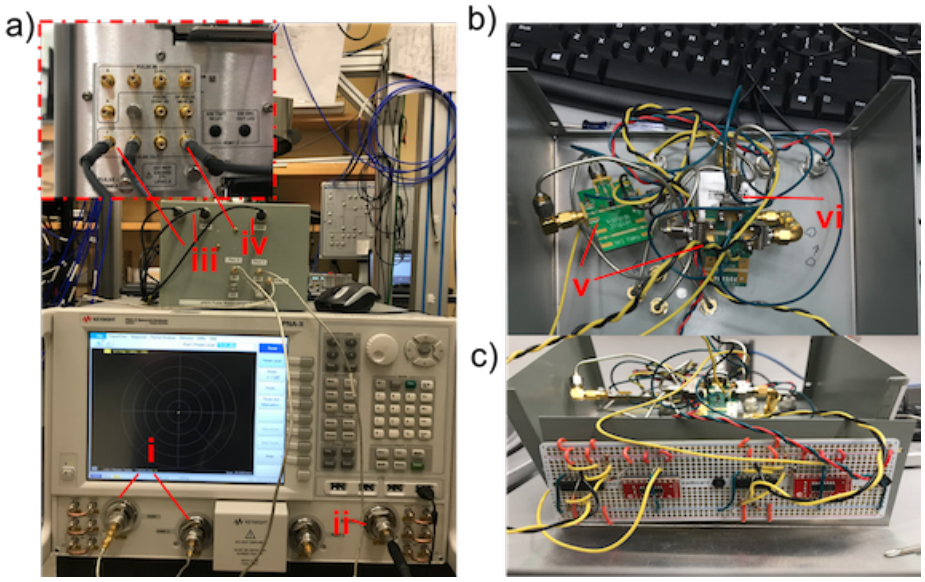

Figure 5.6: a) The microwave measurement set up where we used a Network Analyzer (shown at the bottom) in conjunction with an RF switch connected to the pulse configuration at the back of the NWA. The inset on the upper left shows the back panel of the NWA, which provides TTL logic pulses with programmable duration, for the purpose of pulsed microwave control. i) The two input ports for microwave measurements ii) The output port coming back out of the fridge that does a homodyne measurement and mixes the signals back down to DC. iii) The TTL-logic lines used to control the pulse width and timing of our microwave ports

5.3 Microwave Measurement: NWA

For measurements shown in this thesis, we use a Kiethley 4-port network analyzer (figure 5.6a). This allows us to do both simple 2-port transmission measurements as well as pulsed 2 or 3 tone measurements with the use of the pulse port in the NWA (inset in upper left of figure 5.6a). To do pulsed measurements we used RF switches (figure 5.6b) which were controlled with the TTL logic from the NWA, and the required control circuit for the RF switches.

CHAPTER 6

QUBIT CHARACTERIZATION AND CONTROL

6.1 Initial Qubit Measurement

6.1.1 Is the qubit 'alive'?

When working with superconducting qubits in cQED, the very first experiment is to test if the qubit is 'alive'. In other words, has the qubit survived the entire fabrication process and has a measurable non-linearity and - in some cases - is flux tunable. The first step to see if the non-linearity of the qubit is present is to do a power sweep on the readout resonator and see if a non-linearity is present in the resonator. At high powers the qubit mode will be saturated and you will see the bare-cavity resonance. As the power is swept to lower powers, if there exists a non-linearity, the readout resonance will shift in frequency. In the situation where the only non-linear element (for the relevant power range) is our superconducting qubit, this shift indicates that the qubit is alive and can be studied more carefully to determine its precise properties. (i.e. Is it flux tunable, what is the anharmonicity, lifetime, coherence time, etc.) In the specific case of the heavy fluxonium, as shown in figure 6.2, you will see the presence of a single resonance at high powers and two resonances at lower powers. This frequency shift indicates that our non-linear element is working. The presence of another peak indicates that we have a mode that is non-dispersively interacting with the readout resonator, and with further characterization we determine the higher frequency peak is actually the central plasmon mode from the heavy fluxonium qubit, and the lower peak is the single-photon mode of the readout resonator.

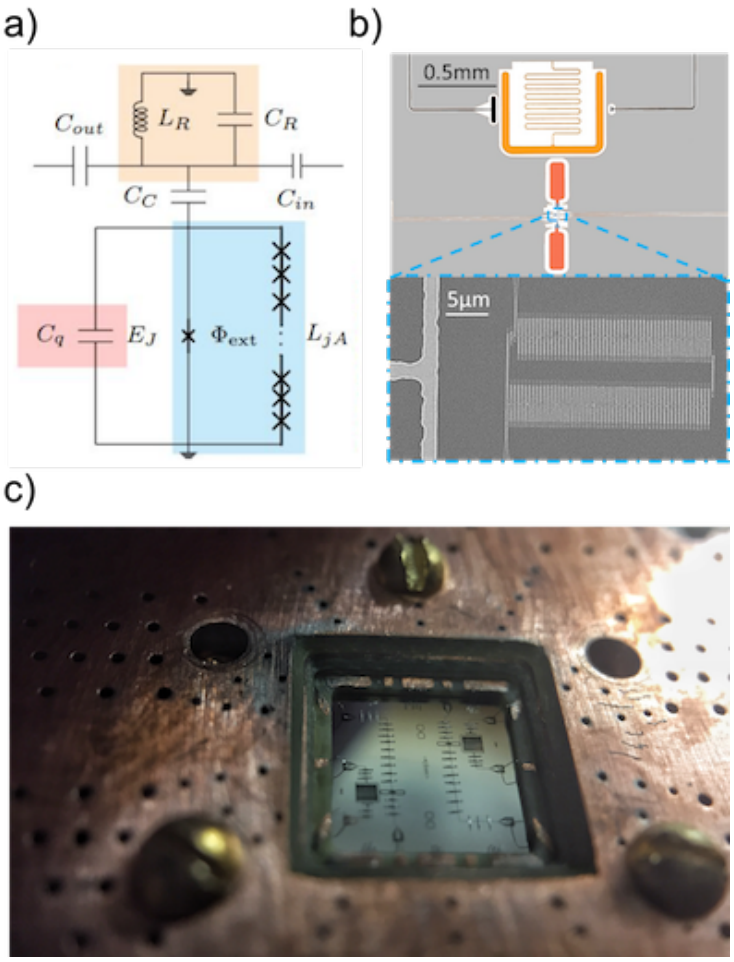

Figure 6.1: a) The circuit diagram of the heavy fluxonium circuit capacitively coupled to a readout resonator. b) A colorized microscope image of the heavy fluxonium circuit coupled to a readout resonator. c) A macro photo of the heavy fluxonium sample mounted and wirebonded to a IBM styled breakout board. There are two samples on the tested chip, but only one of them survived processing and was able to be measured. Measured sample is in the top right side of the photo.

6.1.2 Qubit/Resonator Coupling And Hybridization

Spectroscopy

The appearance of this extra mode in single tone, which we will see shortly is bright over the entire flux quantum, is a unique feature of the device at hand and puts us in a limit in which the plasmon modes and resonator modes blend together. What this means is that photon population of the resonator can also result in a plasmon excitation and vice-versa, and the probability of doing so is represented by the overall intensity of each peak , I_R and I_Q, normalized by the intensity of the bare resonant peak I.

Generally speaking, one must turn to two-tone spectroscopy in order to explore the qubit modes - unless if the qubit is in non-dispersively resonance with the readout. When the qubit mode and readout resonator are in the non-dispersive regime, their coupling can be measure as the splitting of the avoided crossing. While we will have to use two tone spectroscopy to fully characterize the qubit, there is the unique opportunity to measure several features directly in single-tone spectroscopy due to the quasi-dispersive coupling of the plasmon mode. First, by looking at the shift in our resonator frequency as a function of the readout power, we can approximate the coupling strength of our qubit and the resonator. Restricting ourselves to subspace of the resonator and $|g_0, 0_r\rangle \rightarrow |e_0, 0_r\rangle$ mode, we obtain the effective Hamiltonian:

$$H = \begin{pmatrix} \epsilon_R & m \\ m^* & \epsilon_Q \end{pmatrix} \tag{6.1}$$

Where m is the coupling matrix element specific to the plasmon excitation, $m = g\langle e_0|n|g_0\rangle = 0.062i$, and ϵ_R and ϵ_Q are the energies of the readout resonator and qubit plasmon respectively. Diagonalizing H, we find the two lowest excited eigenstates of the system. Near $\Phi_{\text{ext}} = 0$, where the bare detuning is $\epsilon_Q - \epsilon_R \approx 89\,\text{MHz}$, we find the resonator-like eigenstate defined by $(\alpha/\beta)_R = 1.94i$, and the qubit-like eigenstate $(\alpha/\beta)_Q = -i/1.94$. In the

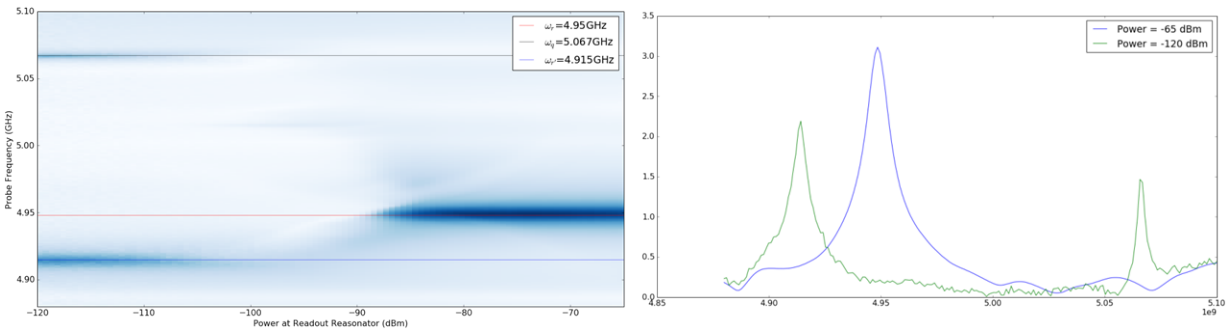

Figure 6.2: Single Tone Spectroscopy power sweep. a) A 2D plot showing the saturation of the heavy fluxonium qubit at high powers ($> -90\,\mathrm{dB}$) revealing the bare resonance, ω_r of the readout resonator. At lower powers ($< -100\,\mathrm{dB}$) the qubit plasmon ω_q and the dressed resonator, $\omega_{r'}$ are seen, revealing the 'plasmonic dispersive' coupling regime. b) A line cut of the two characteristic regimes. The total area under the curve must be conserved, and the bare resonator transmission amplitude is used to normalize the spectra in all the figures.

former, there is a probability of $|\beta_R|^2 = 0.21$ that the qubit will be found in the ($|e_0\rangle$ state, and conversely, in the latter, the same probability that the resonator will be found in its $|1\rangle$ state.

Since both resonance lines are read from the resonator, their relative intensities are given by the relative probabilities of finding the resonator in its $|1\rangle$ state,

$$I_R/I_Q = |\alpha_R/\alpha_Q|^2 = 3.8, \tag{6.2}$$

and a rough comparison of resonance peak heights times linewidths is consistent with this estimate, as shown in figure 6.2b. As Φ_{ext} is increased and the detuning is reduced, the eigenstates exhibit further hybridization. At $\Phi_{\mathrm{ext}} = 1/2$, for example, the predicted intensity ratio is reduced to $I_R/I_Q = 2.6$.

6.2 Single Tone Spectroscopy

6.2.1 Spectrum

Overview of Spectrum

To start the characterization of our device, we tune it with flux and measure the change in the spectrum, as seen in figure 6.3a. The single tone spectrum consists of two peaks, one the is 'mostly resonator' and another that is 'mostly plasmon'. This device has the unusual feature that there is a qubit mode that is bright over the entire flux range -$\frac{1}{2}\Phi_0$ to $\frac{1}{2}\Phi_0$. This is due to the fact that the plasmon is non-dispersively coupled to the readout resonator, and this plasmon resonance does not change very much with flux as this transition exists in a single well. The corresponding potential energy landscape for the qubit, as shown in figure 6.3b, helps show the various transition features.

Finite Temperature Affects

If this device was perfectly thermalized, and the fridge was at T=0K, we could expect that the device would always cool down to the ground state after some externally-induced excitation. However, since the fridge (and consequently the device) is at a finite temperature of ∼30mK, it will have a finite expectation in the excited state. We can approximate the temperature of the device by measuring the excited state probability and using the Boltzmann factor, which is generally given by:

$$\rho_0^{(1)} = \frac{e^{-\beta H_0}}{Z} \tag{6.3}$$

Where Z is the partition function of our system. In the specific case of the fluxonium, this relation becomes a bit more complicated due to the rich availability of different excitation and the extending lifetime of the localized ground states. However, if we simply treat it as

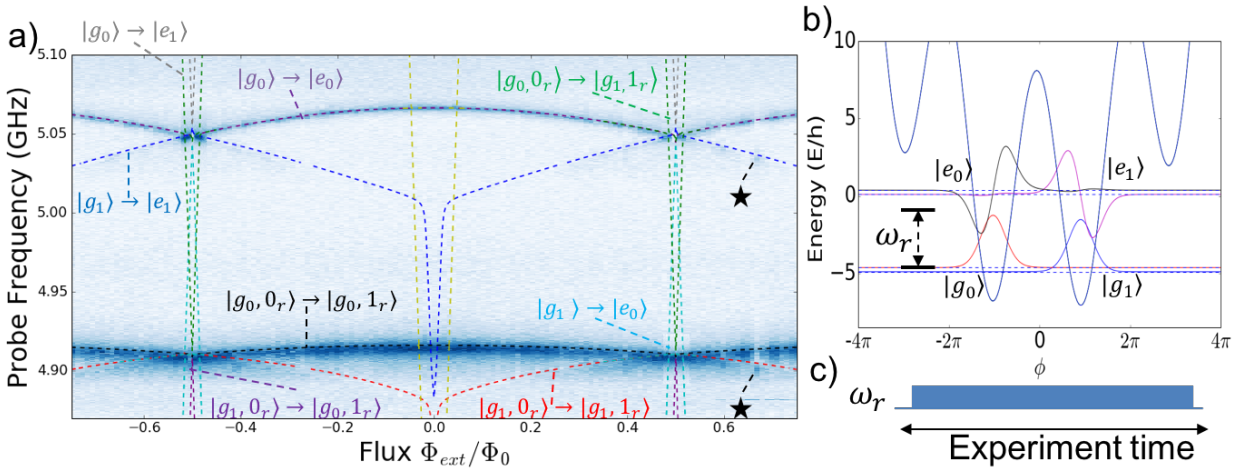

Figure 6.3: a) Single-tone spectroscopy of the fluxonium-resonator system in the vicinity of the resonator and primary plasmon transition frequencies. Dashed lines indicate simulated energy levels of the coupled system based on device parameters extracted from fits to single and two-tone spectra, and are labeled with the corresponding transitions. The resonator stays in the $|0_r\rangle$ state, unless otherwise noted. The star indicates a momentary qubit inversion, with a shift in both the plasmon peak, and the resonator peak. This qubit inversion seems to be a feature found in many different heavy fluxonium experiments, and occurred for varying lengths of time. b) The corresponding energy levels, shown near half-flux quanta. c) An indication of the experiment being carried out. Specifically, this is a single-tone continuous wave measurement

a two-level system, equation 6.3 becomes the well-known relation:

$$\frac{p(g_1)}{p(g_0)} = e^{-\beta(E_{g_1} - E_{g_0})}$$

Where $\beta = \frac{1}{kT}$. A full treatment of the device, however, is needed to appropriately account for full steady-state driven nature of the device. (Because the device has timescales of very different magnitude, the master equation takes an unreasonably long time to simulate and accumulates large errors with integration time.) To overcome this issue, one can approximate the steady-state of the device with linblad operators, where the short time dynamics are integrated out, and generating the plots shown in figure 6.4. A good match between theory and experiment are seen for a finite temperature simulation. Take note that the occupation of the $|g_1\rangle$ state is increased, and fully occupies the $|g_1\rangle$ state (switching primarily to the $|g_1\rangle \rightarrow |e_1\rangle$ branch) at around $\Phi_{\text{ext}} \sim 0.43\Phi_0$, which is in line with the Boltzmann distribution approximation in equation 6.3 and the fact that our $\omega_{g_0 g_1}$ transition is around 700MHz. This branch switch in the reason we do not see the avoided crossing in figure 6.5, marked with a black star, as the avoided crossing is associated with the qubit starting off in the $|g_0, 0_r\rangle$ state, but our device has been thermally excited to the $|g_1, 0_r\rangle$ state.

6.2.2 Half-flux Features

Qubit-like Feautres: Fluxoid State Couplings

Due to the quasi-dispersive coupling, we are able to extract useful information directly from single-tone data, particularly when we look closely at the qubit-like peak around half-flux quantum. Looking at the single tone data in figure 6.5a we can see, in addition to a good fit between theory and experiment, a rhombus shaped avoided crossing. In figure 6.5a we note how at very close to a half flux quantum, intra-well plasmon transitions become symmetry forbidden, and therefore the transmission at this point goes to zero. In place of this transition

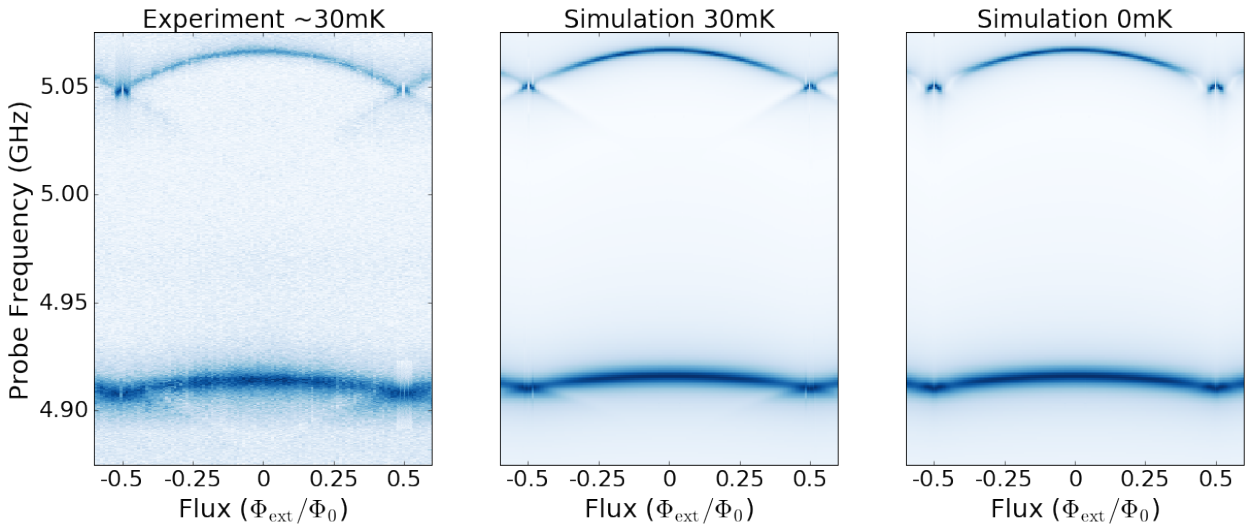

Figure 6.4: a) Single-tone spectroscopy of the fluxonium-resonator system data. b) Simulation of the system at 0mK. c) Simulation of the system at 30mK. When comparing simulations at zero and finite temperatures, we can see an increase occupation of the $|g_1\rangle \rightarrow |e_1\rangle$ branch as the qubits transition $|g_0\rangle \rightarrow |g_1\rangle$ approaches kT.

we see our inter-well transitions ($|g_0\rangle \Rightarrow |e_1\rangle$ and $|g_0\rangle \Rightarrow |e_1\rangle$) light up. The splitting of these peaks represents that fact that the higher plasmon energy levels ($|e_{0,1}\rangle$) couple at precisely half-flux, and the splitting of these two peaks is a direct measure of twice the coupling strength, $t_e \approx 7\,\text{MHz}$. In principle, this coupling indicates that these energy levels could be used as a way to create a Λ system and couple our ground states via a Raman transition. However, due to the low Q of our readout resonator and the hybridization of with our readout resonator, these energy levels did not suffice for us to realize our Λ system. Though we cannot resolve the ground state coupling experimentally, again due to the low-quality factor blurring out this avoided crossing, we can infer from simulations that the ground state coupling, $t_g \approx 0.4\text{MHz}$, a thousand times smaller than the original fluxonium design. We can gain a sense of intuition about why this is true by approximating our fluxonium as

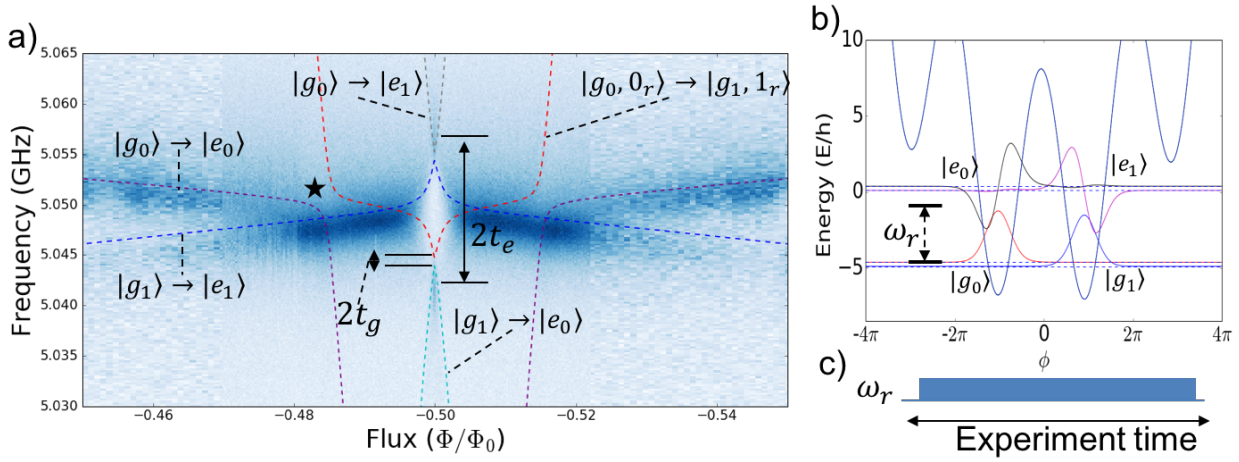

Figure 6.5: a) Single-tone spectroscopy of qubit-like peak for the fluxonium-resonator system data. From this measurement, we are able to directly measure the splitting of the $|e_0\rangle$ and $|e_1\rangle$ states, giving a t_e ≈7MHz. From fits, one can infer the coupling of the ground states $|g_0\rangle$ and $|g_1\rangle$ is t_g ≈0.4MHz, which is comparable with the modeled $|g_0, 0_r\rangle \rightarrow |g_1, 0_r\rangle$ at half flux quanta. The star indicates an avoided crossing not observed in this figure, but will be seen in when the qubit is in a persistent negative temperature state. It is not present in the spectrum shown here because the qubit occupies the excited $|g_1\rangle$ state when $\omega_{g_0 g_1}$ is comparable to kT. This avoided crossing is a composite coupling between $|g_0, 0_r\rangle \rightarrow |g_1, 1_r\rangle$ and $|g_0, 0_r\rangle \rightarrow |e_0, 0_r\rangle$. b) The corresponding energy levels to help guide corresponding transition. c) An indication of the experiment being carried out. Specifically, this is a single-tone continuous wave measurement

a four-level system near $\Phi_{\text{ext}} \approx 0.5\Phi_0$:

$$H = \begin{pmatrix} E_{g_0} & -t_g & 0 & 0 \\ -t_g & E_{g_1} & 0 & 0 \\ 0 & 0 & E_{e_0} & -t_e \\ 0 & 0 & -t_e & E_{e_1} \end{pmatrix} \tag{6.4}$$

Furthermore, from the numerical diagonalization shown in figure 6.5, we can see that there is an avoided crossing between $|g_0, 0_r\rangle \rightarrow |e_0, 0_r\rangle$ and $|g_0, 0_r\rangle \rightarrow |g_1, 1_r\rangle$, which is not readily seen in the data. This is likely due to the lack of occupation in the $|g_1\rangle$ state in figure 6.5a due to the thermal excitation of the device. But, this avoided crossing, surprisingly,

will be readily seen when we discuss the negative temperature state of the device in a few sections.

Resonator-like Features: Composite transitions

Turning our attention to the resonator-like feature near half flux in figure 6.6, we take note of two sets of avoided crossings. The outer avoided crossing arises from $|g_1, 0_r\rangle \rightarrow |g_1, 1_r\rangle$ coming into resonance with $|g_1, 0_r\rangle \rightarrow |e_1, 0_r\rangle$ and is visible due to a slight thermal occupation of the $|g_1\rangle$ state.

Meanwhile, the two inner avoided crossings are the result of the hybridized transitions $|g_1, 0_r\rangle \rightarrow |g_0, 1_r\rangle$ and $|g_0, 0_r\rangle \rightarrow |g_1, 1_r\rangle$ coming into resonance with our readout resonator. Physically these avoided crossings indicate that the presence of a photon in the resonator increases the coupling of the fluxon states. This increased coupling between our fluxon states $|g_0\rangle$ and $|g_1\rangle$, will also be readily seen in the photon assisted transitions. Interestingly, we will see the inner composite avoided crossing disappear when the device goes into its persistent negative temperature state, and the appearance of several crossings in place of the outer avoided crossing seen in figure 6.6, which will be discussed in the next chapter. I would also like to remind the reader that we are taking the simplified version of these transitions, and as such one must be careful to not over interpret the physical implications with the simplified labeling.

6.3 Two-Tone Spectroscopy

Once one has exhausted the information to be had from single tone data, one can move onto two-tone measurements in order probe the qubit energy levels that are not seen in single tone, which will be the qubit energy levels that are dispersively coupled to the readout resonator. Since the fluxoid states of interested (namely, $|g_i\rangle$) are engineered to be weakly coupled, we must drive at high powers in order to observe these transitions. As a result,

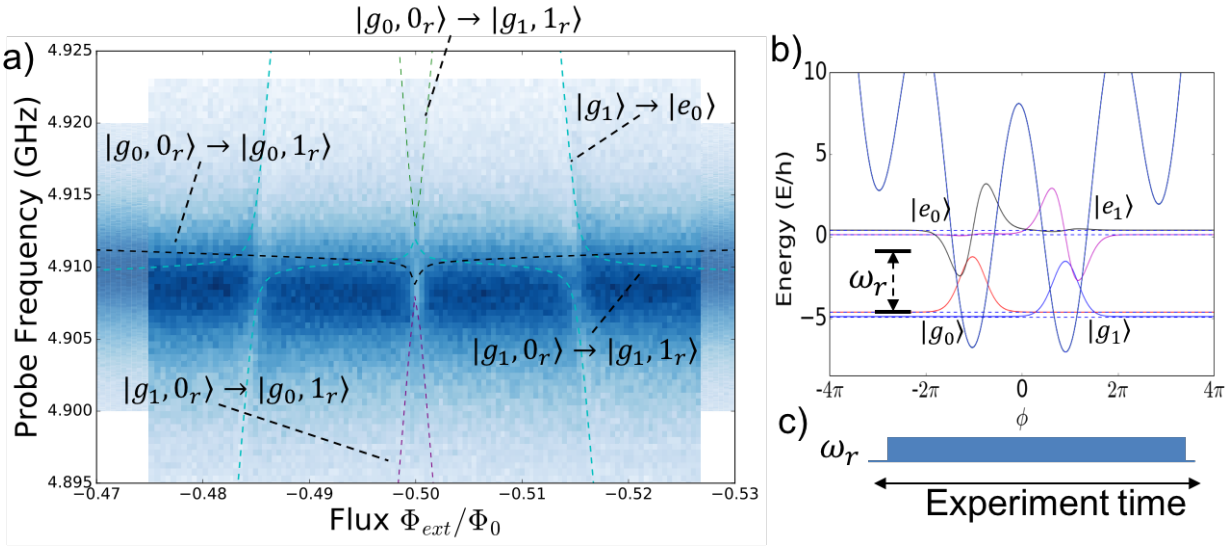

Figure 6.6: a) Single-tone spectroscopy of the resonator-like peak in fluxonium-resonator system. Note the very weak signs of the avoided crossing corresponding to the qubit being in the $|g_1\rangle$, likely due to thermal excitation to this state. Further, at precisely half-flux quanta the resonator transmission goes down. This is due to the composite avoided crossings, in which fluxoid states are exchanged for a photon. This indicates that fluxon transitions coupling is increased with the presence of a photon in the resonator (and further supported by the photon/plasmon assisted transitions to be discussed) b) The corresponding energy levels to help guide corresponding transition. c) An indication of the experiment being carried out. Specifically, this is a single-tone continuous wave measurement with a tone at ω_r

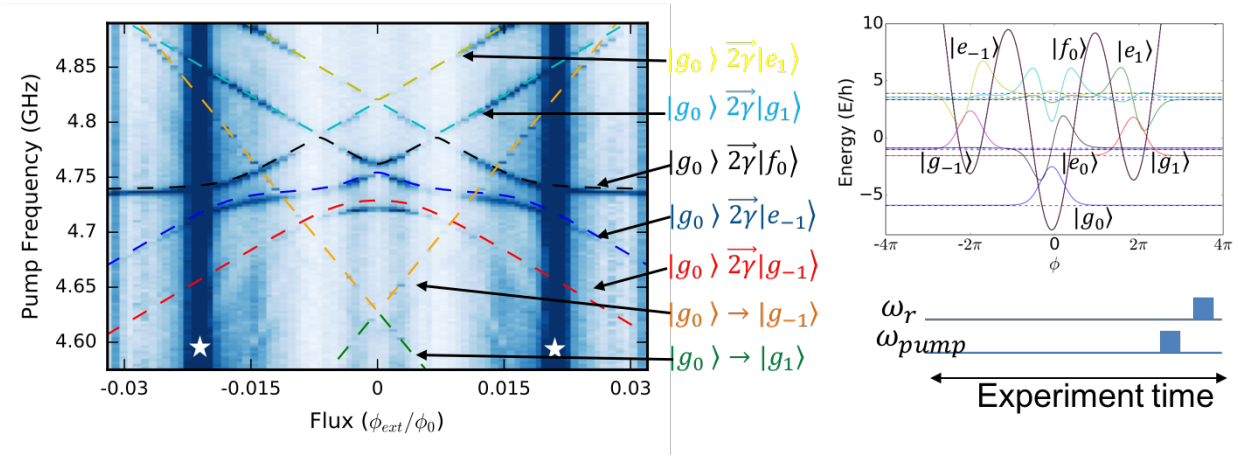

Figure 6.7: a) A two tone spectroscopy scan of the qubit modes near zero flux. Transitions are labeled with the corresponding transition, and are either single photon or two photon transitions (indicated with a right arrow and a '2γ'. The white star is to indicate the this is when the resonator blanks out, due to coming into resonance with the $|g_0, 1_r\rangle \rightarrow |e_{-1}, 0_r\rangle$ transition. In other words, at this flux point, a photon in the resonator translates into an excited fluxon transition, and pumps the qubit into the $|g_{-1}\rangle$ state. b) The corresponding energy levels near $\phi_{\text{ext}} = 0 \cdot \Phi_0$ to help guide corresponding transition. c) An indication of the experiment being carried out. Specifically this is a two-tone pulsed measurement, in which the readout tone (at ω_r) is never on during the driving of the qubit modes (at ω_{pump})

in these high-power drives, we will also drive two-photon transitions to the higher energy plasmon-like manifold, which will also reveal the couplings of these energy levels.

6.3.1 Direct Drive of the Fluxon transition

We start off by looking at transitions associated with single-photon features in our two-tone data. As seen in figure 6.7a, we see two sets of transitions with the greatest slope, corresponding the direct drive of the fluxon transition. Though these transitions of engineered to be weakly coupled, we are still able to see them near zero flux when driving strongly enough. As we tune away from zero flux, the charge coupling matrix element of these transitions becomes further suppressed (as seen in figure 3.6), eventually making it impossible to see the direct transition without the power of our drive exceeding the cooling power of the base

stage. This direct transition was visible down to about 3GHz (a flux value of $\approx 0.2\Phi_0$ and a coupling matrix element of ≈ 0.02MHz). Since we are able to see the direct transition, it is worth trying to coherently couple these states and perform a Rabi oscillation, which can be seen in figure **??**.

6.3.2 Two-photon features: Formation of a Λ system

All of the other transitions in figure 6.7 are the result of two-photon transitions to our higher energy manifold. These two-photon features will be the basis of our Λ system. These transitions clearly indicate the coupling strength of our secondary plasmon wavefunctions. As we either adjust the detuning of the plasmonic-dispersive feature (and the consequential hybridization of the device), or as we tighten the bands of the different transitions, we change the exact nature of these transitions, which is discussed in the previous fluxonium theory chapter.

Resonator-Photon blanking

As seen in figure 6.7, we notice that, even at single photon measurement powers and pulsed measurements, there is a blanking out in the resonator at around $\Phi_{\text{ext}} \sim 0.02\Phi_0$, creating a vertical band. This is the result of a photon-assisted transition crossing the resonator. More specifically, it results from the composite transition $|g_0, 1_r\rangle \rightarrow |e_{-1}, 0_r\rangle$ coming into resonance with our $|g_0, 0_r\rangle \rightarrow |g_0, 1_r\rangle$ transition, which serves to pump the device into the $|g_{-1}\rangle$ state. This blanking becomes readily apparent when the single tone read powers are put slightly above the single photon limit (see figure 9.1). In this figure, I have included a 'medium' power scan of the single tone spectrum. At these powers with several photons, we can see multiple instances in which the resonator in blanking out from coupling to photon assisted transitions, and can even see a fluxon transition in single tone at higher powers. These features have not been seen in a more recent fluxonium sample, and appear to be the

result of our qubit/resonator hybridization.

6.3.3 Raman Transition

Identifying Energy Levels

Now that we have identified our energy-levels of interests in order to form a Λ transition, we can perform a Raman transition by sweeping a third tone ω_{probe} hoping to satisfy the condition:

$$2\nu_{\text{pump}} - \nu_{\text{probe}} = E_{g_1} - E_{g_0} \tag{6.5}$$

Once this condition is satisfied, we will get a dip in our readout resonator, as is signified by the dashed line in figure 6.8a. The other features in this spectrum have not been fully determined. Exploring known transitions indicate possible signatures of photon assisted transitions for a few of the peaks. Focusing on the transition of interest, beyond ensuring that the energy levels match according to equation 6.5, we confirmed that we are addressing the proper level by:

- Lifetime measurements with Raman gate match up with direct drive and plasmon pumping lifetime measurements
- The slope of the energy transition corresponds with a two-photon feature
- (Not shown) The change of the energy values as a function of the applied external flux behaved according to expectations

Direct Rabi Drive Attempt

Going with the typical route of trying to prepare a superposition state of $|g_0\rangle$ and $|g_1\rangle$ we start off by trying to drive the transition directly in figure 6.9. We start off in figure 6.9a

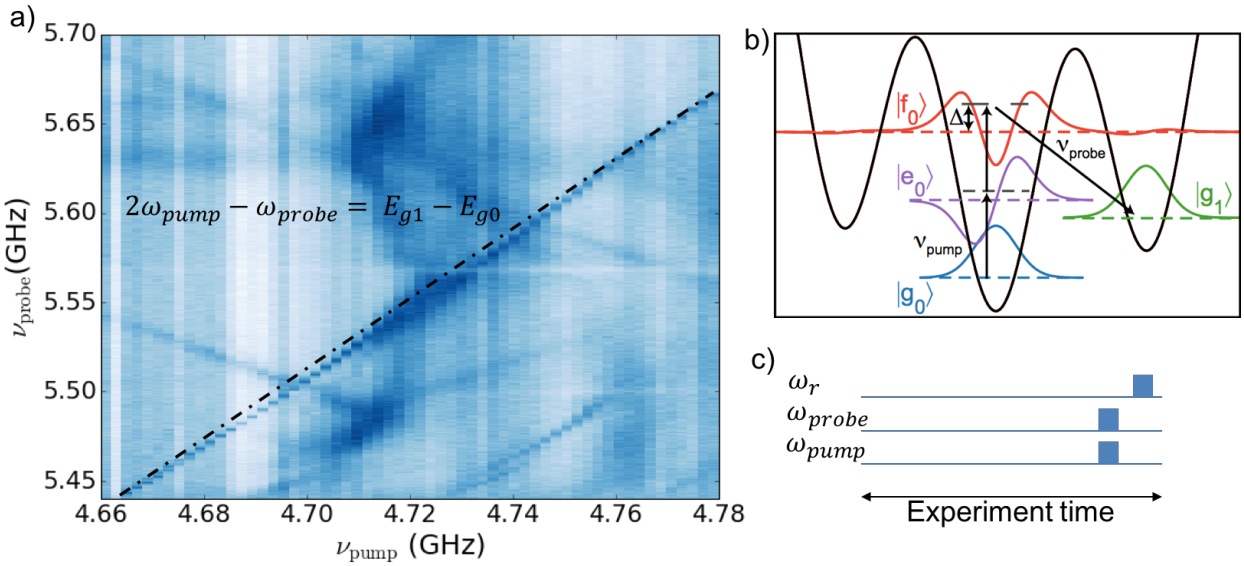

Figure 6.8: a) Pump-probe spectroscopy of Raman transitions between $|g_0\rangle$ and $|g_1\rangle$ as a function of pump (near $|g_0\rangle \rightarrow |f_0\rangle$-$2\gamma$ transition) and probe frequency (near $|g_1\rangle \rightarrow |f_0\rangle$). The Raman transition is seen when $2\nu_{\mathrm{pump}} - \nu_{\mathrm{probe}} = E_{g_1} - E_{g_0}$, represented by the dashed line. b) The wavefunctions of the states involved in the Raman transition. The intermediate $|f_0\rangle$ state couples to $|g_0\rangle$ via a two-photon process, and has a small amplitude in the right well, with a direct dipole-allowed transition to the metastable $|g_1\rangle$ state. The dashed lines are simulated energy levels of the fluxonium-resonator system. c) An indication of the experiment being carried out. Specifically, this is a 'two-tone' pulsed measurement, in which the readout tone (at ω_r) is never on during the driving of the qubit (at ω_{pump} and ω_{probe})

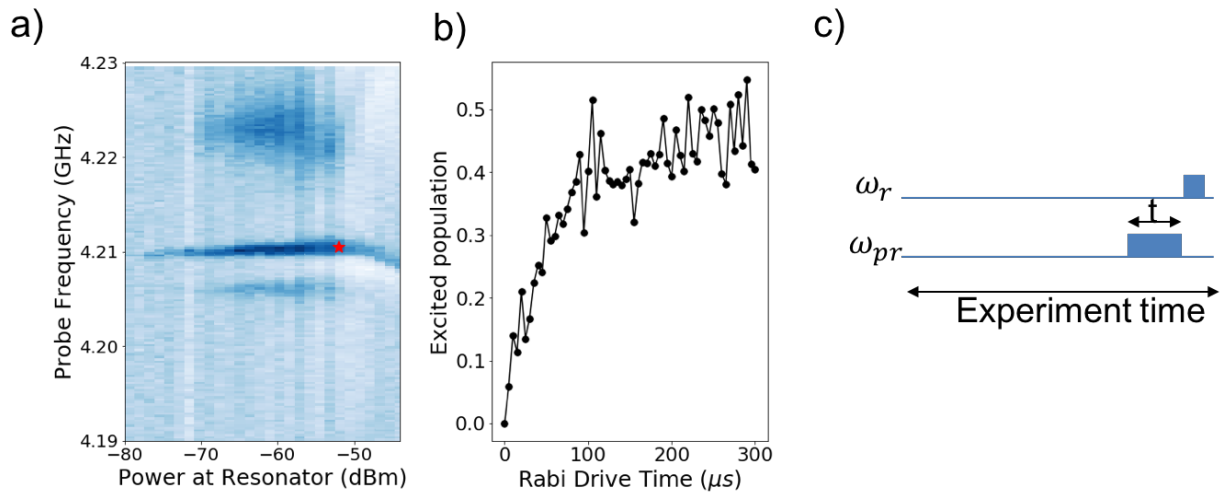

Figure 6.9: a) Power Sweep where we identify the maximum width of the direct fluxon transition. b) The rabi attempt, demonstrating the forbidden nature of the $|g_0\rangle \rightarrow |g_1\rangle$transition as . c) An indication of the experiment being used. A pulsed measurement in which the qubit transition $|g_0\rangle \rightarrow |g_1\rangle$ is being driven directly, for varying lengths of time, t, followed by a readout tone at the readout resonator frequency ω_r.

by sweeping our driving power, finding where the direct transition resonance has the largest width. This should be the point of maximum energy transfer, and correspondingly the fastest Rabi gate. However, we can see in figure 6.9b that even at this point, the Rabi oscillation takes on the order of $\sim$150μsec, just to obtain a 50/50 classical mixture state.

Raman Rabi Drive

Since driving on the $|g_0\rangle \rightarrow |g_1\rangle$ direct transition cannot induce a coherent Rabi oscillation, this gate alone would result in us having more of a classical bit, than a quantum one. In order to appropriately claim that we have a qubit, we must be able to induce a superposition state. The reason that the direct drive takes so long to couple our two local ground states is because these states are well isolated in their individual wells (Which also is what gives the qubit it's to be seen longer lifetime.) With this in mind, we then look to other energy levels that have a decent wavefunction amplitude it both wells of interest, namely the $|f_0\rangle$ state that forms the lambda system shown in figure 6.8b.

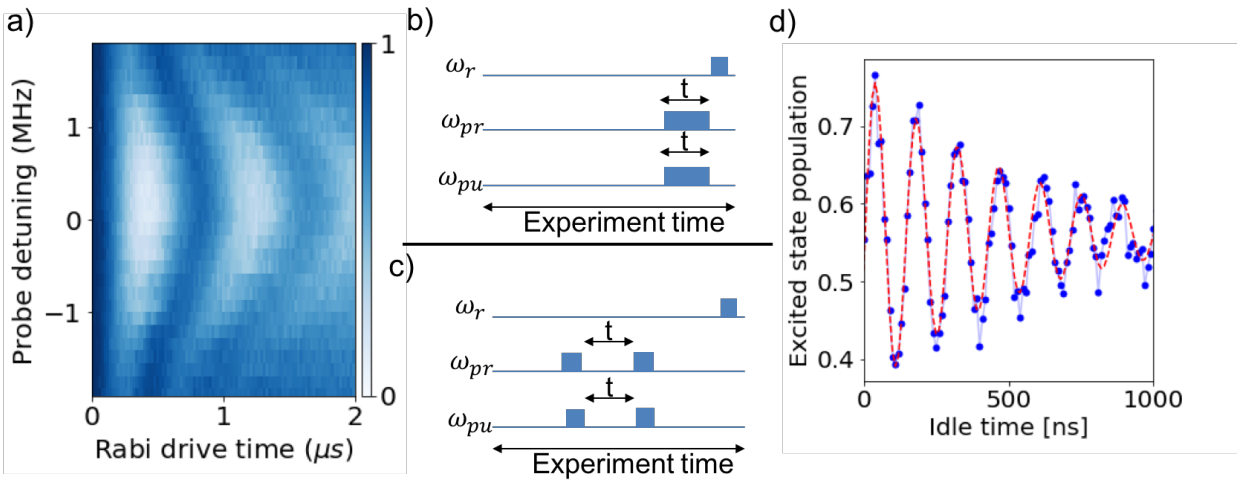

Figure 6.10: a) Demonstration of a successful Rabi oscillation with a T_π of $\sim$ 440nsec, a substantial improvement in the very slow excitation seen in figure 6.9b. Here you can see the typical chevron patterns which arise from an increase rabi oscillation when driving slightly off resonance. b) A demonstration of the 'three tone' Raman rabi experiment. c) Demonstration of the 'three tone' Ramsey experiment. d) A Ramsey experiment, which allows us to directly measure the T_2 of the device.

6.4 Two-tone experiments: Increase coupling of fluxon states

An interesting aspect of this device is the increased coupling of fluxon states with the presence of a photon in the readout resonator, or an excitation in the plasmon of the qubit. Due to the low Q nature of the resonator/plasmon modes, these transitions cannot be used to coherently control the qubit.

6.4.1 Photon/Plasmon-Assisted Transitions

Photon Assist

Initial measurements of the device were done in a continuous wave method, in which both the readout tone and the driving tone are on at the same time. This resulted in there being photon assisted transitions very near our readout resonator as seen in figure 6.11. These transitions are further indication that the coupling of states in different wells is increased

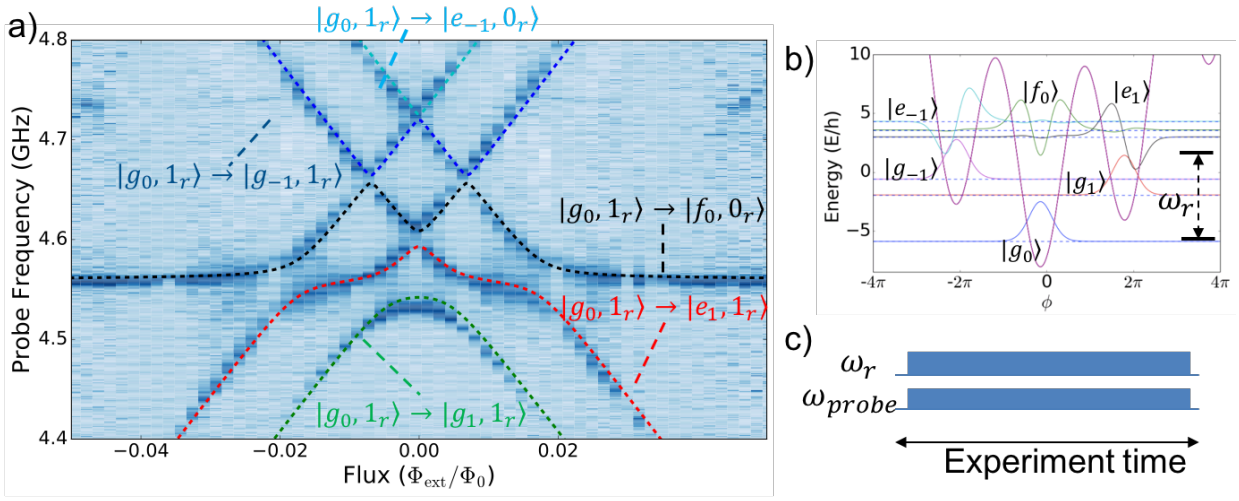

Figure 6.11: Two-tone spectroscopy as a function of flux (near zero flux) showing (a) resonator-photon and (b) plasmon assisted transitions. In (a) the readout tone is placed at the resonator frequency and the transitions start with the fluxonium-resonator system in $|g_0\rangle \otimes |1\rangle$. In (b), the 'readout' tone is placed at the plasmon frequency and the transitions start with the fluxonium-resonator system in $|e_0\rangle \otimes |0\rangle$. In each case, the transmission of a readout tone is monitored, while the frequency of a second drive tone is swept (y-axis). Both sets of transitions are absent when the drive and readout tones are pulsed and staggered, as a result of the short lifetimes of both the resonator and the plasmon. (State labeling for the transitions is valid for $\Phi_{\text{ext}} > 0$.)

when there is a photon present in the readout resonator. Interestingly, this feature of the device could prove to be useful is photon detection schemes underway for the detection of dark matter [49, 50]. These photon-assisted transitions were done at the single photon level, and demonstrate how the forbidden fluxon states coupling can be enhanced with the presence of a photon in the resonator. This may also prove to be useful for future experiment, where a single photon is placed in a higher Q cavity plasmonicaly coupled to the heavy fluxonium, and then exchanged for a fluxon as a way to realize gates between forbidden transitions (see outlook chapter). The exact nature of these photon assisted transition is not fully understood and will be part of future explorations.

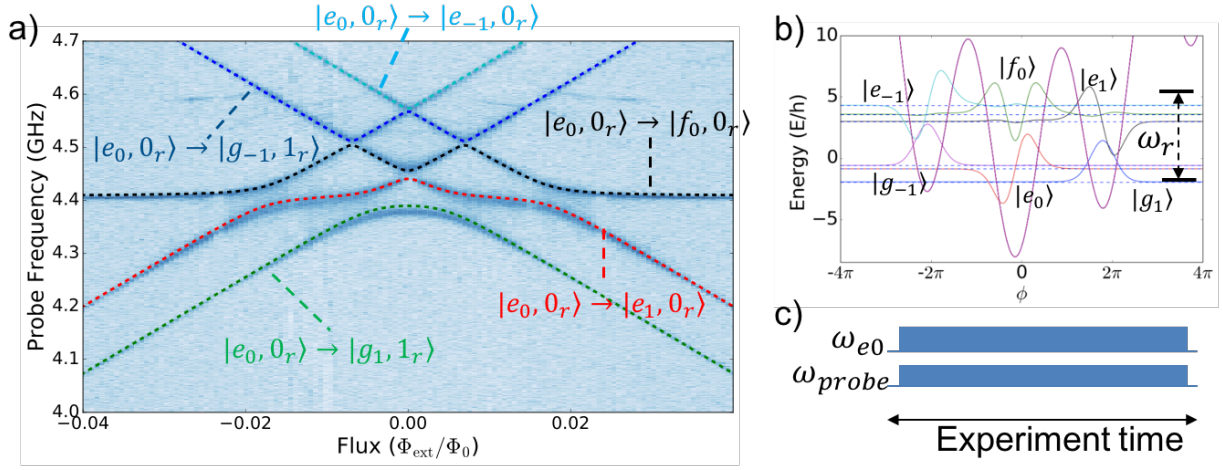

Figure 6.12: a) Plasmon Assisted transitions near zero flux. Due to the low Q readout resonator, and the resulting Purcell limitation of the plasmon mode, these transitions cannot be used to form a Λ system. b) A guide of the energy landscape and the relevant energy wavefunctions, as well as the approximate scale of the resonator energy c) An indication of the experiment being carried out. Specifically, this is a two-tone continuous wave measurement, in which the readout tone (at $\omega_{g_0e_0}$) is on during the driving of the qubit modes (at ω_{probe})

Plasmon Assist

Given the bright nature of the plasmon peak, due to the quasi-dispersive regime that this device is in, we are able to do fluorescent readout on the plasmon peak directly. When doing this in a continuous wave manner (in which both the read and the drive tones are on at the same time), we can see a set of transitions corresponding to the initial occupation of the plasmon mode as seen in figure 6.12a. Due to the low Q readout mode causing a heavy Purcell limitation of the $|e_0\rangle$ mode, we are unable to use these modes as a way to induce coherent oscillations between our disjoint fluxoid states. Future interactions of this device would improve through the slight increase of the readout Q. A Q of 5,000 should suffice as this will allow for easy rabi oscillations of the plasmon mode, but without requiring very slow readout.

6.4.2 Plasmon Pumping

Due to the finite matrix elements between $|g_0\rangle$ and $|e_1\rangle$ (or $|g_1\rangle$ and $|e_0\rangle$), we are able to drive directly on the intra-well transitions as a way to either pump the device into the excited state, or as a way to reset the state of the device. This feature was particularly useful in the characterization of the device, as it allowed for an easy method to prepare the device in the excited state, as a way to measure the T1. Namely, by driving on the $|g_0\rangle \rightarrow |e_0\rangle$ transition, we will eventually pump ourselves into the $|g_1\rangle$ state. Similarly, we can drive on the $|g_1\rangle \rightarrow |e_1\rangle$ transition as a way to reset the device to the $|g_0\rangle$ (this feature will be discussed shortly as a way to measure the nature of the qubit inversion.). This method of state preparation in akin to optical pumping in atomic physics, used for such purposes as realizing a laser.

For our purposes, this method of state preparation is useful in determining the readout fidelity for a given set of readout parameters. Since this state is difficult to access (by design), we can make full use of the plasmon pumping feature to easily (but incoherently) put our device into the $|g_1\rangle$ state. This can then give a baseline for knowing if the loss of fidelity in our Raman gates is coming from poor state preparation, or other means. Figure 6.13 is an example of such a state preparation and two different drive parameters. In both cases, we keep our readout time and power constant (in the few photon limit and a read time of $\sim$150μs) and cycle on the $|g_0\rangle \rightarrow |e_0\rangle$ transition for different amounts of time. In 6.13a, it was done for 1millisecond, while in 6.13b, the cycling was only done for 100μs. A more careful experimentation of these features, varying pump times and powers, would determine the optimal pumping parameters.

6.5 T_1 Measurements

Now that have identified all relevant transitions of the heavy fluxonium circuit capacitively coupled to a readout resonator, and the various methods one can use to prepare the state

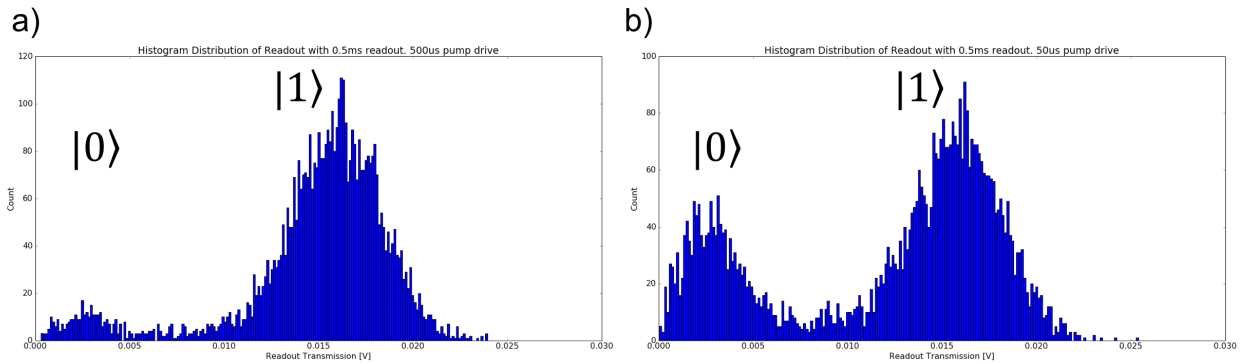

Figure 6.13: A demonstration of two different plasmon pumping schemes. In either figure, we keep the readout time and power constant. In the left figured, we drive for an extending period of time (longer than T_1, and nearly fully pump ourselves into the $|g_1\rangle$ state. By contrast, the figure on the right is the result of only driving for $\sim$50μseconds. This leads to a decreased occupation in the excited state. The left-hand plot can be used as a way to set amplitudes when determining the fidelity of a coherent gate.

of our device, we can bare the fruits of our labor and measure the T_1 nearly over the entire flux quantum, with $|\Phi_{\text{ext}}| < 0.45 \cdot \Phi_0$. As we approach half flux quantum, the χ-shift of our readout resonator becomes small in comparison with the width of the readout peak since our readout Q was very low at Q_{readout} $\sim$500. Though in principle a higher Q readout mode should make it feasible to measure the T_1 all the way to $\Phi_{\text{ext}} = 0.5 \cdot \Phi_0$. As can be seen in figure 6.14, measurements of the T_1 show that there is an increase in the lifetime as we approach half-flux quantum. More specifically, we can see that this increase is proportional to the inverse of the square of our charge matrix element (purple dashed line), indicating that the T_1 of the device is limited by dielectric loss in the capacitor (in agreement with the results published at the same time by [11]).

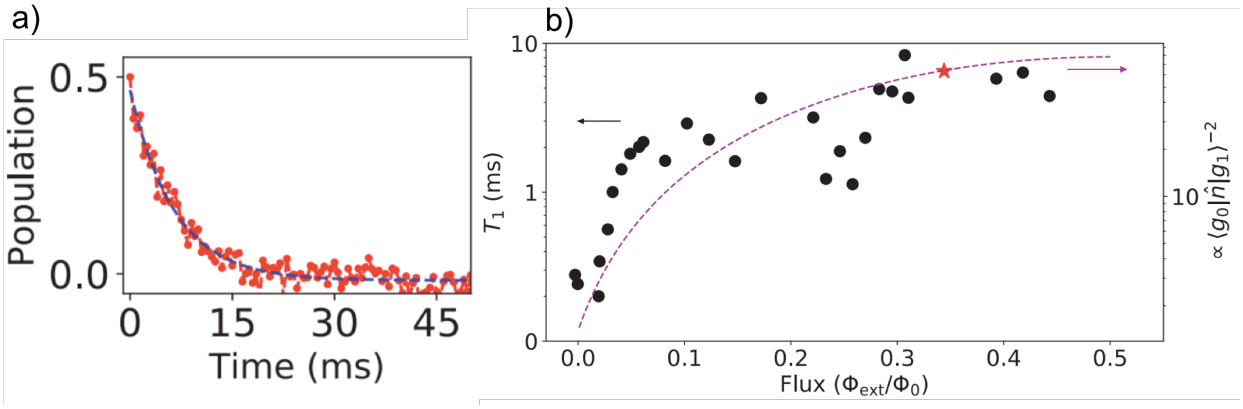

Figure 6.14: a) An example of a T_1 measurement carried out with a long Raman drive, and indicated by the red star in b. b) T_1 measurements of the heavy fluxonium over most of the flux quantum, with the purple dashed line indicated the inverse of the charge matrix elements squared. This indicates that the T_1 is limited by dielectric loss in the capacitor, in agreement with [11].

CHAPTER 7

QUBIT INVERSION: NEGATIVE TEMPERATURE ACTIVITY

7.1 Defining Negative Temperature

Temperature is something that we usually defined as a sense of hot or cold, and for most people is usually measured in either Celsius or Fahrenheit. For Celsius the temperature range is based on the freezing and boiling points of water, which depends on local pressure. Intuitively this relates to the amount of how much the particles are moving around. This notation of motion can be rigorously defined through the entropy of the system:

$$S = k \ln \Omega \tag{7.1}$$

Where Ω is the distribution of states. The more energy the particle has, the more states in it distribution. From this we are able to rigorously define the temperature of our system:

$$\frac{1}{T} = \frac{\partial S}{\partial E} \tag{7.2}$$

Where we now measure the system in Kelvin, where - if it were possible - particles would stop moving once the system reaching 0K. This, however, is forbidden from Heisenberg's uncertainty principle, so there will always be some zero-point energy fluctuations. This sense of temperature can become slightly more intuitive for a collection of non-interacting spin-$\frac{1}{2}$ particles. In such a system, the energy is given by:

$$E = \frac{\omega_s}{2} \sum_i \sigma_i \tag{7.3}$$

Where ω_s is the energy difference between the spin states, and σ_i represents the state of the i-th spin. When all of the particles are in the ground state, then we have the temperature is

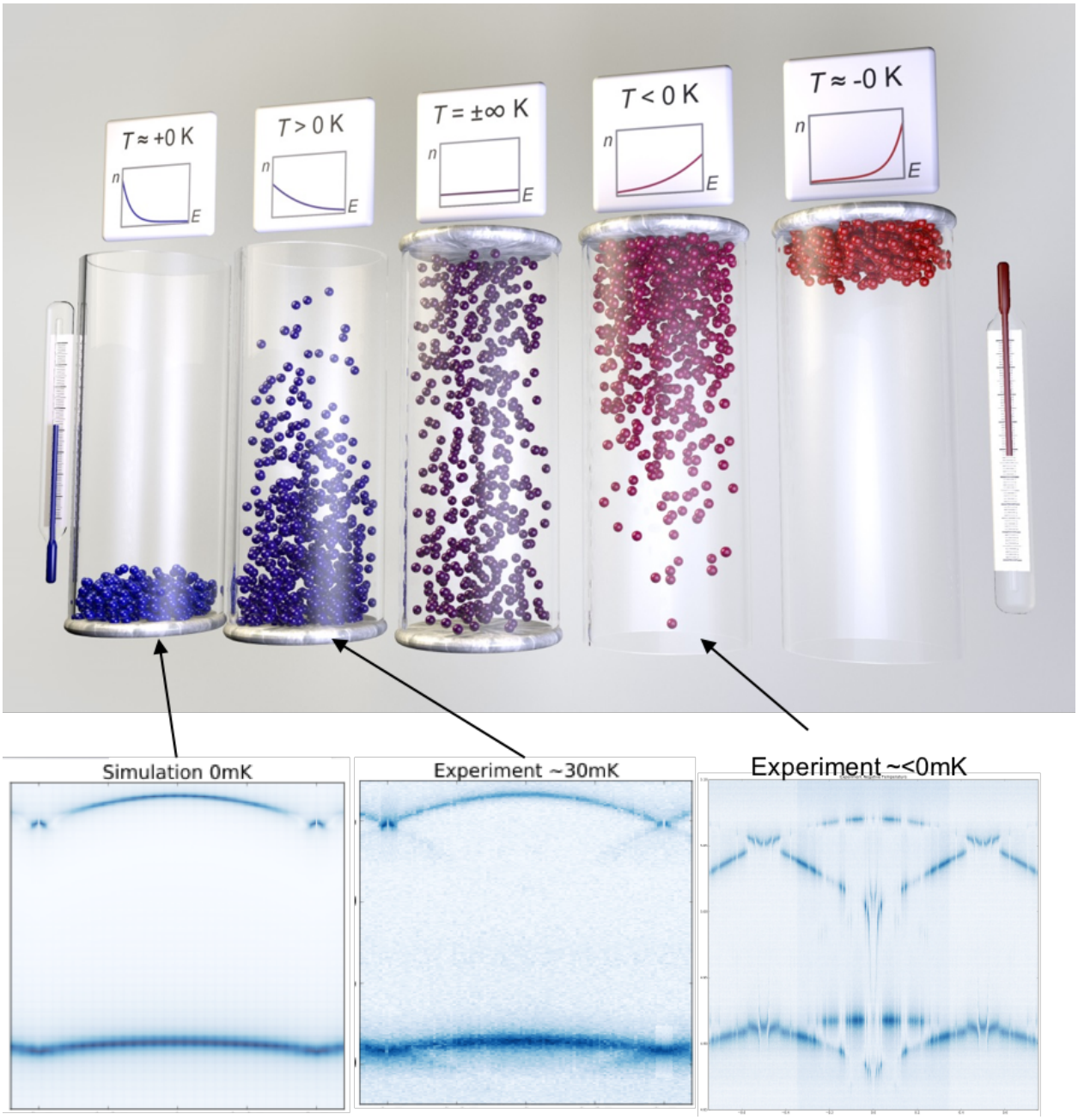

Figure 7.1: Info-graphic demonstrating the meaning of a negative temperature as well as a none-zero positive temperature, to better reveal what is discussed in the finite temperature

zero. An infinite temperature result in a random distribution of spin states, and when all of the particles are in the excited state we have that the system is in a negative temperature state. (see figure 7.1). So, in this respect, when a device is preferentially in an excited state of the system we can say that it is in a negative temperature state. It is in this way, that we have found that our heavy fluxonium went into a negative temperature state for varying periods of time. In particular, it went into a negative temperature state that was persistent for over a week, and can be seen in figure 7.3, and only went back to the typical ground state after trying several reset protocols. The exact cause of this negative temperature state has yet to be determined, and will require more experiments to completely rule out external sources. However, there is a considerable amount of behavior to this device's state that I would like to draw the reader's attention to now.

7.2 Thermal Population of Excited State vs Negative Temperature

One strong bit of evidence that the qubit truly went into a negative temperature state can be seen when we look towards the half-flux region, and understanding the difference between thermal excitation and negative temperature. As discussed in section 6.2, the capacitive shunt of our heavy fluxonium results in the primary energy transition ($|g_0\rangle \rightarrow |g_1\rangle$) going down to sub-MHz energy levels. At such low frequencies, the thermal bath - even inside our 20mK dilution fridge - becomes comparable to the qubit energy. As we move towards half-flux quantum, a combination of the long-lived nature of our $|g_1\rangle$ state and the thermal excitations, the device is thermal excited and switches to the $|g_1\rangle$ state around $\Phi_{\text{ext}} \sim 0.43\Phi_0$. This can be seen both in figure 6.5, where the lower plasmon branch $|g_1\rangle \rightarrow |e_1\rangle$ becomes bright, as well as in figure 7.4, where the resonator-like peak has avoided crossings associated with the qubit being in the $|g_1\rangle$ state. These features are the result of our system interacting with the thermal bath and are distinct from a 'negative' temperature state, which varies

over time and at frequencies well above kT. Below I will discuss some intricacies of these features as well the different durations of the negative temperature activity.

7.2.1 Flux-Dependent Qubit Inversion

Now that we have defined the meaning of negative temperature and clarified how this is different than the finite temperature population of the excited states, I would like to discuss two different sorts of negative temperature activity. The first of which is a negative temperature activity that seemingly depends on flux. In figure 6.3 a black star around $\Phi_{\text{ext}} \approx 0.6\Phi_0$ marks a moment when the resonator seems to shift, and the excited state of the device is occupied. This is an instance of what I would call a 'flux-dependent' negative temperature state. These brief periods of inversion would occur at seemingly specific flux values, but would vary in how often they occurred and happened many times throughout our measurements. To better characterize this qubit inversion, I made use of our ability to do fluorescent readout of the qubit state, which should help determine the effect of our drive for the qubit inversion.

Fluorescent Readout to Characterize Momentary Qubit Inversion

Fluorescent readout is a quantum non-demolition measurement method, whereby a quantum state is determined through cycling on a transition of interest. Commonly used in atomic and solid-state physics, this readout method will prove to be useful in characterizing our negative temperature state, as the same mechanism that determines the qubit inversion should also serve to reset the qubit into the excited state. This is particularly interesting as other groups studying the heavy fluxonium notice a negative temperature state when the qubit is driven at high powers [58], indicating that the drive may be the result of the qubit inversion. Specifically, we implement a method that is akin to the plasmon pumping discussed earlier, where before we cycled the $|g_0\rangle \rightarrow |e_0\rangle$ transition as a way to 'pump' our

qubit into the $|g_1\rangle$ state, and do subsequent T_1 measurements. However, we now turn to the other branch and cycle on the $|g_1\rangle \rightarrow |e_1\rangle$ transition. This will serve the purpose of measuring the qubit occupation in the $|g_1\rangle$ state, as well as a means to 'pump' our state into the global ground state $|g_1\rangle$. This fluorescent readout is done such that the driving component of the readout ensure the readout tone is 'pumping' the qubit into the ground and thereby rules out the possibility that drive of the readout as being the cause for the device to go into this negative temperature state. I perform this measurement for an hour in figure 7.2, where a simple NWA transmission measurement is done on the $|g_1\rangle \rightarrow |e_1\rangle$ frequency at a flux value of $\Phi_{\text{ext}} \sim 0.25\Phi_0$ for an hour. Each measurement takes approximately 15seconds, and is therefore only a measure of the average occupation of the qubit state. (This is why we do not measure discrete jumps in the device). This sort of negative temperature state was seen many times during qubit measurements, and - through discussions - was also seen by other heavy fluxonium groups (even those made with a NbTiN kinetic inductance for the superinductor).

7.3 Persistent Negative Temperature

7.3.1 Spectrum Overview

During the measurement of our device, we cycled the fridge and confirmed the device was still operational. Sometime later, measurement of the single tone spectra revealed a state of the device that preferred to occupy the $|g_1\rangle$ state, and remained this way for over a week! Plasmon pumping was attempted to put the device back into the universal ground state, but would only put the device into the $|g_0\rangle$ state while the pumping remained on! Instead, this persistent state was reset during a haphazard approaching, trying high powers, and ultimately going back to the ground state when the external flux was biased near zero flux and slowly moved back and forth across this value, 'pouring' the occupation into the

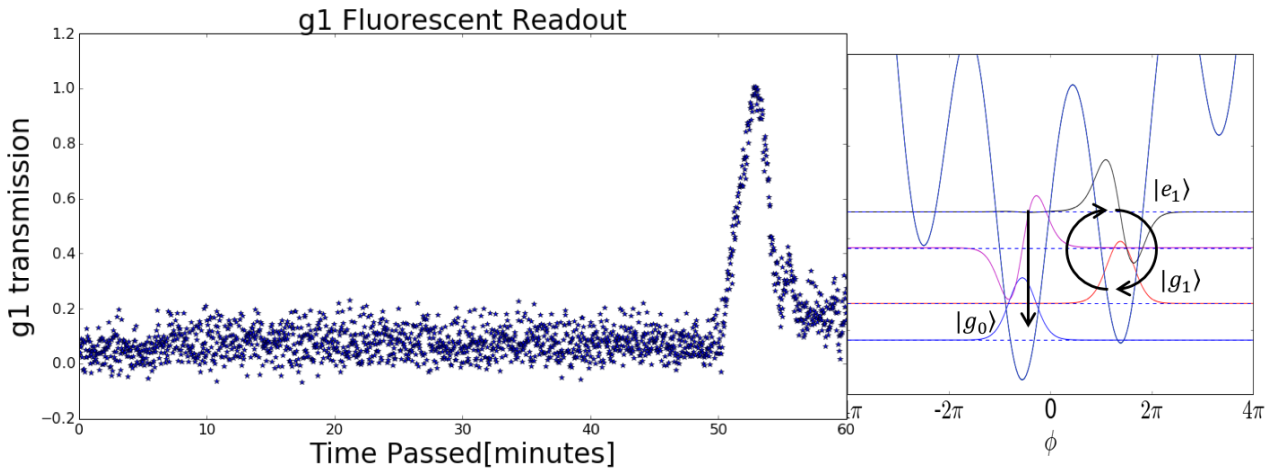

Figure 7.2: Fluorescent Readout of the fluxon state, and an observation of qubit inversion over roughly a 10-minute period. These qubit inversions occurred frequently in this device, and have also been observed by other groups with similar fluxonium devices. This plot is an example of what one of these inversions looked like, but is not necessarily what all of these inversions looked like. b) The readout scheme for plot a, demonstrating that this is also a measurement that pumps that qubit into the ground state. None-the-less the qubit took on a preferred excited state. c) Given the quantum nature of our energy levels, it should be the case that the qubit is either in $|g_0\rangle$ or $|g_1\rangle$. Therefore, the measured peak indicates that the qubit is spending varying amounts of time in the excited state, but does not tell us about the faster dynamics of this process.

$|g_0\rangle$ state. Due to the unknown cause of this persistent negative temperature state, further studies were not pursued to fully address why it arose and what reset protocol ultimately worked. None the less, there are a substantial number of interesting features that arose during this inversion that are worth taking note. It can be seen that during this persistent negative temperature state, the device would continue to 'invert' back to the $|g_0\rangle$, but would not remain there as one would expect, and these inversions has a rather strong symmetry in the spectrum about zero flux. This is particularly surprising as there was a substantial amount of inversion occurring, and is an indication that this inversion is systematic and not simply the result of noise. Furthermore, there were some flux points where the spectrum went bright at a point not associated with known devices energies (indicated by the black stars in figure 7.3.

7.3.2 Inverted Spectrum - Half Flux Features: Modeled and Not

Avoided Crossing Captured by current Hamiltonian model

If we turn our attention to the half-flux quantum region, we can see some interesting features. Particularly, around $\Phi_{\text{ext}} \sim 0.43\Phi_0$ (or, equivalently $\sim 0.57\Phi_0$), we have the $\omega_{g_0 g_1} \sim kT$, and the thermal bath consequently 'excites' the qubit into the global ground state $|g_0\rangle$ as determined by the fluorescent readout of the plasmon-like branch. Once the qubit is in the ground state, there is the onset of the composite avoided crossing arising from the following two transitions coming into resonance:

$$|g_0, 0_r\rangle \rightarrow |e_0, 0_r\rangle \tag{7.4}$$

with

$$|g_0, 0_r\rangle \rightarrow |g_1, 1_r\rangle \tag{7.5}$$

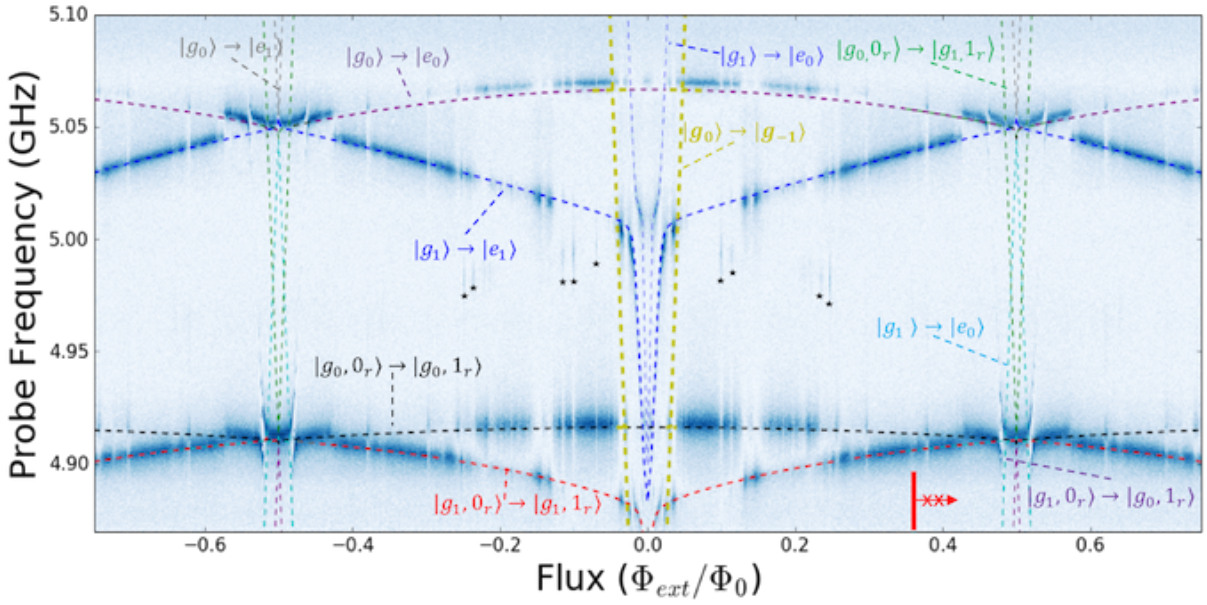

Figure 7.3: Single tone spectroscopy demonstrating qubit state inversion for varying time durations, and appearance of new avoided crossings. It also highlights very clearly the switching of preferred states throughout the measurements, with a surprising amount of symmetry. Black stars indicate occupation of a state that is not seen the Hamiltonian diagonalization(more easily viewed in an electronic version of this thesis). During these period the resonator blanks out from both the $|g_0, 1_r\rangle$ and $|g_1, 1_r\rangle$ states. Reasons for this inversion and avoided crossings are yet to be determined, though I give some speculative possibilities in the outlook. The redline with the arrow indicates that symmetry to the right is the result of reflecting data in the plot. The symmetry in the measurement is otherwise inherent in the measurement.

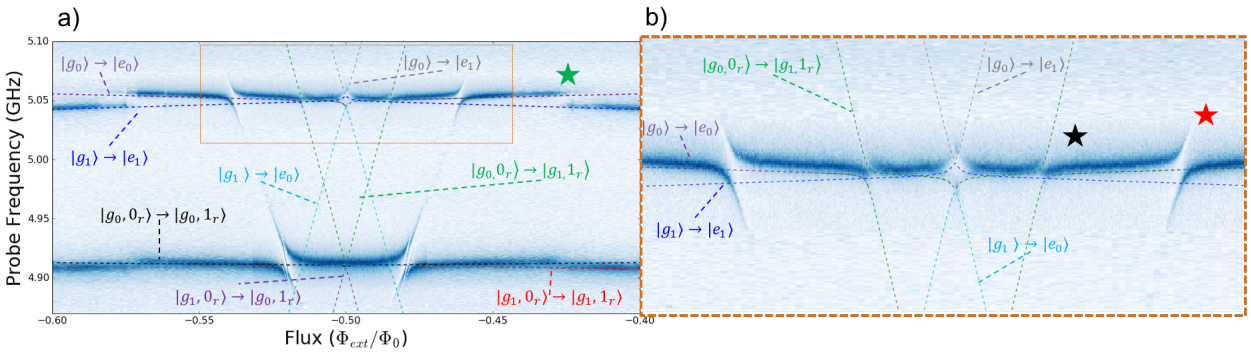

Figure 7.4: a) Single tone inverted spectroscopy near half flux quantum. I note that as we approach half flux quanta, the spectrum goes from being bright on the $|g_1\rangle \rightarrow |e_1\rangle$ branch to the $|g_0\rangle \rightarrow |e_0\rangle$. This is the opposite trend when the qubit is in the positive temperature state (which is captured by the steady state simulations). The green star indicates when the thermal bath 'excites' the qubit into the ground state $|g_0\rangle$. b) A zoom in near the plasmon-like features. The black star is to indicate the avoided crossing that is captured by our Hamiltonian, but was not very visible when the qubit was in the positive temperature state. The red star is to indicate an avoided crossing that is not captured by our model.

which indicates an avoided crossing between $|e_0, 0_r\rangle$ and $|g_1, 1_r\rangle$. This is a higher order avoided in which a photon and fluxon are exchanged for a plasmon. (indicated by the black star in figure 7.4b). However, the hybridized nature of our plasmon and resonator needs to be fully understood to appropriately understand this avoided crossing.

Unexplained Avoided Crossing: Reflected in Higher Energy Manifold

In addition to this avoided crossing that is explained by our current Hamiltonian model, there is a set of avoided crossings not yet captured. One is in the plasmon-like features in figure 7.4b, and the other is indicated by the red start in figure 7.6. The avoided crossing in the resonator, additionally, has an exquisite set of lines. Based on the fact that the $|g_0\rangle \rightarrow |e_0\rangle$ branch is bright, these avoided crossings should be associated with transitions arising from the ground state of the qubit, and not some other level in the qubit (or, possibly, coupling to some other system that is not accounted for in our model. Though this seems doubtful). Based on appearance, we can see in figure 7.4a that these avoided crossings are a connection

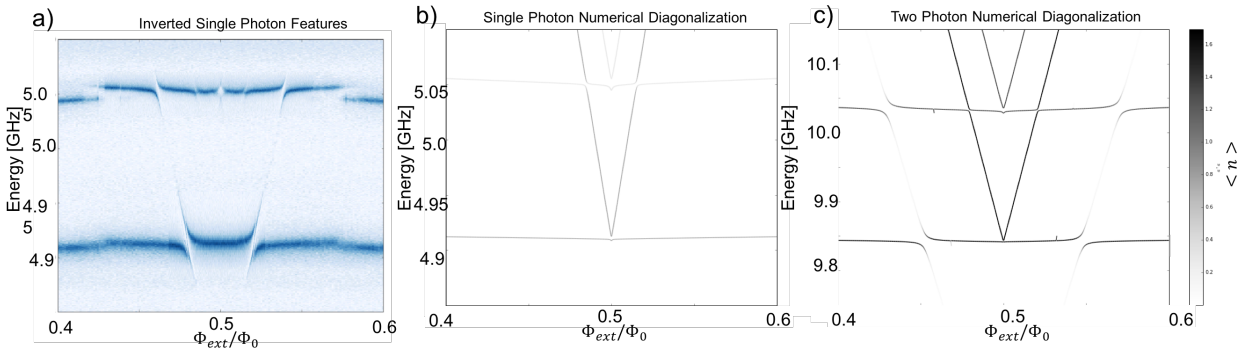

Figure 7.5: a) Experimental Data of Single Tone scan near half-flux quantum when the device is in the persistent negative temperature state. b) Expectation value of the photon number for the Eigen solution of the coupled Hamiltonian, showing a different energy spectrum than what was measured. c) Expectation value of a higher energy manifold for the Eigen solution of the coupled matrix. Showing the similar features of the inverted spectrum with this higher energy manifold. In figure 8.4, we see that the otherwise prevalent photon-assisted features line up in this area and may serve to excite us into this higher energy manifold.

of the plasmon-like and resonator-like features. Furthermore, when one looks at the higher energy manifold (see figure 7.5c) these unexplained avoided crossings are reflected in the 2-photon manifold. These features are indicative of a higher order coupling, and are rather suggestive of a 2-photon vacuum rabi splitting with our plasmon mode.

7.3.3 Inverted Spectrum - Zero Flux Features: Apparent Interactions Between γ-assisted transitions and $|g_1\rangle$-resonator

If we take a look near zero flux (figure 7.7), we note that there are a substantial amount of activity compared to the half-flux quantum region. More specifically, without the thermal excitation for a low frequency $\omega_{g_0 g_1}$, our qubit will not be stable like it was near half-flux quantum. In figure 7.7, I have overlaid the same photon assisted transitions that led to the blanking of our readout resonator in figure 6.7a or figure 6.11. It should not be surprising that these photon-assisted transitions would be important in explaining the activity of our device near zero flux given their omnipresence in the device otherwise. The exact nature of this behavior and precisely how these states interact with our qubit, however, is not yet

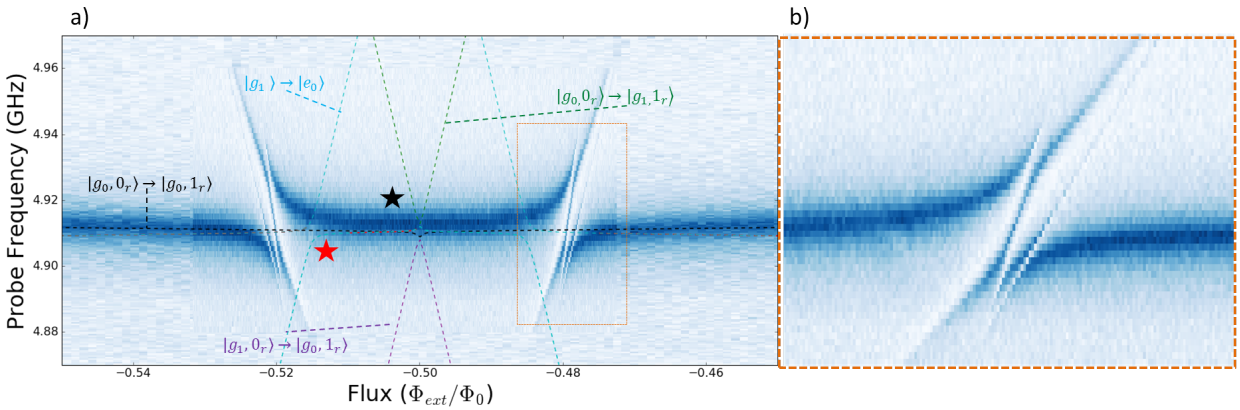

Figure 7.6: a) A zoom in of the resonator features near half flux quantum near half flux. The black star is to indicate the disappearance of the composite avoided crossings measured when the qubit is in the positive temperature states. The red star is to indicate the disappearance of the avoided crossing seen in the positive temperature state, and an onset of many different avoided crossings in its place. b) A zoom in of the unexplained avoided crossings, showing several intricate features which suggests the presence of several energies levels crossing in this vicinity.

understood and beyond the scope of this thesis.

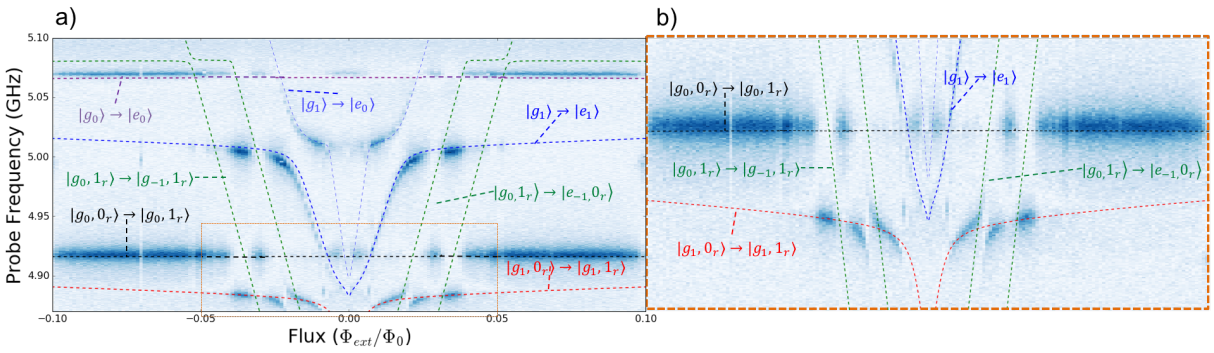

Figure 7.7: a)Single tone inverted spectroscopy near zero flux with the appropriately labeled transitions. b) A zoom in near the resonator-like features, capturing apparent avoided crossings, but not seen in the diagonalization of the Hamiltonian. The seeming avoided crossing corresponding to the resonator interacting with $|g_0, 1_r\rangle \rightarrow |g_{-1}, 1_r\rangle$ would serve to pump the qubit to the ground state, which is observed.

CHAPTER 8

OUTLOOK

8.1 New Gates

8.1.1 Tunable E_J and Fast flux

The method used to improve the coherence time of the device is good because it is relatively simple to accomplish. However, there is the added complication of getting fast gates with protection. Through implementing a double loop architecture (see figure 8.1a/d), one may be able to get the best of both words. Long T1s when the device is meant to serve as a storage, and fast gate times otherwise. One simple such approach would be to do an adiabatic change from a low E_j barrier height (see figure 8.1c), let the state rotate, and then tune the barrier back up to complete the gate, or there is the possibility to implement fast flux gates with our 2D architecture.

8.1.2 Coherent Photon Coupling of Fluxon transitions

In this device, we realize photon assisted transitions, which when a photon is present in the resonator, the forbidden fluxon states were greatly enhanced, as demonstrated by a transition from $|g_0\rangle$ t0 $|g_1\rangle$ at single photon powers, which is significantly lower than the powers needed to see the transition when driven without a photon present (see figure **??** for direct drive powers). Due to the low Q nature of our readout resonator, this does not make it possible to realize coherent gates with the use of a photon. One possible next generation of this device is to make a sort of 'fluxonium-resonator' molecule. In this situation, a high Q resonator plasmonically coupled to our fluxonium would comprise the 'fluxonium-resonator' molecule. This system would then be dispersively coupled to a low-Q readout resonator.

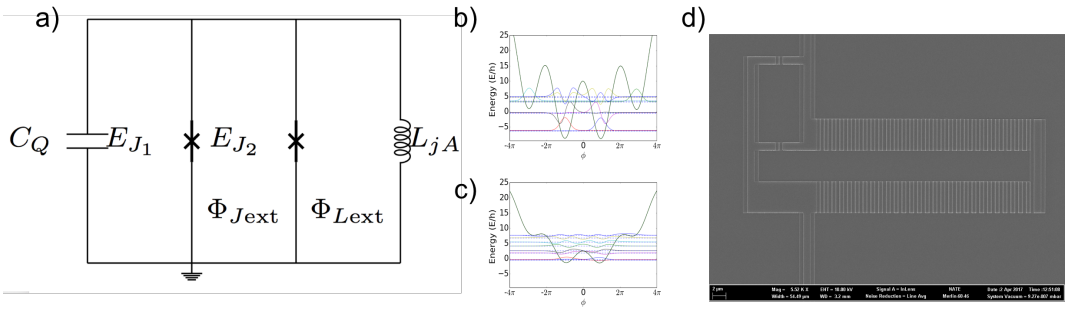

Figure 8.1: a) A circuit diagram of a heavy fluxonium circuit with both a tunable E_J and a tunable ϕ_L b/c) Ground state wavefunctions for two different E_J values which can be realized in-situ by implementing a tunable E_J loop d) An SEM image of a heavy fluxonium circuit fabricated using the Dolan bridge process with both a tunable E_J and ϕ_L with the center point offset from each other for the purpose of minimal crosstalk between each of the loops flux line.

8.2 Improving Coherence

8.2.1 Hyper-inductance fluxonium: The "Blochonium"

As we saw in the experimental results, the $T_2 \approx 500ns$ of the device was limited by flux noise. While it should be possible to improve the shield and noise sources of the device to improve this value slightly, ideally one would engineer the circuit to be immune to noise in the same way that we engineered the circuit's T_1 to be immune to noise. Given that we were limited by flux noise, an ideally way to improve the T_2 would be to create energy levels that tune less with flux. As we can see in figure 3.3d, this can be easily accomplished by further increasing the inductance of the circuit. However, the best way to achieve this increased inductance is unclear. This is due to the fact that the exact effect of chain modes on the Hamiltonian and when these modes will ruin the quantum states otherwise has yet to be experimentally verified. If these modes lead to minimal impact on the Hamiltonian, this it should be relatively easy to simply make a longer chain of junctions and get T_2s that are not limited by flux noise. An alternative approach will be to stack junctions on top of each other as discussed in the experimental design chapter, or possibly through the implementation

of high kinetic inductance samples. Furthermore, once this inductance reaches sufficiently large values, interesting comparisons between the 'blochonium' and the Cooper Pair box studied. As superconducting circuits get larger coherences times, the thermal bath will become increasingly important and provides the chance to study Maxwell's demon in the quantum limit.

8.2.2 0-π

Circuit Overview

Another possible path to make a circuit that is inherently immune to noise for both T_1 and T_2 is to use the 0-π circuit (figure 8.2). The Hamiltonian for this circuit is given by [54, 55]:

$$H = -2E_{C_J}\partial_\phi^2 - 2E_{C_\Sigma}\partial_\theta^2 - 2E_J\cos\theta\cos(\phi - \phi_{ext}/2) + E_L\phi^2 + 2E_J \tag{8.1}$$

where we have undergone a basis change from the nodes in figure 8.2a, following:

$$2\varphi_1 = \Sigma - \theta - \phi + \chi \tag{8.2}$$

$$2\varphi_2 = \Sigma + \theta + \phi + \chi \tag{8.3}$$

$$2\varphi_3 = \Sigma + \theta - \phi - \chi \tag{8.4}$$

$$2\varphi_4 = \Sigma - \theta + \phi - \chi \tag{8.5}$$

Though the $0-\pi$ circuit will be a very interesting circuit, both for its coherent protection for applications in quantum information [54, 55] and for interesting dualities of its dynamics to a Majorana Josephson junction [56], there are real large experimental challenges one must overcome in order to realize this exciting circuit. Below I elaborate on the challenges we have experienced thus far.

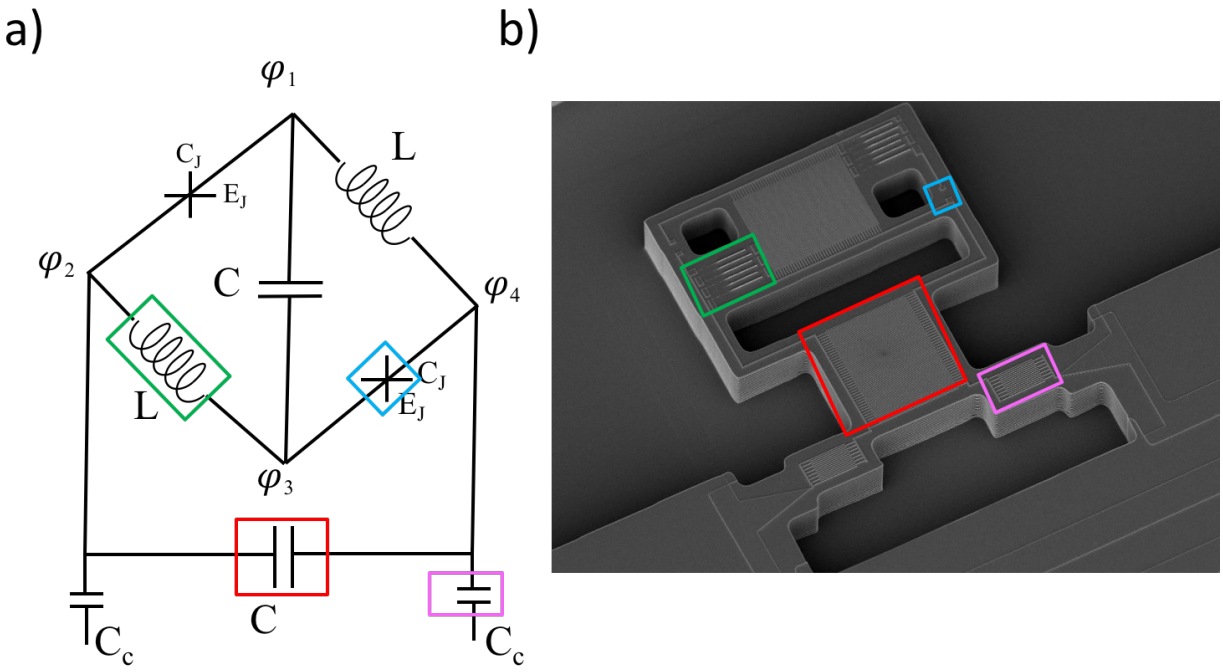

Figure 8.2: a)The circuit diagram for an asymmetrically coupled 0-π circuit. Colored boxes are to guide the eye for the fabrication image seen in b. b) An SEM image of process development for the 0-π circuit. In particular, this process was to determine the feasibility of using stacked junctions with a deep silicon etch to reduce the amount of stray capacitance contributing to C_J.

0-π Challenges: Capacitance Matrix

Part of the challenge in the circuit is that one must simultaneously realize very large capacitance and inductance values for the designed L and C (figure 8.2a), while simultaneously minimizing the undesired capacitances, in particular the capacitance across non-linear Josephson junctions. Intuitively this capacitance should be reduced in order to ensure that the effective mass in the ϕ degree of freedom is as small as possible in order to ensure there is a large amount of tunneling in this direction. Large tunneling in this direction will help spread the wavefunctions out over multiple wells and thereby make it less sensitive to flux (good for T_2.) In this sense, any amount of stray capacitance is a killer for the dynamics of the 0-Pi. As such, we seek to make the device as small as possible and thereby reduce

any source of stray capacitance. Furthermore, the specific design shown in figure 8.2 was the result of hard work with (and largely by) Abigail Shearrow [62], where she carefully analyzed the full capacitance matrix of the circuit. In this design, we implement the stack junction fabrication process discussed earlier, as well as a 75nm pitch interdigitated capacitor to simultaneously realize the needed large capacitance and inductance, with minimal stray terms. The essence of this analysis is to take the vector form of a capacitive network, $\vec{q} = C\vec{v}$, where C is the capacitance matrix precisely defined as:

$$C_{N\times N} = \begin{cases} C_{ii} = \sum_{j\neq i} C_{ij} \\ C_{ij} = -C_{ij} \end{cases} \quad \forall i,j \in I \cup S \tag{8.6}$$

Where C_{ij} is the direct capacitance between nodes i and j, and $\vec{q}$ represent the element with charges on nodes represented by the voltage vector $\vec{v}$. Following the method in [70], one can design the circuit to have minimum capacitance put across the small junction and the primary causes of the undesired capacitance can be determined through simulations. In this analysis, the nodes in the circuit can be divided into three sets: 'I' representing island nodes, 'J' is the set of nodes between a junction and a voltage source, and lastly 'S' is the set of voltage source nodes. In this situation, the charge on each node is then given by:

$$q_\alpha = \sum_{\beta\in I} C_{\alpha\beta} v_\beta + \sum_{i\in S} C_{\alpha i} v_i \tag{8.7}$$

In the case of our analysis we are just interested in the set of island nodes I, which then allows one to drop the extra term, use simulation software as a way to determine the appropriate capacitance matrix and invert the capacitance matrix to determine the effective E_{C_J}. One can find a very well written and detailed description of how to properly do this analysis at [62]. In Abigail's write up, she carefully goes through the appropriate form of the charge vector to get the desired charging energy, and the needed modifications to the original

charging matrix in order to invert it.

0-π Challenges: Asymmetric Coupling

Another difficult aspect of realizing the 0-π circuit is to avoid blending the different modes of the circuit. This is because we achieve our protected qubit through careful engineering of the modes and the resulting wavefunctions. As such, any mixing of the modes will inherently complicate the dynamics and make it more difficult for us to realize the protected states we are seeking. Disorder in the circuit (i.e. lack of symmetry in circuit energies) is one way in which this mode blending can occur, while another is through the 'asymmetric' coupling to our device, where one only couples to one of the capacitive (or inductive) elements, as was done in our initial circuit design (see figure 8.2). To see how this results in the blending of modes, let us first explore the case for symmetric capacitive coupling. In either case the Lagrangian for our 0-π circuit is given by:

$$L_{0-\pi} = C_J\dot{\phi}^2 + C_{\sum}\dot{\theta}^2 + C\dot{\zeta}^2 - U \tag{8.8}$$

And for the readout resonator:

$$L_r = \frac{1}{2}C_R\dot{\Phi}^2 + \frac{1}{2}E_L\Phi^2 \tag{8.9}$$

Now, if we use the symmetric coupling, the coupling Lagrangian is given by:

$$L^{\text{Sym}}_{\text{Coupling}} = \frac{1}{2}C_c\left[(\dot{\varphi}_1 - \dot{\varphi}_6)^2 + (\dot{\varphi}_3 - \dot{\varphi}_6)^2 + (\dot{\varphi}_2 - \dot{\varphi}_5)^2 + (\dot{\varphi}_4 - \dot{\varphi}_5)^2\right] \tag{8.10}$$

Which, after dropping a few terms that don't affect the circuit dynamics and changing to the appropriate basis gives:

$$L_c = \left(C_J + \frac{1}{2}C_c\right)\dot{\phi}^2 + \left(C_{\sum} + \frac{1}{2}C_c\right)\dot{\theta}^2 + \left(C + \frac{1}{2}C_c\right)\dot{\zeta}^2 - U - \frac{1}{2}C_c\dot{\phi}\dot{\phi_-} - \sum \dot{\phi_+} + \dot{\phi_-}^2 + \dot{\phi_+}^2 \tag{8.11}$$

Where $\phi_5 = \frac{1}{2}(\phi_+ + \phi_-)$ and $\phi_6 = \frac{1}{2}(\phi_+ - \phi_-)$. In the case of the asymmetric coupling, however, following a similar procedure we get:

$$L_c^{asym} = \frac{1}{2}C_c\left(\frac{1}{2}\dot{\Sigma}^2 + \dot{\phi}^2 + \dot{\Theta}^2 + \dot{\zeta}^2 + \dot{\Sigma}\dot{\phi} + \dot{\theta}\dot{\zeta} - \dot{\Sigma}\dot{\phi}_+ - \dot{\theta}\dot{\phi}_- - \dot{\phi}\dot{\phi}_+\dot{\zeta}\dot{\phi}_- + \dot{\phi}_-^2 + \dot{\phi}_+^2\right) \tag{8.12}$$

Where we can see now that the modes have all blended together. Our approach was to simplify the fabrication of the device (even though it is still a challenging fabrication in our 'simplified' version), and avoid the use of crossovers for symmetric coupling.

8.3 Weak-link Junction

8.3.1 Brief Description

A Josephson junction is effectively a current constriction point in which quantum tunnel effects become appreciable and important. A similar idea can be achieved by using a 'weak-link bridge' in which current flow become difficult due to the fact that the bridge width is smaller than the coherence length of the metal and the bridge length is longer than the London length. Under these conditions, quantum tunneling effects can begin to occur, however their phase relation is no longer the simple phase relation of the SIS-Josephson junction.

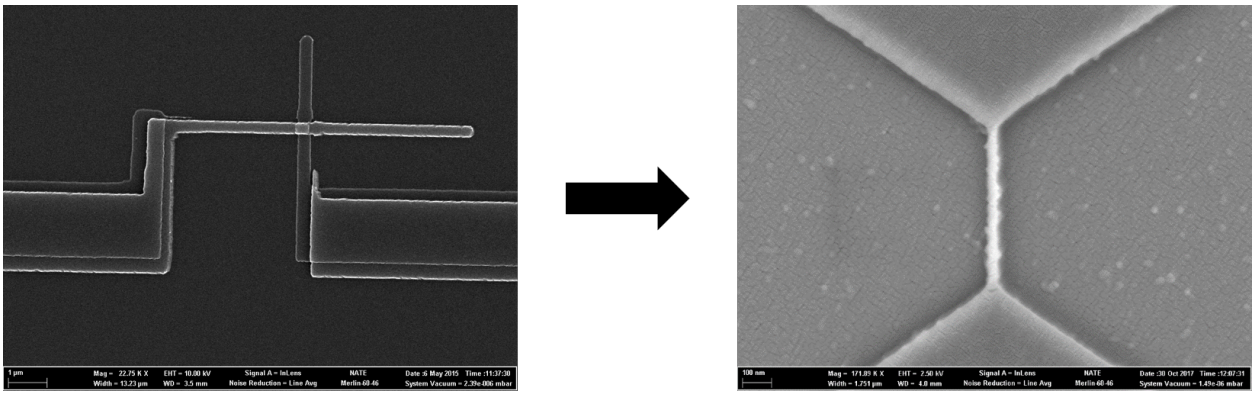

Figure 8.3: By using a highly disordered superconductor, such as Titanium Nitride, a SIS-Josephson junction(left) can be replaced by a weak-link bridge (right). This realization of a tunable non-linearity provides to opportunity to experimentally explore difficult BCS theories for such systems. Furthermore, the distributed nature of the bridge allows for the opportunity to place other interesting quantum systems nearby and couple to different degrees of freedom

8.3.2 Weak-Link fluxonium to Couple to Other systems

An interesting application of such a weak-link junction would be to use the magnetic field associated with the weak-link as a way to couple to other systems. If coherent quantum phase slips can exist across a TiN weak-link, this weak-link can replace the small phase-slip junction in the heavy fluxonium circuit (similar to how the group at Princeton used NbTiN as a way to replace the superinductance Josephson junction chain) and may prove to be a means by which one can engineer a heavy fluxonium circuit that can then couple to nearby magnetic systems. Given the demonstrated coherence of these artificial atoms, such a system could serve to be a highly sensitive to its magnetic environment. More specifically, the magnetic field associated with the weak-link could serve as a means to create an artificial spin-orbit coupling which may allow for the realization of Majorana modes, which can then be readout through the heavy fluxonium [57].

8.4 Light/Matter Engineering

8.4.1 Ultra-Strong Coupling

Earlier we saw that the dimensionless coupling, which can help us characterize the magnitude of the dipole coupling, in the case of capacitive coupling is given by:

$$\frac{g}{\omega_r} = \beta \sqrt{\frac{Z_r e^2}{2\hbar}}$$

Where Z_r is the impedance of the readout resonator. If one were to seek the largest coupling value possible, maximizing the voltage division aspect of the circuit results in a situation where $\beta = 1$ and the coupling is primary determined by the impedance of our readout resonator. Rewriting this equation in a suggestive form where we can compare coupling realized in cavity QED:

$$\frac{g}{\omega_r} = \zeta \sqrt{\frac{2\alpha}{n}} \left(\frac{\mu_r}{\epsilon_r}\right)^{1/4}$$

Where μ_r and ϵ_r are dependent on the material being used. In the case of a high impedance readout resonator, of $Z_r \approx 10\text{k}\Omega$, (realizable with either a thin TiN film, or a resonator made from a chain of large Josephson junction) we can exceed the vacuum impedance and study light/matter interactions not achievable in cavity QED [63, 12].

8.5 What is causing negative temperature and avoided crossings

8.5.1 Avoided Crossings Resemble a higher 2-photon manifold

During the negative persistent temperature state, we observed the appearance of avoided crossings not capture directly in the Hamiltonian model of our device. Naively one may think they are associated with transitions from the $|g_1\rangle$ state, however the incorrect branch is bright for this to be the case and instead these avoided crossing should be related to features

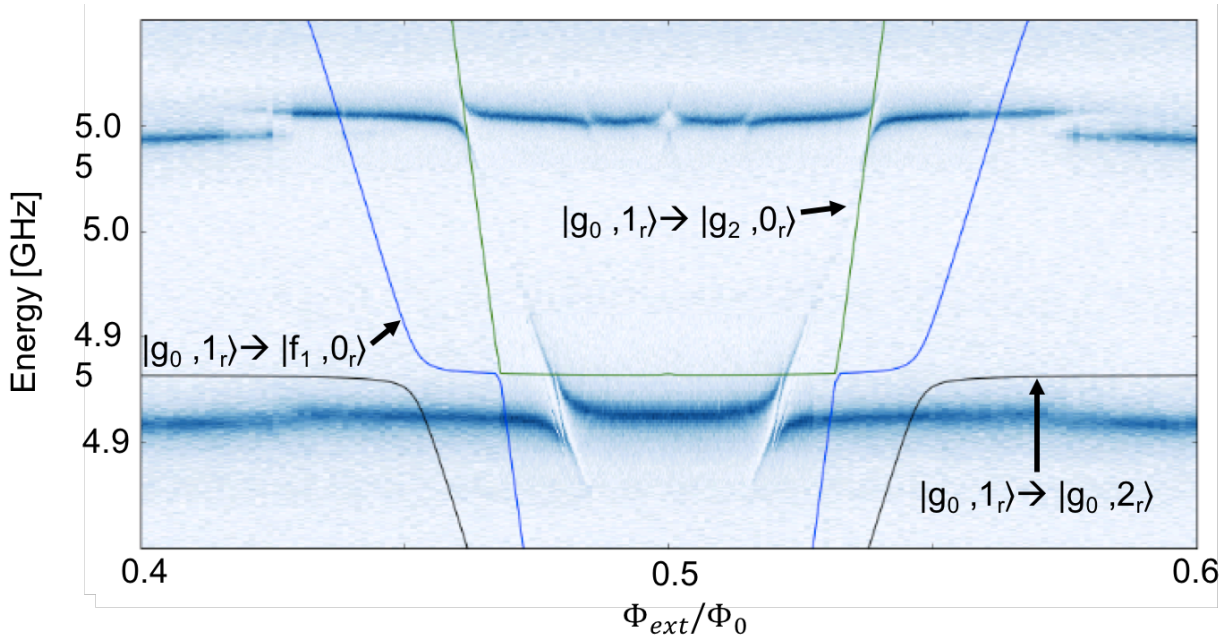

Figure 8.4: Overlay of the photon assisted features that played a large role in various qubit activity. In particular, the transition associated with a shift of two fluxoid numbers $|g_2, 0_r\rangle$ in connection with the similar features seen in figure 7.5c, along with the proximity of these photon assisted transitions is suggestive of a need for higher order correction in our sample.

with the device in the $|g_0\rangle$ state. As shown earlier in figure refNegTempTwoPhoton, these features closely reflect a higher 2-photon manifold, which seems suggestive that this behavior is inherent to the physics of the device itself and may be a sign of a 2-photon coupling [13]. A further indication of this 2-photon coupling would be gained by the detection of correlated photon emission. In figure 8.4, I point how that the photon assisted transitions, which caused resonator blanking in figure **??**, are in close proximity to the single-photon spectrum and may serve as a way to couple the device to the 2-photon manifold.

8.5.2 Negative Temperature Activity: Interesting interplay between qubit and thermal bath

One aspect of this device that we have not yet explained is the root cause of the various negative temperature activities. In order to explain these features with scientific rigor, we

must do so by designing careful experiments, and reproducing the various features. To this end, I would like to make specific mention of what was reproducible and what was not. However, I will state upfront that I can only offer speculative ideas and no definitive answers.

The momentary qubit inversion was a feature that occurred multiple times in the measurement of this device and did not correspond with a raise in the fridge's base temperature. However, the temperature of higher stages and the lines themselves were not well characterized and, in principle, could have played a role in the behavior. Furthermore, it is interesting to note that through conversations with other groups, I have learned that others have also seen these momentary qubit inversions (like that shown in figure 7.2 or 6.3a around $0.65\Phi_0$. This momentary inversion appeared with a regular occurrence), indicating this feature appears to be a general result of heavy fluxonia. A possible explanation for such features could be that the larger capacitor pads that are present in the heavy fluxonium will have flux vortices appear, which can move around over time, and will do so randomly. If such a vortex was present it could, in principle, shift the flux quantum of the device by $\sim \Phi_0$, which would result in a seeming negative temperature state. It is also interesting to note that in a talk by Long B Nguyen [58], demonstrates that at high cavity powers this negative temperature state can appear. It is interesting that high power would put the qubit into such a state, though I do not believe that this is the reason that it is always seen, based on the fluorescent readout scheme used in 7.2, as this should serve as a way to pump the qubit into the 'global ground state', $|g_0\rangle$, indicating something more than only the drive component on the qubit is causing the inversion. The week-long persistent negative temperature state, however, was not a feature that we reproduced, and it is unclear what is its root cause. I would argue though, that the high level of symmetry in the behavior about zero flux, and the onset of avoided crossings (explained above), along with the momentary inversion seen by multiple groups with the heavy fluxonium, all seem to indicate that this inversion may be the result of physics inherent to the circuit. I would like to elaborate on the features seen in the avoided

crossings and how these, to me, indicate that this inversion is more than just noise.

A unique property of this specific heavy fluxonium device is the plasmonic coupling whereby our plasmon transitions are always non-dispersively coupled to the readout mode (this is what makes it possible to perform fluorescent readout). In particular, our ability to directly see plasmon transitions allows us to see an onset of a composite avoided transition involving both a fluxon and a photon($|g_0, 0_r\rangle \rightarrow |g_1, 1_r\rangle$ having an avoided crossing with $|g_0, 0_r\rangle \rightarrow |e_0, 0_r\rangle$, seen in figure 7.4). It is interesting that the Hamiltonian captures this avoided crossing, but it is not seen when the device is in the 'normal', finite temperature, state as the thermal baths excites it to $|g_1\rangle$.

We can see in figure 7.4a that the qubit at a flux value of $\phi_{\text{ext}} \approx 0.575\Phi_0$ or $\phi_{\text{ext}} \approx 0.435\Phi_0$ that the qubit switches from the $|g_1\rangle \rightarrow |e_1\rangle$ branch to the $|g_0\rangle \rightarrow |e_0\rangle$, which would explain why we can still see the composite transition as shown above. Furthermore, in figure 6.5, we see the opposite. The qubit switches from the $|g_0\rangle \rightarrow |e_0\rangle$ branch to the $|g_1\rangle \rightarrow |e_1\rangle$, which would then explain why we don't see the avoided crossing when the device is in the 'normal' state. It would also explain why we see the avoided crossings in the resonator associated with the transition $|g_1, 0_r\rangle$

So, it is understood why the avoided crossing appears in the negative temperature state, and not otherwise. In the case in which the device is in the normal state, this can be easily understood by the fact the thermal excitations will result in an increased occupation in the excited state as the qubit goes towards half-flux quantum where its frequency becomes much smaller than kT. At around $\Phi_{\text{ext}} \sim 0.43\Phi_0$, the ground state transition $|g_0\rangle \rightarrow |g_1\rangle$ is at 650MHz which is comparable to the thermal bath energy of kT$\sim$625MHz for our 30mK base stage. This explains why we switch the $|g_1\rangle \rightarrow |e_1\rangle$ branch as seen in figure 6.5, and the appearance of the avoided crossings associated with the qubit being in the $|g_1\rangle$ seen in figure 6.6. However, what is curious is the situation when the qubit is in the negative temperature state. In such a case, we find that the qubit switches to the opposite $|g_0\rangle \rightarrow |e_0\rangle$,

which explains why we see the onset of the composite avoided crossings associated with $|g_0\rangle$, but the fact that the thermal bath would drive the qubit from $|g_1\rangle$ to $|g_0\rangle$, seems to be counterintuitive. This result would be indicative of an interesting interplay of our quantum system and the thermal bath, which should become more relevant with highly coherent devices [59, 60]. It would be very interesting if this persistent negative temperature state could be reproduced and better understood.

CHAPTER 9

APPENDIX

9.1 'Medium' Power Scans

As one can see in the figure 6.7a there is a moment near zero flux quantum where our resonator blanks out, (indicated by the white star) creating a vertical strip in our pulsed two-tone scan. As explained earlier, this is the result of a photon assisted transition coming into resonance with our readout resonator and the specific transition in consideration consequently pumps us into $|g_1\rangle$, and blanks to resonator. These features depend heavily on the read power of the cavity, with many more features appearing when we go into the multi-photon read power regime. To elucidate this fact a bit more, I present a single tone scan at slightly higher powers

9.2 Code

Some screens shots of the python code used to get the values for resonator Hybridization and charge matrix elements.

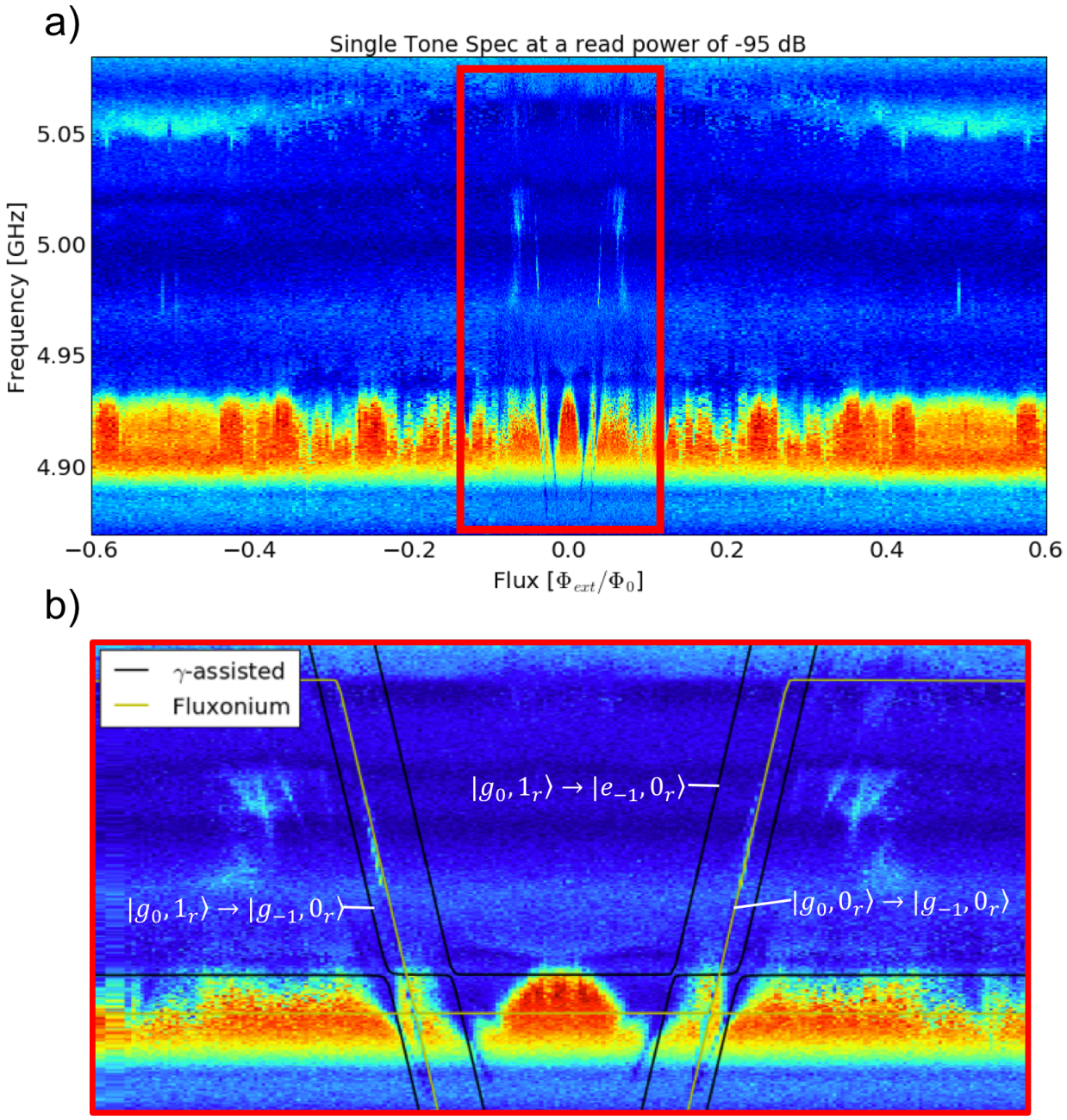

Figure 9.1: a) A medium power flux scan demonstrating the blanking of our resonator. b) A zoom in of the scan in b showing the photon assisted transitions causing blanking in the resonator (this is the feature that causes the vertical stripes in figure 6.7. Additionally, we can see that the fluxon transition corresponding to $|g_0, 0_r\rangle \rightarrow |g_{-1}, 0_r\rangle$ directly in single tone when driving at higher enough powers.

Fluxonium qubit

$$H_{\mathrm{fl}} = -4E_C\partial_\phi^2 - E_J\cos(\phi - \varphi_{\mathrm{ext}}) + \tfrac{1}{2}E_L\phi^2$$

In [3]:
```
fluxonium = qubit.Fluxonium(
    EJ = 8.11,
    EC = 0.456,
    EL = 0.243,
    flux = 0.0,
    cutoff = 110,
    truncated_dim = 12
)
```

In [4]:
```
fluxonium
```

Out[4]:
```
fluxonium -- PARAMETERS -------
EC      : 0.456
EJ      : 8.11
EL      : 0.243
cutoff  : 110
flux    : 0.0
truncated_dim   : 12
Hilbert space dimension : 110
```

In [6]:
```
figure(figsize=(7.5,7.5))
flux_list = linspace(-0.61,0.61,400)
plt.title('$E_C$ = 0.5GHz',fontsize=20)
plt.xlabel('test',fontsize=20)
plt.ylabel('energy',fontsize=20)
fluxonium.plot_evals_vs_paramvals('flux', flux_list, evals_count=10, subtract_ground=True,yrange=[0.4,10.7])
```

```
[====================] 100% Done.
```

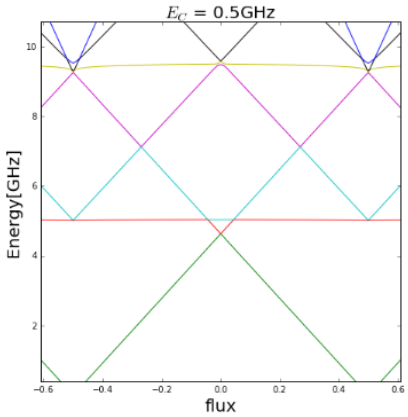

Figure 9.2: Code for Bare fluxonium. Using the python library developed by the Koch group at Northwestern.

```
In [8]: fluxonium.flux=0.00
        figure(figsize=(3,7.5))
        fluxonium.plot_wavefunction(esys=None,phi_range=(-4*3.14,4*3.14), which=(0,1,2,3,4,5,6,7), mode='real')
        ylim(-10.5,20)
        xlim(-1,3)
        ylabel('Energy (E/h) ',fontsize=35)
        xlabel('$\phi$',fontsize=35)
        plt.tick_params(labelsize=34)
        plt.xticks(arange(-4*pi,5*pi,2*pi),(['-$4\pi$','-$2\pi$','0','$2\pi$','$4\pi$']))

Out[8]: ([<matplotlib.axis.XTick at 0x3daca90>,
          <matplotlib.axis.XTick at 0xad7c3c8>,
          <matplotlib.axis.XTick at 0x87a7588>,
          <matplotlib.axis.XTick at 0x8756c88>,
          <matplotlib.axis.XTick at 0x8756208>],
         <a list of 5 Text xticklabel objects>)

        <matplotlib.figure.Figure at 0xb3bba20>
```

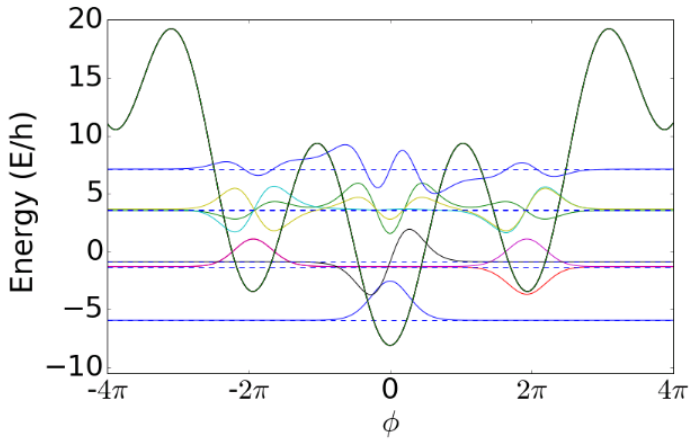

Figure 9.3: Code for Bare fluxonium wavefunction. Using the python library developed by the Koch group at Northwestern. Important for determining energy level labeling.

In [5]:
```
# Set up the components / subspaces of our Hilbert space

resonator = qubit.Oscillator(
    omega = 4.95,
    truncated_dim=3
)

fluxonium = qubit.Fluxonium(
    EJ = 8.11,
    EC = 0.456,
    EL = 0.243,
    flux = 0.0,
    cutoff = 110,
    truncated_dim = 12
)


hilbertspc = qubit.HilbertSpace([fluxonium, resonator])


# Get resonator Hamiltonian (full product Hilbert space)
h_res = hilbertspc.diag_hamiltonian(resonator)
```

In [6]:
```
hilbertspc
```

Out[6]:
```
====== HILBERT SPACE OBJECT ======
subsystem_list  : [fluxonium -- PARAMETERS -------
EC      : 0.456
EJ      : 8.11
EL      : 0.243
cutoff  : 110
flux    : 0.0
truncated_dim   : 12
Hilbert space dimension : 110, Oscillator -- PARAMETERS -------
truncated_dim   : 3
omega   : 4.95]

dimension       : 36

subsystem_count : 2

subsystem_dims  : [12, 3]
```

In [53]:
```
g = 0.076  # coupling resonator-fluxonium (without charge matrix elements)

hbd = hilbertspc.hubbard_operator
a = hilbertspc.annihilate(resonator)

dim1 = fluxonium.truncated_dim
# Spectrum when varying flux
# Set up Hamiltonian:

def hamiltonian(flux):
    fluxonium.flux = flux

    esys = fluxonium.eigensys(evals_count=dim1)
    gmat = g * fluxonium.matrixelement_table('n_operator', esys=esys, evals_count=dim1)   # coupling constants

    h_fl = hilbertspc.diag_hamiltonian(fluxonium)
    v = sum([gmat[j][k] * hbd(j,k,fluxonium) for j in range(dim1) for k in range(dim1)])

    return (h_fl + h_res + v*(a + a.dag()))
```

Specify initial state for transition in terms of *bare fluxonium and resonator states*

This is useful for understanding nature of lines in absorption/emission spectra.

In [54]:
```
flux_list = np.linspace(0.1, -0.11, 200)
specdata = hilbertspc.get_spectrum_vs_paramvals(hamiltonian, flux_list, evals_count=15, get_eigenstates=True, filename='m')
```

```
[====================] 100% Done.
```

In [55]:
```
spec_f0r0 = hilbertspc.absorption_spectrum(specdata, ((fluxonium, 0), (resonator, 0)), initial_as_bare=True)
spec_f1r0 = hilbertspc.absorption_spectrum(specdata, ((fluxonium, 1), (resonator, 0)), initial_as_bare=True)
spec_f0r1 = hilbertspc.absorption_spectrum(specdata, ((fluxonium, 0), (resonator, 1)), initial_as_bare=True)
spec_f2r0 = hilbertspc.absorption_spectrum(specdata, ((fluxonium, 2), (resonator, 0)), initial_as_bare=True)
```

```
[====================] 100% Done.

[====================] 100% Done.

[====================] 100% Done.

[====================] 100% Done.
```

Figure 9.4: Code for (linear) capacitive coupling fluxonium to a readout resonator and determining the uncoupled transitions of interest. Photon assisted transitions correspond to the braket when "(resonator,1)" is present.

```
In [29]: #Obtaining data, in this case eigenvalues and eigenstates
         ev_no = 15
         fluxval_count =200
         flux_list = np.linspace(-0.6, -0.4, fluxval_count)
         specdata = hilbertspc.get_spectrum_vs_paramvals(hamiltonian, flux_list, evals_count=ev_no, get_eigenstates=True)
         # specdata1 = hilbertspc.absorption_spectrum(specdata, ((fluxonium, 0), (resonator, 1)), initial_as_bare=True)

         [====================] 100% Done.

In [30]: absorptiondata = hilbertspc.absorption_spectrum(specdata, 0)

         [====================] 100% Done.

In [31]: n_res = a.dag()*a

         adag_a_data = np.empty((fluxval_count, ev_no), dtype=np.complex_)
         for fluxval_index in range(fluxval_count):
             for state_index in range(ev_no):
                 adag_a_data[fluxval_index][state_index] = qubit.matrix_element(specdata.state_table[fluxval_index][state_index],
                                                                                n_res,
                                                                                specdata.state_table[fluxval_index][state_index])

In [32]: plot.spectrum_with_matrixelement(absorptiondata, np.abs(adag_a_data), param_name='flux', energy_name='Energy[GHz]', matrixelement
                                          colormap='Greys',y_range=[4.85,5.1])
```

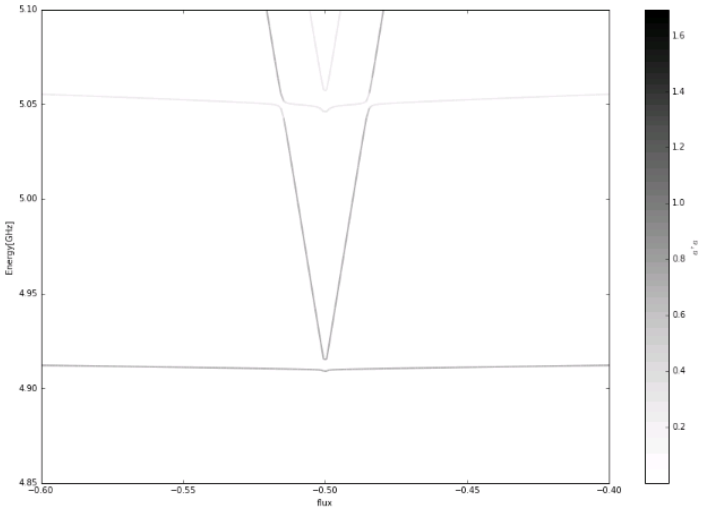

Figure 9.5: Code used to determine the number expectation for different transition of interest. Important for identifying composite transitions

In [33]:
```
fdim = fluxonium.truncated_dim

charge_op_data = np.empty((fluxval_count, ev_no), dtype=np.complex_)

for fluxval_index, flux in enumerate(flux_list):
    fluxonium.flux = flux
    esys = fluxonium.eigensys(evals_count=fdim)
    n_mat = fluxonium.matrixelement_table('n_operator', esys=esys, evals_count=fdim)   # coupling constants
    v = sum([n_mat[j][k] * hbd(j,k,fluxonium) for j in range(fdim) for k in range(fdim)])
    for state_index in range(ev_no):
        charge_op_data[fluxval_index][state_index] = qubit.matrix_element(specdata.state_table[fluxval_index][0],
                                                                          v,
                                                                          specdata.state_table[fluxval_index][state_index])
```

In [36]:
```
plot.spectrum_with_matrixelement(absorptiondata, np.abs(charge_op_data), param_name='flux', energy_name='energy', matrixelement_n
                                 colormap='Greys',y_range=[4.85,5.1])
```

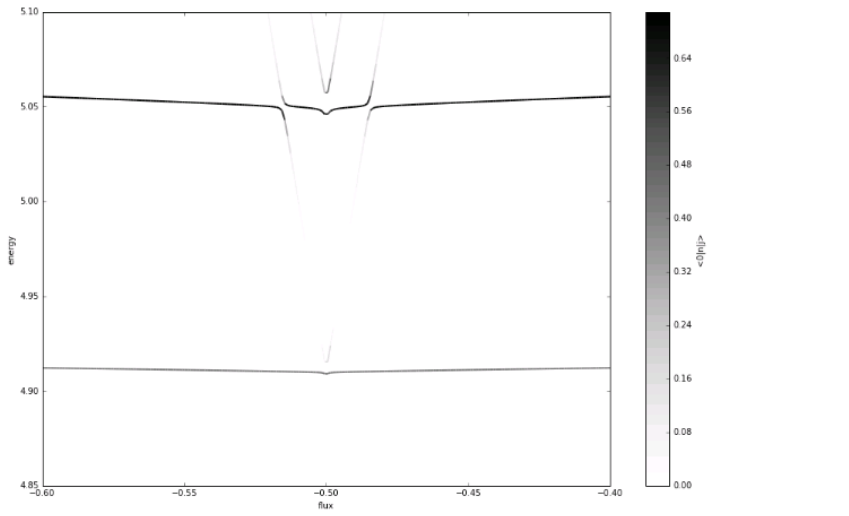

Figure 9.6: Code used to determine the charge matrix for different transitions of interest. Important for identifying composite transitions

REFERENCES

[1] Bouchendira, Rym, Pierre Clad, Sada Guellati-Khlifa, Franois Nez, and Franois Biraben. "New determination of the fine structure constant and test of the quantum electrodynamics." Physical Review Letters 106, no. 8 (2011): 080801.

[2] Macklin, Chris, K. OBrien, D. Hover, M. E. Schwartz, V. Bolkhovsky, X. Zhang, W. D. Oliver, and I. Siddiqi. "A nearquantum-limited Josephson traveling-wave parametric amplifier." Science 350, no. 6258 (2015): 307-310.

[3] Martinis, John M., Michel H. Devoret, and John Clarke. "Experimental tests for the quantum behavior of a macroscopic degree of freedom: The phase difference across a Josephson junction." Physical Review B 35, no. 10 (1987): 4682.

[4] Martinis, John M., S. Nam, J. Aumentado, and C. Urbina. "Rabi oscillations in a large Josephson-junction qubit." Physical review letters 89, no. 11 (2002): 117901.

[5] Wallraff, Andreas, David I. Schuster, Alexandre Blais, L. Frunzio, R-S. Huang, J. Majer, S. Kumar, Steven M. Girvin, and Robert J. Schoelkopf. "Strong coupling of a single photon to a superconducting qubit using circuit quantum electrodynamics." Nature 431, no. 7005 (2004): 162.

[6] Cedergren, Karin, Roger Ackroyd, Sergey Kafanov, Nicolas Vogt, Alexander Shnirman, and Timothy Duty. "Insulating Josephson Junction Chains as Pinned Luttinger Liquids." Physical review letters 119, no. 16 (2017): 167701.

[7] Schuster, David Isaac. Circuit quantum electrodynamics. Yale University, 2007.

[8] Bishop, Lev S. "Circuit quantum electrodynamics." arXiv preprint arXiv:1007.3520 (2010).

[9] Devoret, Michel H., and Robert J. Schoelkopf. "Superconducting circuits for quantum information: an outlook." Science 339, no. 6124 (2013): 1169-1174.

[10] Vool, Uri. "Engineering synthetic quantum operations." PhD diss., Yale University, 2017.

[11] Lin, Yen-Hsiang, Long B. Nguyen, Nicholas Grabon, Jonathan San Miguel, Natalya Pankratova, and Vladimir E. Manucharyan. "Protecting a superconducting qubit from energy decay by selection rule engineering." arXiv preprint arXiv:1705.07873 (2017).

[12] Kuzmin, Roman, Raymond Mencia, Nicholas Grabon, Nitish Mehta, Yen-Hsiang Lin, and Vladimir E. Manucharyan. "Quantum electrodynamics of a superconductor-insulator phase transition." arXiv preprint arXiv:1805.07379 (2018).

[13] Zhu, Guanyu, David G. Ferguson, Vladimir E. Manucharyan, and Jens Koch. "Circuit QED with fluxonium qubits: Theory of the dispersive regime." Physical Review B 87, no. 2 (2013): 024510.

[14] Earnest, Nathan, Srivatsan Chakram, Yao Lu, Nicholas Irons, Ravi K. Naik, Nelson Leung, L. Ocola et al. "Realization of a System with Metastable States of a Capacitively Shunted fluxonium." Physical review letters 120, no. 15 (2018): 150504.

[15] Manucharyan, Vladimir E., Jens Koch, Leonid I. Glazman, and Michel H. Devoret. "fluxonium: Single cooper-pair circuit free of charge offsets." Science 326, no. 5949 (2009): 113-116.

[16] Nguyen, Long, Yen-Hsiang Lin, Nicholas Grabon, Raymond Mencia, Aaron Somoroff, and Vladimir Manucharyan. "High-coherence fluxonium qubit." Bulletin of the American Physical Society (2018).

[17] Naik, R. K., N. Leung, S. Chakram, Peter Groszkowski, Y. Lu, N. Earnest, D. C. McKay, Jens Koch, and D. I. Schuster. "Random access quantum information processors using

multimode circuit quantum electrodynamics." Nature communications 8, no. 1 (2017): 1904.

[18] Anderson, Philip W., and John M. Rowell. "Probable observation of the Josephson superconducting tunneling effect." Physical Review Letters 10, no. 6 (1963): 230.

[19] Martinis, John M., and Kevin Osborne. "Superconducting qubits and the physics of Josephson junctions." arXiv preprint cond-mat/0402415 (2004).

[20] Astafiev, O. V., L. B. Ioffe, S. Kafanov, Yu A. Pashkin, K. Yu Arutyunov, D. Shahar, O. Cohen, and J. S. Tsai. "Coherent quantum phase slip." Nature 484, no. 7394 (2012): 355.

[21] Viola, Giovanni, and Gianluigi Catelani. "Collective modes in the fluxonium qubit." Physical Review B 92, no. 22 (2015): 224511.

[22] Happer, William. "Optical pumping." Reviews of Modern Physics 44, no. 2 (1972): 169.

[23] Hilser, Florian, and Guido Burkard. "All-optical control of the spin state in the NV center in diamond." Physical Review B 86, no. 12 (2012): 125204.

[24] Jacques, V., P. Neumann, J. Beck, M. Markham, D. Twitchen, J. Meijer, F. Kaiser, G. Balasubramanian, F. Jelezko, and J. Wrachtrup. "Dynamic polarization of single nuclear spins by optical pumping of nitrogen-vacancy color centers in diamond at room temperature." Physical review letters 102, no. 5 (2009): 057403.

[25] Nicholson, T. L., S. L. Campbell, R. B. Hutson, G. E. Marti, B. J. Bloom, R. L. McNally, Wei Zhang et al. "Systematic evaluation of an atomic clock at 2 10 18 total uncertainty." Nature communications 6 (2015): 6896.

[26] Monroe, Chris, D. M. Meekhof, B. E. King, Wayne M. Itano, and David J. Wineland.

"Demonstration of a fundamental quantum logic gate." Physical review letters 75, no. 25 (1995): 4714.

[27] Weisskopf, Victor, and Eugene Wigner. "Berechnung der natrlichen linienbreite auf grund der diracschen lichttheorie." Zeitschrift fr Physik 63, no. 1-2 (1930): 54-73.

[28] Kandala, Abhinav, Antonio Mezzacapo, Kristan Temme, Maika Takita, Markus Brink, Jerry M. Chow, and Jay M. Gambetta. "Hardware-efficient variational quantum eigensolver for small molecules and quantum magnets." Nature 549, no. 7671 (2017): 242.

[29] Rastelli, Gianluca, Ioan M. Pop, and Frank WJ Hekking. "Quantum phase slips in Josephson junction rings." Physical Review B 87, no. 17 (2013): 174513.

[30] Hazard, T. M., A. Gyenis, A. Di Paolo, A. T. Asfaw, S. A. Lyon, A. Blais, and A. A. Houck. "Nanowire Superinductance fluxonium Qubit." arXiv preprint arXiv:1805.00938 (2018).

[31] Lecocq, Florent, Ccile Naud, Ioan M. Pop, Zhi-Hui Peng, Iulian Matei, Thierry Crozes, Thierry Fournier, Wiebke Guichard, and Olivier Buisson. "Novel E-beam lithography technique for in-situ junction fabrication: the controlled undercut." arXiv preprint arXiv:1101.4576 (2011).

[32] Lu, Yao, Srivatsan Chakram, Nelson Leung, Nathan Earnest, Ravi K. Naik, Ziwen Huang, Peter Groszkowski, Eliot Kapit, Jens Koch, and David I. Schuster. "Universal stabilization of a parametrically coupled qubit." Physical review letters 119, no. 15 (2017): 150502.

[33] Wu, X., J. L. Long, H. S. Ku, R. E. Lake, M. Bal, and D. P. Pappas. "Overlap junctions for high coherence superconducting qubits." Applied Physics Letters 111, no. 3 (2017): 032602.

[34] Zeng, L. J., S. Nik, Tine Greibe, Philip Krantz, C. M. Wilson, Per Delsing, and Eva Olsson. "Direct observation of the thickness distribution of ultra thin AlO x barriers in Al/AlO x/Al Josephson junctions." Journal of Physics D: Applied Physics 48, no. 39 (2015): 395308.

[35] Fenner, D. B., D. K. Biegelsen, and R. D. Bringans. "Silicon surface passivation by hydrogen termination: A comparative study of preparation methods." Journal of Applied Physics 66, no. 1 (1989): 419-424.

[36] Vissers, Michael R., Jiansong Gao, David S. Wisbey, Dustin A. Hite, Chang C. Tsuei, Antonio D. Corcoles, Matthias Steffen, and David P. Pappas. "Low loss superconducting titanium nitride coplanar waveguide resonators." Applied Physics Letters 97, no. 23 (2010): 232509.

[37] Grnhaupt, Lukas, Nataliya Maleeva, Sebastian T. Skacel, Martino Calvo, Florence Levy-Bertrand, Alexey V. Ustinov, Hannes Rotzinger, Alessandro Monfardini, Gianluigi Catelani, and Ioan M. Pop. "Quasiparticle dynamics in granular aluminum close to the superconductor to insulator transition." arXiv preprint arXiv:1802.01858 (2018).

[38] Bateman, James, Andr Xuereb, and Tim Freegarde. "Stimulated Raman transitions via multiple atomic levels." Physical Review A 81, no. 4 (2010): 043808.

[39] Mishina, O. S., M. Scherman, P. Lombardi, J. Ortalo, D. Felinto, A. S. Sheremet, A. Bramati, D. V. Kupriyanov, J. Laurat, and E. Giacobino. "Electromagnetically induced transparency in an inhomogeneously broadened transition with multiple excited levels." Physical Review A 83, no. 5 (2011): 053809.

[40] Anisimov, Petr M., Jonathan P. Dowling, and Barry C. Sanders. "Objectively discerning Autler-Townes splitting from electromagnetically induced transparency." Physical review letters 107, no. 16 (2011): 163604.

[41] Fleischhauer, Michael, Atac Imamoglu, and Jonathan P. Marangos. "Electromagnetically induced transparency: Optics in coherent media." Reviews of modern physics 77, no. 2 (2005): 633.

[42] Santori, Charles, David Fattal, Sean M. Spillane, Marco Fiorentino, Raymond G. Beausoleil, Andrew D. Greentree, Paolo Olivero et al. "Coherent population trapping in diamond NV centers at zero magnetic field." Optics Express 14, no. 17 (2006): 7986-7994.

[43] Yale, Christopher G., Bob B. Buckley, David J. Christle, Guido Burkard, F. Joseph Heremans, Lee C. Bassett, and David D. Awschalom. "All-optical control of a solid-state spin using coherent dark states." Proceedings of the National Academy of Sciences 110, no. 19 (2013): 7595-7600.

[44] Weil, Thomas, Bruno Kng, E. Dumur, Alexey K. Feofanov, Iulian Matei, Ccile Naud, Olivier Buisson, Frank WJ Hekking, and Wiebke Guichard. "Kerr coefficients of plasma resonances in josephson junction chains." Physical Review B 92, no. 10 (2015): 104508.

[45] Maleeva, Nataliya, Lukas Gruenhaupt, T. Klein, F. Levy-Bertrand, O. Dupr, M. Calvo, F. Valenti et al. "Circuit quantum electrodynamics of granular Aluminum resonators." arXiv preprint arXiv:1802.01859 (2018).

[46] Muppalla, P. R., O. Gargiulo, S. I. Mirzaei, B. Prasanna Venkatesh, M. L. Juan, L. Grnhaupt, I. M. Pop, and G. Kirchmair. "Bistability in a mesoscopic Josephson junction array resonator." Physical Review B 97, no. 2 (2018): 024518.

[47] Averin, D. V., A. B. Zorin, and K. K. Likharev. "Bloch oscillations in small Josephson junctions." Sov. Phys. JETP 61, no. 2 (1985): 407-413.

[48] Masluk, Nicholas Adam. Reducing the losses of the fluxonium artificial atom. Yale University, 2013.

[49] Zheng, Huaixiu, Matti Silveri, R. T. Brierley, S. M. Girvin, and K. W. Lehnert. "Accelerating dark-matter axion searches with quantum measurement technology." arXiv preprint arXiv:1607.02529 (2016).

[50] Shokair, T. M., J. Root, K. A. Van Bibber, B. Brubaker, Y. V. Gurevich, S. B. Cahn, S. K. Lamoreaux et al. "Future directions in the microwave cavity search for dark matter axions." International Journal of Modern Physics A 29, no. 19 (2014): 1443004.

[51] Manucharyan, Vladimir Eduardovich. "Superinductance." PhD diss., Yale University, 2012.

[52] Koch, Jens, V. Manucharyan, M. H. Devoret, and L. I. Glazman. "Charging effects in the inductively shunted Josephson junction." Physical review letters 103, no. 21 (2009): 217004.

[53] Zhu, Guanyu, and Jens Koch. "Asymptotic expressions for charge-matrix elements of the fluxonium circuit." Physical Review B 87, no. 14 (2013): 144518.

[54] Dempster, Joshua M., Bo Fu, David G. Ferguson, D. I. Schuster, and Jens Koch. "Understanding degenerate ground states of a protected quantum circuit in the presence of disorder." Physical Review B 90, no. 9 (2014): 094518.

[55] Brooks, Peter, Alexei Kitaev, and John Preskill. "Protected gates for superconducting qubits." Physical Review A 87, no. 5 (2013): 052306.

[56] Ulrich, Jascha, and Fabian Hassler. "Dual approach to circuit quantization using loop charges." Physical Review B 94, no. 9 (2016): 094505.

[57] Pekker, David, Chang-Yu Hou, Vladimir E. Manucharyan, and Eugene Demler. "Proposal for coherent coupling of Majorana zero modes and superconducting Qubits using the 4 ? Josephson effect." Physical review letters 111, no. 10 (2013): 107007.

[58] "fluxonium Artificial Atoms and Quantum Measurement Techniques." minute 20 YouTube. April 18, 2016. Accessed June 28, 2018.

[59] Cottet, Nathanal, and Benjamin Huard. "Maxwell's demon in superconducting circuits." arXiv preprint arXiv:1805.01224 (2018).

[60] Cottet, Nathanal, Sebastien Jezouin, Landry Bretheau, Philippe Campagne-Ibarcq, Quentin Ficheux, Janet Anders, Alexia Auffves, Rmi Azouit, Pierre Rouchon, and Benjamin Huard. "Observing a quantum Maxwell demon at work." Proceedings of the National Academy of Sciences 114, no. 29 (2017): 7561-7564.

[61] Wu, X., J. L. Long, H. S. Ku, R. E. Lake, M. Bal, and D. P. Pappas. "Overlap junctions for high coherence superconducting qubits." Applied Physics Letters 111, no. 3 (2017): 032602.

[62] Abigail Shearrow "0-Pi" Schuster lab drive S/Abigail/0-Pi/Circuit Calculation / 0-pi.pdf

[63] Bosman, Sal J., Mario F. Gely, Vibhor Singh, Alessandro Bruno, Daniel Bothner, and Gary A. Steele. "Multi-mode ultra-strong coupling in circuit quantum electrodynamics." npj Quantum Information 3, no. 1 (2017): 46.

[64] Bouchiat, Vincent, D. Vion, Ph Joyez, D. Esteve, and M. H. Devoret. "Quantum coherence with a single Cooper pair." Physica Scripta 1998, no. T76 (1998): 165.

[65] Vladimir Manucharyan. "TBA" Invited talk Bulletin of the American Physical Society (2018).

[66] Einstein, Albert, Boris Podolsky, and Nathan Rosen. "Can quantum-mechanical description of physical reality be considered complete?." Physical review 47, no. 10 (1935): 777.

[67] Josephson, Brian David. "Possible new effects in superconductive tunnelling." Physics letters 1, no. 7 (1962): 251-253.

[68] Devoret, M. H., Steven Girvin, and Robert Schoelkopf. "Circuit?QED: How strong can the coupling between a Josephson junction atom and a transmission line resonator be?." Annalen der Physik 16, no. 10?11 (2007): 767-779.

[69] Nation, P. D., M. P. Blencowe, A. J. Rimberg, and E. Buks. "Analogue Hawking radiation in a dc-SQUID array transmission line." Physical review letters 103, no. 8 (2009): 087004.

[70] Devoret, M. H., and Hermann Grabert. "Introduction to single charge tunneling." In Single Charge Tunneling, pp. 1-19. Springer, Boston, MA, 1992.